BEILSTEIN JOURNAL OF NANOTECHNOLOGY

Energy conversion applications of atomic layer deposition

Edited by Julien Bachmann

Imprint

Beilstein Journal of Nanotechnology
www.bjnano.org
ISSN 2190-4286
Email: journals-support@beilstein-institut.de

The *Beilstein Journal of Nanotechnology* is published by the Beilstein-Institut zur Förderung der Chemischen Wissenschaften.

Beilstein-Institut zur Förderung der
Chemischen Wissenschaften
Trakehner Straße 7–9
60487 Frankfurt am Main
Germany
www.beilstein-institut.de

Beilstein Journal
of Nanotechnology

Atomic layer deposition, a unique method for the preparation of energy conversion devices

Julien Bachmann

Editorial

Address:
Institute of Inorganic Chemistry, Friedrich-Alexander University of Erlangen-Nürnberg, Egerlandstrasse 1, 91058 Erlangen, Germany

Email:
Julien Bachmann - julien.bachmann@fau.de

Keywords:
atomic layer deposition; batteries; energy conversion; electrochemistry; electrolysis; fuel cells; photovoltaics; solar cells; thin films

Beilstein J. Nanotechnol. **2014,** *5,* 245–248.
doi:10.3762/bjnano.5.26

Received: 28 October 2013
Accepted: 28 October 2013
Published: 05 March 2014

This article is part of the Thematic Series "Energy conversion applications of atomic layer deposition".

Editor-in-Chief: T. Schimmel

Most of the technical development of the 19th and 20th centuries relied on thermal engines to generate mechanical or electrical work from the combustion of fossil fuels [1]. This strategy of energy production is not renewable, in that finite resources are consumed and greenhouse gases are emitted, and it is also fundamentally inefficient as defined by Carnot. In a more modern strategy which circumvents those disadvantages of thermal machines, energy is converted directly from solar (or some other renewable source) to its electrical or chemical form [2]. Here, fuels still play a fundamental role as energy carriers for the storage and the regulation of the electrical power grid, but they are converted to other energy forms by electrochemical methods rather than thermal engines.

The interconversion of energy between light and electrical forms (in solar cells and light-emitting diodes), between light and chemical forms (photosynthesis and chemiluminescence), and between chemical and electrical forms (batteries, electrolyzers, fuel cells, respiration) always relies on the transport of charge carriers towards an interface and away from it, combined with the transfer of electrons at the interface. This electron transfer, the most fundamental energy-converting single event, occurs at the interface between two phases, which can have various identities depending on the type of device. In most solar cells these two phases are two solid semiconductors, in batteries and fuel cells they are usually a solid and an electrolytic liquid, and in the 'light reactions' of photosynthesis the two phases consist of two liquids separated by a lipidic membrane. The nature of the charge carriers that transport electrons between the bulk and the interface varies accordingly: electrons and holes in semiconductors, molecules and ions in electrolytes. Figure 1 summarizes the particular types of charge and energy carriers in a solar cell (left), an electrode of a lithium

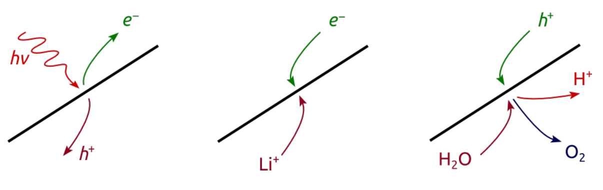

Figure 1: Nature of the charge carriers combining or separating at an interface in a solar cell (left), a lithium ion battery (center), and the water oxidation electrode of an electrolyzer (or the oxygen-evolving complex in photosynthesis, right).

ion battery (center), and the water oxidation electrode of an electrolyzer (right).

Despite the variety of physical states and chemical identities found in such energy conversion devices, they all share a fundamental principle: an increase of the geometric area of their interfaces should result in a commensurate increase in their throughput, until the concomitant increase in the diffusion distances of the charge carriers between the bulk and the interface causes transport to become limiting. For this reason, nanostructured interfaces with elongated folds or tubes can result in optimized devices (Figure 2).

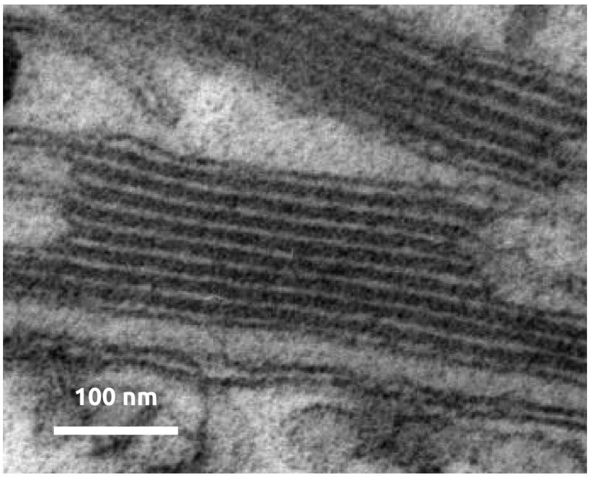

Figure 2: An example of nanostructured interfaces in an energy conversion device: thylakoids for photosynthesis (micrograph adapted and reproduced with author permission; (c) Andreas Anderluh and Bela Hausmann).

In this context, any method capable of depositing thin functional layers onto structured substrates, and especially into nanoporous frameworks, is conferred with a direct relevance towards energy conversion applications. The conformal coating of non-planar samples is a property that uniquely defines atomic layer deposition (ALD) [3-7], which is why ALD is inherently suited to the preparation of energy conversion devices. ALD achieves a thin film growth by using well-defined surface chemistry. Two (or more) complementary, quantitative surface reactions performed subsequently and repeated in an alternating manner result in the deposition of a solid in a layer-by-layer fashion [8-10]. The surface chemistry is ‘self-limiting’: each reaction deposits an amount of material defined by the availability of surface reactive groups, not by the (local) partial pressure of gaseous precursors. This growth mode circumvents mass transport as the rate-limiting factor of the increase of the film thickness, thereby allowing for a homogeneous growth even if the gas phase is inhomogeneous – a situation notably found in highly porous systems.

Readers of this Thematic Series will obtain a glimpse of the broad applicability of the method in different types of energy conversion devices (summarized in Table 1). The plethora of functions which can be performed by ALD materials may be rationalized if a few common themes are recognized, which run like a common thread through this Thematic Series:

- ALD for a direct device function, such as light absorption in solar cells, ion conduction and electrocatalysis in fuel cells, or lithium uptake in batteries;
- ALD for separation and protection, in particular to prevent erosion or corrosion in electrochemical devices;

Table 1: A non-exhaustive list of exemplary ALD applications in energy conversion devices illustrated in this Thematic Series and in previous literature. Reviews have been published recently on the applications of ALD in photovoltaics [11], lithium ion batteries [12], and solid oxide fuel cells [13].

Device type	Function of the ALD film	Literature references	References in this Thematic Series
Batteries	Li ion electrode materials	[14-16]	[17]
Batteries	Protective layer	[18,19]	
Batteries, fuel cells	Ion conduction	[20-22]	
Fuel cells, electrolysis, photoelectrolysis	Electrocatalysis	[23-26]	[27,28]
Photoelectrolysis, photovoltaics	Light absorber	[29-31]	
Photoelectrolysis, photovoltaics	Transparent conducting oxide	[32,33]	[34,35]
Photovoltaics	Electron conductor	[36-39]	[40,41]
Photovoltaics	Surface passivation	[42-44]	[45,46]
Photovoltaics	Tunnel barriers	[47,48]	

- ALD for interface engineering, for example defect passivation in solar cells or prevention of charge recombination by tunnel barriers, and for influencing the electronic structure of an underlying semiconductor.

This Thematic Series will certainly provide the reader with novel ideas for exploiting ALD in the energy realm, and spur further original work in this rapidly developing research area. After its industrial application in electroluminescent displays, semiconductor logics (MOSFET), magnetic memory (TMR sensors) and semiconductor memory (DRAM), ALD has the potential to also become a critical tool in the area of energy conversion.

Julien Bachmann

Erlangen, November 2013

References

1. Armaroli, N.; Balzani, V. *Angew. Chem., Int. Ed.* **2006,** *46,* 52–66. doi:10.1002/anie.200602373
2. Nocera, D. G. *ChemSusChem* **2009,** *2,* 387–390. doi:10.1002/cssc.200900040
3. Elam, J. W.; Routkevitch, D.; Mardilovich, P. P.; George, S. M. *Chem. Mater.* **2003,** *15,* 3507–3517. doi:10.1021/cm0303080
4. Bachmann, J.; Jing, J.; Knez, M.; Barth, S.; Shen, H.; Mathur, S.; Gösele, U.; Nielsch, K. *J. Am. Chem. Soc.* **2007,** *129,* 9554–9555. doi:10.1021/ja072465w
5. Knez, M.; Nielsch, K.; Niinistö, L. *Adv. Mater.* **2007,** *19,* 3425–3438. doi:10.1002/adma.200700079
6. Detavernier, C.; Dendooven, J.; Sree, S. P.; Ludwig, K. F.; Martens, J. A. *Chem. Soc. Rev.* **2011,** *40,* 5242–5253. doi:10.1039/c1cs15091j
7. Peng, Q.; Lewis, J. S.; Hoertz, P. G.; Glass, J. T.; Parsons, G. N. *J. Vac. Sci. Technol., A* **2012,** *30,* 010803. doi:10.1116/1.3672027
8. Puurunen, R. L. *J. Appl. Phys.* **2005,** *97,* 121301. doi:10.1063/1.1940727
9. Leskelä, M.; Ritala, M. *Angew. Chem., Int. Ed.* **2003,** *42,* 5548–5554. doi:10.1002/anie.200301652
10. George, S. M. *Chem. Rev.* **2010,** *110,* 111–131. doi:10.1021/cr900056b
11. van Delft, J. A.; Garcia-Alonso, D.; Kessels, W. M. M. *Semicond. Sci. Technol.* **2012,** *27,* 074002. doi:10.1088/0268-1242/27/7/074002
12. Meng, X. B.; Yang, X.-Q.; Sun, X. *Adv. Mater.* **2012,** *24,* 3589–3615. doi:10.1002/adma.201200397
13. Cassir, M.; Ringuedé, A.; Niinistö, L. *J. Mater. Chem.* **2010,** *20,* 8987–8993. doi:10.1039/c0jm00590h
14. Wang, W.; Tian, M.; Abdulagatov, A.; George, S. M.; Lee, Y.-C.; Yang, R. *Nano Lett.* **2012,** *12,* 655–660. doi:10.1021/nl203434g
15. Donders, M. E.; Knoops, H. C. M.; Kessels, W. M. M.; Notten, P. H. L. *J. Power Sources* **2012,** *203,* 72–77. doi:10.1016/j.jpowsour.2011.12.020
16. Chen, X.; Pomerantseva, E.; Gregorczyk, K.; Ghodssi, R.; Rubloff, G. *RSC Adv.* **2013,** *3,* 4294–4302. doi:10.1039/c3ra23031g
17. Grünzel, T.; Lee, Y. J.; Kuepper, K.; Bachmann, J. *Beilstein J. Nanotechnol.* **2013,** *4,* 655–664. doi:10.3762/bjnano.4.73
18. Jung, Y. S.; Cavanagh, A. S.; Riley, L. A.; Kang, S.-H.; Dillon, A. C.; Groner, M. D.; George, S. M.; Lee, S.-H. *Adv. Mater.* **2010,** *22,* 2172–2176. doi:10.1002/adma.200903951
19. Li, X.; Meng, X.; Liu, J.; Geng, D.; Zhang, Y.; Banis, M. N.; Li, Y.; Yang, J.; Li, R.; Sun, X.; Cai, M.; Verbrugge, M. W. *Adv. Funct. Mater.* **2012,** *22,* 1647–1654. doi:10.1002/adfm.201101068
20. Ballée, E.; Ringuedé, A.; Cassir, M.; Putkonen, M.; Niinistö, L. *Chem. Mater.* **2009,** *21,* 4614–4619. doi:10.1021/cm9016968
21. Shim, J. H.; Chao, C.-C.; Huang, H.; Prinz, F. B. *Chem. Mater.* **2007,** *19,* 3850–3854. doi:10.1021/cm070913t
22. Hämäläinen, J.; Holopainen, J.; Munnik, F.; Hatanpää, T.; Heikkilä, M.; Ritala, M.; Leskelä, M. *J. Electrochem. Soc.* **2012,** *159,* A259–A263. doi:10.1149/2.052203jes
23. Jiang, X.; Huang, H.; Prinz, F. B.; Bent, S. F. *Chem. Mater.* **2008,** *20,* 3897–3905. doi:10.1021/cm7033189
24. Rikkinen, E.; Santasalo-Aarnio, A.; Airaksinen, S.; Borghei, M.; Viitanen, V.; Sainio, J.; Kauppinen, E. I.; Kallio, T.; Krause, A. O. I. *J. Phys. Chem. C* **2011,** *115,* 23067–23073. doi:10.1021/jp2083659
25. Gemmer, J.; Hinrichsen, Y.; Abel, A.; Bachmann, J. *J. Catal.* **2012,** *290,* 220–224. doi:10.1016/j.jcat.2012.03.022
26. Riha, S. C.; Klahr, B. M.; Tyo, E. C.; Seifert, S.; Vajda, S.; Pellin, M. J.; Hamann, T. W.; Martinson, A. B. F. *ACS Nano* **2013,** *7,* 2396–2405. doi:10.1021/nn305639z
27. Assaud, L.; Monyoncho, E.; Pitzschel, K.; Allagui, A.; Petit, M.; Hanbücken, M.; Baranova, E. A.; Santinacci, L. *Beilstein J. Nanotechnol.* **2014,** *5,* 162–172. doi:10.3762/bjnano.5.16
28. Tallarida, M.; Das, C.; Schmeisser, D. *Beilstein J. Nanotechnol.* **2014,** *5,* 77–82. doi:10.3762/bjnano.5.7
29. Sarkar, S. K.; Kim, J. Y.; Goldstein, D. N.; Neale, N. R.; Zhu, K.; Elliot, C. M.; Frank, A. J.; George, S. M. *J. Phys. Chem. C* **2010,** *114,* 8032–8039. doi:10.1021/jp9086943
30. Wedemeyer, H.; Michels, J.; Chmielowski, R.; Bourdais, S.; Muto, T.; Sugiura, M.; Dennler, G.; Bachmann, J. *Energy Environ. Sci.* **2013,** *6,* 67–71. doi:10.1039/c2ee23205g
31. Klahr, B. M.; Martinson, A. B. F.; Hamann, T. W. *Langmuir* **2011,** *27,* 461–468. doi:10.1021/la103541n
32. Godlewski, M.; Guziewicz, E.; Łuka, G.; Krajewski, T.; Łukasiewicz, M.; Wachnicki, Ł.; Wachnicka, A.; Kopalko, K.; Sarem, A.; Dalati, B. *Thin Solid Films* **2009,** *518,* 1145–1148. doi:10.1016/j.tsf.2009.04.066
33. Lee, D.-J.; Kim, H.-M.; Kwon, J.-Y.; Choi, H.; Kim, S.-H.; Kim, K.-B. *Adv. Funct. Mater.* **2011,** *21,* 448–455. doi:10.1002/adfm.201001342
34. Chaaya, A. A.; Viter, R.; Bechelany, M.; Alute, Z.; Erts, D.; Zalesskaya, A.; Kovalevskis, K.; Rouessac, V.; Smyntyna, V.; Miele, P. *Beilstein J. Nanotechnol.* **2013,** *4,* 690–698. doi:10.3762/bjnano.4.78
35. Pietruszka, R.; Witkowski, B. S.; Luka, G.; Wachnicki, L.; Gieraltowska, S.; Kopalko, K.; Zielony, E.; Bieganski, P.; Placzek-Popko, E.; Godlewski, M. *Beilstein J. Nanotechnol.* **2014,** *5,* 173–179. doi:10.3762/bjnano.5.17
36. Martinson, A. B. F.; Góes, M. S.; Fabregat-Santiago, F.; Bisquert, J.; Pellin, M. J.; Hupp, J. T. *J. Phys. Chem. A* **2009,** *113,* 4015–4021. doi:10.1021/jp810406q
37. Schmidt, H.; Flügge, H.; Winkler, T.; Bülow, T.; Riedl, T.; Kowalsky, W. *Appl. Phys. Lett.* **2009,** *94,* 243302. doi:10.1063/1.3154556
38. Yousfi, E. B.; Weinberger, B.; Donsanti, F.; Cowache, P.; Lincot, D. *Thin Solid Films* **2001,** *387,* 29–32. doi:10.1016/S0040-6090(00)01838-1

39. Hultqvist, A.; Platzer-Björkman, C.; Pettersson, J.; Törndahl, T.; Edoff, M. *Thin Solid Films* **2009,** *517,* 2305–2308. doi:10.1016/j.tsf.2008.10.109
40. Bugot, C.; Schneider, N.; Lincot, D.; Donsanti, F. *Beilstein J. Nanotechnol.* **2013,** *4,* 750–757. doi:10.3762/bjnano.4.85
41. Yazdani, N.; Chawla, V.; Edwards, E.; Wood, V.; Park, H. G.; Utke, I. *Beilstein J. Nanotechnol.* **2014,** *5,* 234–244. doi:10.3762/bjnano.5.25
42. Hoex, B.; Heil, S. B. S.; Langereis, E.; van de Sanden, M. C. M.; Kessels, W. M. M. *Appl. Phys. Lett.* **2006,** *89,* 042112. doi:10.1063/1.2240736
43. Tétreault, N.; Arsenault, É.; Heiniger, L.-P.; Soheilnia, N.; Brillet, J.; Moehl, T.; Zakeeruddin, S.; Ozin, G. A.; Grätzel, M. *Nano Lett.* **2011,** *11,* 4579–4584. doi:10.1021/nl201792r
44. Natu, G.; Huang, Z.; Ji, Z.; Wu, Y. *Langmuir* **2012,** *28,* 950–956. doi:10.1021/la203534s
45. Haeberle, J.; Henkel, K.; Gargouri, H.; Naumann, F.; Gruska, B.; Arens, M.; Tallarida, M.; Schmeißer, D. *Beilstein J. Nanotechnol.* **2013,** *4,* 732–742. doi:10.3762/bjnano.4.83
46. López, G.; Ortega, P. R.; Voz, C.; Martín, I.; Colina, M.; Morales, A. B.; Orpella, A.; Alcubilla, R. *Beilstein J. Nanotechnol.* **2013,** *4,* 726–731. doi:10.3762/bjnano.4.82
47. Chandiran, A. K.; Tétreault, N.; Humphry-Baker, R.; Kessler, F.; Baranoff, E.; Yi, C.; Nazeeruddin, M. K.; Grätzel, M. *Nano Lett.* **2012,** *12,* 3941–3947. doi:10.1021/nl301023r
48. Law, M.; Greene, L. E.; Radenovic, A.; Kuykendall, T.; Liphardt, J.; Yang, P. *J. Phys. Chem. B* **2006,** *110,* 22652–22663. doi:10.1021/jp0648644

License and Terms

The definitive version of this article is the electronic one which can be found at:
doi:10.3762/bjnano.5.26

Beilstein Journal
of Nanotechnology

Preparation of electrochemically active silicon nanotubes in highly ordered arrays

Tobias Grünzel[1], Young Joo Lee[1], Karsten Kuepper[2]
and Julien Bachmann[*1,3]

Full Research Paper

Address:
[1]Physics Department and Chemistry Department, University of Hamburg, Sedanstrasse 19, 20146 Hamburg, Germany, [2]Physics Department, University of Osnabrück, Barbarastrasse 7, 49076 Osnabrück, Germany and [3]Department of Chemistry and Pharmacy, Friedrich Alexander University Erlangen-Nürnberg, Egerlandstrasse 1, 91058 Erlangen, Germany

Email:
Julien Bachmann* - julien.bachmann@fau.de

* Corresponding author

Keywords:
atomic layer deposition; electrochemistry; lithium ion battery electrode; silica thermal reduction; silicon nanotubes

Beilstein J. Nanotechnol. **2013,** *4,* 655–664.
doi:10.3762/bjnano.4.73

Received: 26 July 2013
Accepted: 19 September 2013
Published: 16 October 2013

This article is part of the Thematic Series "Energy conversion applications of atomic layer deposition".

Associate Editor: N. Motta

Abstract

Silicon as the negative electrode material of lithium ion batteries has a very large capacity, the exploitation of which is impeded by the volume changes taking place upon electrochemical cycling. A Si electrode displaying a controlled porosity could circumvent the difficulty. In this perspective, we present a preparative method that yields ordered arrays of electrochemically competent silicon nanotubes. The method is based on the atomic layer deposition of silicon dioxide onto the pore walls of an anodic alumina template, followed by a thermal reduction with lithium vapor. This thermal reduction is quantitative, homogeneous over macroscopic samples, and it yields amorphous silicon and lithium oxide, at the exclusion of any lithium silicides. The reaction is characterized by spectroscopic ellipsometry for thin silica films, and by nuclear magnetic resonance and X-ray photoelectron spectroscopy for nanoporous samples. After removal of the lithium oxide byproduct, the silicon nanotubes can be contacted electrically. In a lithium ion electrolyte, they then display the electrochemical waves also observed for other bulk or nanostructured silicon systems. The method established here paves the way for systematic investigations of how the electrochemical properties (capacity, charge/discharge rates, cyclability) of nanoporous silicon negative lithium ion battery electrode materials depend on the geometry.

Introduction

A significant research and development effort has been dedicated to the positive electrode materials of lithium ion batteries [1]. In contrast, the negative electrode of all commercial lithium ion batteries still consists of graphite, which can intercalate lithium up to a theoretical stoichiometry LiC_6 [2]. Silicon, however, can react with lithium to create several phases with stoichiometries as high as $Li_{4.4}Si$ [3]. This corresponds to a theoretical lithium storage capacity of 4200 mAh g^{-1}, more than 10 times as high as in the case of LiC_6. Even the number 3000 mAh g^{-1}, which is also often mentioned in the literature, is still eight times as high as for graphite [4]. Unfortunately, the significant volume changes that occur upon loading of Si with Li, and which are associated with the concomitant phase transitions, severely constraint the practical exploitation of this very large capacity [5]. In bulk silicon, one does not limit oneself to charging and discharging a small fraction of the theoretically available lithium, the mechanical tensions generated by the full electrochemical cycling will rupture the solid and large fractions of the material will lose the electrical contact.

In principle, this difficulty could be circumvented by nanostructuring. A porous structure in which parallel cylindrical channels run 'vertically' from the electrolyte to the vicinity of the current collector should allow for a 'lateral' expansion of the electrode material upon charging, whereas direct 'vertical' transport paths are maintained for the charge carriers in the solid electrode (for the electrons) and in the electrolyte (for the Li^+ ions). The transport of Li^+ ions inside the solid remains 'horizontal', so that the lateral characteristic length of the porous structure should be small. Indeed, a proof of principle has been provided based on nanowires and nanotubes obtained either by vapor-liquid solid methods or from bulk silicon [6-8], and based on porous silicon [7,9]. However, no study is available to date in which the geometric parameters of this system were varied systematically in order to pinpoint the critical length scales associated with mass transport, charge transport, and mechanical relaxation.

We propose an experimental platform specifically designed to provide the experimental capability of tuning individually every single geometric parameter in such a porous silicon structure created in an inert matrix (Figure 1): the pore length L, the pore diameter D, the silicon layer thickness d, and the interpore distance P. The matrix (white) will be prepared by the two-step anodization of aluminum, a procedure which enables the experimentalist to generate templates of ordered cylindrical pores with a tunable period 50 nm ≤ P ≤ 450 nm and a length 0.1 µm ≤ L ≤ 100 µm [10,11]. Subsequently, the functional material will be deposited into the pores conformally by atomic layer deposition (ALD). This method based on well-defined, self-limiting surface reactions carried out in a cyclic manner enables one to create films of accurately tunable thickness d on the surfaces of such porous substrates [12-15], Because silicon is one of the very few simple inorganic solids for which no practical ALD reaction scheme is available [16], we will deposit SiO_2 instead [17,18], and then reduce it to elemental silicon. This paper reports on the reduction reaction that we developed based on lithium vapor, which exhibits the following crucial properties: (1) quantitative and homogeneous conversion of the sample, (2) conservation of the nanoscale morphology, (3) facile removal of the byproduct, (4) possibility to be carried out at reasonably low temperature and within a short time.

Results and Discussion

Overview of the preparation

The preparative path devised for making ordered arrays of electrically contacted silicon nanotubes is presented in Figure 2. In the first step (a), a double anodization (electrochemical oxidation of aluminum in a protic solution) is carried out under 40 V in oxalic acid at 7 °C according to the standard procedure [11]: after the first anodization, the disordered porous aluminum oxide layer obtained is removed in chromic acid, then the

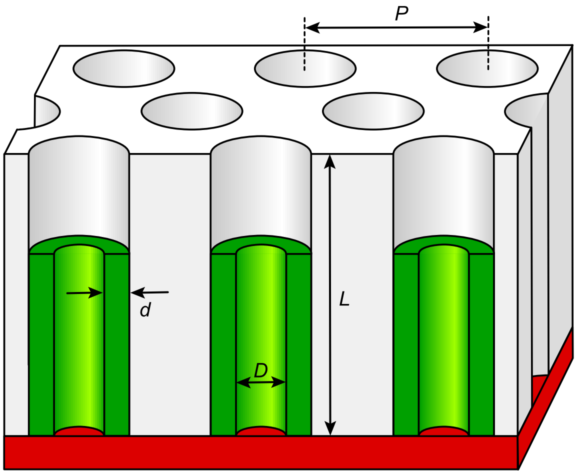

Figure 1: Schematic view of the proposed system, including all tunable geometric parameters. An inorganic matrix (white) defines cylindrical pores of length *L* and in a hexagonal order of period *P*. The silicon tubes (green) have a wall thickness *d* and an inner diameter *D*. The electrical contact is represented in red color.

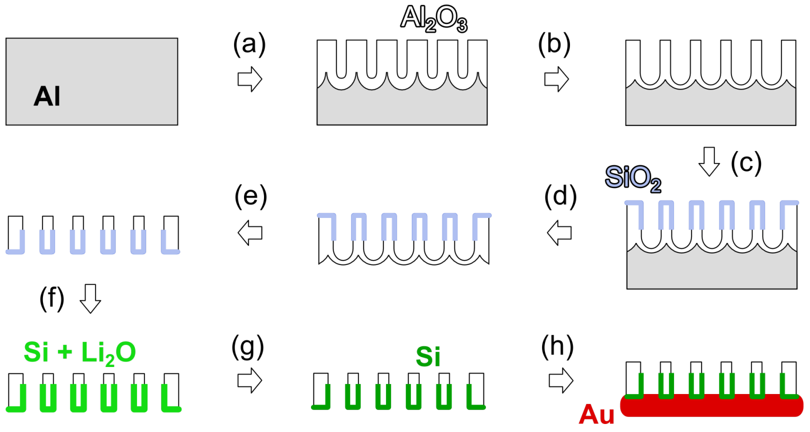

Figure 2: Preparative scheme: (a) –e^-, $H_2C_2O_4/H_2O$, 7 °C (two-step anodization); (b) H_3PO_4/H_2O, 45 °C (pore widening); (c) $H_2N(CH_2)_3Si(OEt)_3$, H_2O, O_3/O_2, 150 °C (ALD); (d) $CuCl_2/HCl/H_2O$, 20 °C; (e) H_3PO_4/H_2O, 45 °C; (f) Li, 670 °C; (g) HCl/H_2O, 20 °C; (h) Au sputter, 20 °C. Note that despite the impression which may emanate from this cross-section representation, the aluminum oxide framework remains reticulated and continuous throughout (see Figure 1).

ordered porous layer is obtained by a second anodization in the same conditions. The length of the pores is defined by the duration of this second anodization. Subsequently (b), the diameter of the pores is increased from its initial value of 40 nm to approximately 60 nm by an isotropic wet chemical etching in warm phosphoric acid. This step maximizes the space available for the electrochemically active material inside the inert matrix. The inner pore walls are coated by ALD (c) by using 3-aminopropyltriethoxysilane, water, and ozone at 150 °C [17,18]. The underlying metallic aluminum substrate is removed oxidatively (d), and the the so-called barrier layer of oxide closing the pore extremities is opened in warm phosphoric acid (e), which leaves a free-standing nanoporous oxide membrane. Its mechanical stability is only sufficient for practical purposes if its thickness is beyond 100 µm. Because of the very large aspect ratio of the pores, the ALD SiO_2 coating does not reach their lower extremity: in our experimental conditions, the continuous, conformal SiO_2 coating only reaches a depth on the order of 10 µm. Note that the maximal depth of the deposit could be increased by larger pore diameters and/or optimized experimental conditions [19,20]. The uncoated depth of the aluminium oxide matrix remains chemically and electrochemically inert, and thus functions as the membrane separator that is always placed between both electrodes of batteries. Thus here, the separator and negative electrode are combined into a single unit.

The first five preparative steps (a–e) described above follow literature procedures, whereas the subsequent reduction and the byproduct removal (f,g) are new. In the final step, which again is a standard one, an electrical contact of metallic gold is created on the other side of the membrane by magnetron sputtering (h).

Investigation of the SiO_2 reduction on flat samples

A native SiO_2 oxide layer of 200 nm thickness on a crystalline silicon substrate is used as a simple, well-defined model for the initial reactivity tests. We first investigate the reduction with Mg, which has been published [21], and then compare the results with those obtained with Li as the reductant. After having been enclosed in a sealed steel tube in the vicinity of metallic magnesium powder under argon and heated to 700 °C for 7 hours, the wafer piece used as the sample displays a coloration gradient indicative of an incomplete, inhomogeneous reaction (Figure 3b). The result is not improved significantly by longer reaction times or more elevated temperatures. It is consistent with the initial report of this reduction with Mg [21], the authors of which noted that the diatomeous silica used as the substrate turned to a variety of colors from blue (attributed to magnesium silicides) to black (elemental silicon) and brown (incomplete reduction). These qualitative observations can be complemented by quantitative data recorded by spectroscopic ellipsometry. This method analyzes light reflected at the various interfaces present in a thin film sample and enables the experimentalist to determine the layer thicknesses, based on a structural model of the system and the optical properties of the materials involved. In the Si/SiO_2 sample exposed to Mg vapors, the experimental ellipsometry spectra recorded over the visible wavelength range (Figure 3a) evidence a systematic variation from the part of the sample immediately adjacent to the Mg boat (black and blue curves) to its opposite end (green to pink). This variation can be interpreted based on a model in which an unreacted SiO_2 film is situated underneath a mixed Si/MgO layer (Figure 3c). If the spectra are fitted to deliver the thicknesses of these two layers (without any constraint on their sum),

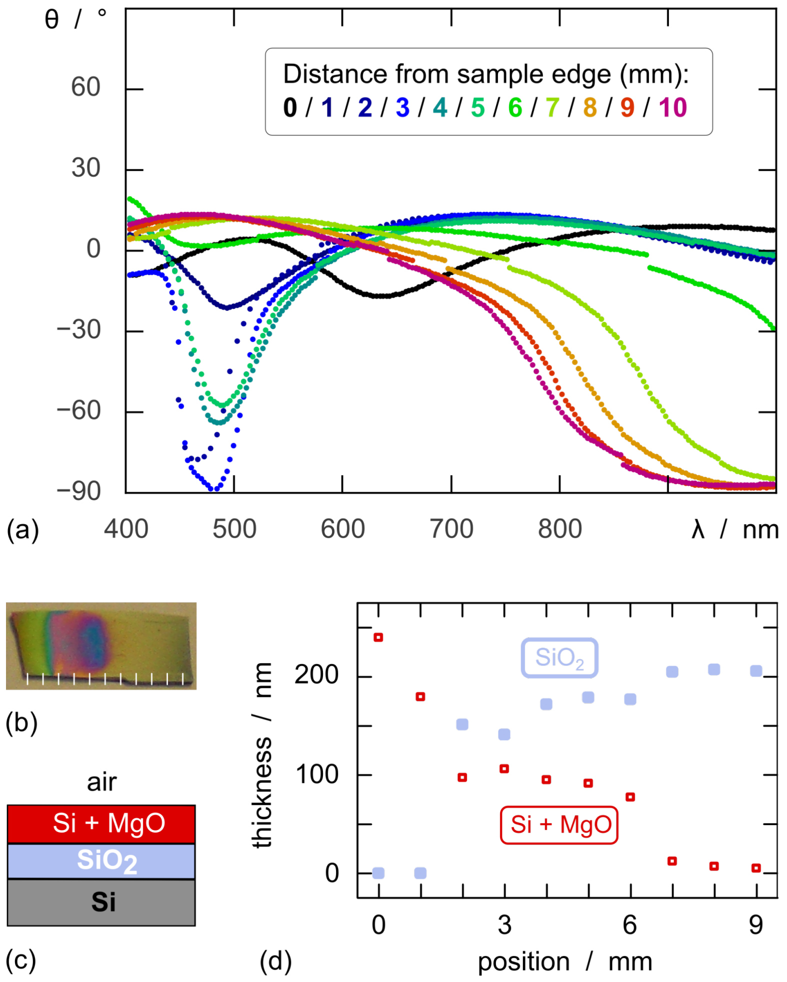

Figure 3: Reaction of a 200-nm thick SiO_2 layer on a silicon wafer with Mg element at 700 °C: (a) spectroscopic ellipsometry orientation data recorded at various positions of the sample; (b) photograph showing the inhomogeneous reaction extent and the position of the ellipsometric measurements; (c) layer stack used to model the ellipsometry data: the mixed layer is treated as a 1:1 mixture with the Lorentz–Lorentz model; (d) results of the fit: thicknesses of the unreacted SiO_2 and converted Si + MgO depending on the distance from the sample edge. The experimental data are presented together with the fit curve at each position of the sample in the Supporting Information File 1 (Figure S1).

a clear picture emerges. The reaction extent transitions smoothly from 100% at position 0 to essentially 0% at a distance of 1 cm (Figure 3d and Figure S1 of Supporting Information File 1).

Thus, the reduction by magnesium vapor cannot be exploited on a preparative scale. Among the other metals that can be considered as alternatives to Mg for the reduction of SiO_2, lithium stands out. Indeed, it is also a strong reductant and provides a negative reaction driving force. Furthermore, lithium also possesses a significant vapor pressure in the range of temperatures considered (Table 1). Its low melting point of 181 °C should be an additional advantage, since it will likely provide faster vaporization kinetics.

Table 1: Properties of the metals M = Mg and M = Li of relevance to the thermal reduction of SiO_2: standard Gibbs free energies of the reactions and metal vapor pressures at two different temperatures [22].

Reaction	$\Delta_rG°$(670 °C) [kJ/mol e^-]	$\Delta_rG°$(700 °C) [kJ/mol e^-]	$p°$(M, 670 °C) [Pa]	$p°$(M, 700 °C) [Pa]
SiO_2 + 2 Mg ǀǀ Si + 2 MgO	–65	–65	570	1000
SiO_2 + 4 Li ǀǀ Si + 2 Li_2O	–56	–56	36	65

In fact, we observe that when the reaction of a SiO_2 film is carried out at 670 °C with lithium instead of magnesium, the reduction is complete, as found by spectroscopic ellipsometry (Figure 4): over the whole sample, the SiO_2 layer is replaced by what can be modeled as a Si + Li_2O mixture in volume ratio 2:3. Furthermore, the ellipsometry spectrum changes again upon treatment with a 1 M HCl solution, in a way consistent with a clean conversion to a porous Si layer (modeled as a 5:1 Si/air mixture).

Application of the thermal SiO_2 reduction to electrochemically active silicon nanotube arrays

When a colorless porous sample, obtained as described above (step (e) of Figure 2), is first dried at 400 °C and then submitted to the same reaction conditions including the subsequent HCl treatment (f,g), its appearance turns to a lustrous black (Figure 5a). The conversion can be monitored by magic angle spinning nuclear magnetic resonance (MAS NMR) spec-

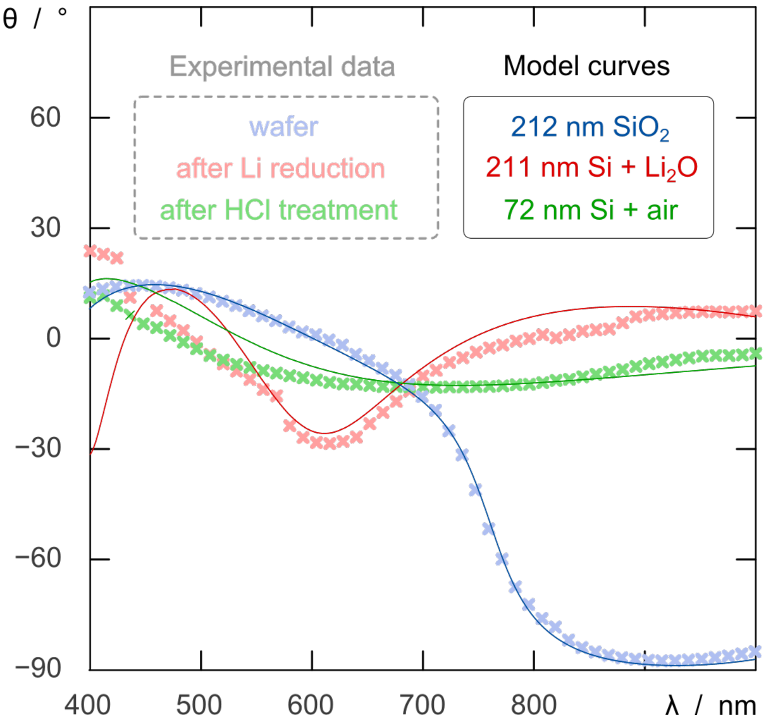

Figure 4: Spectroscopic ellipsometry of flat samples at various stages of preparation: initial substrate with SiO_2 film (blue), after reaction with Li (red), and after acidic treatment and byproduct removal (green). The experimental data are shown as thick, light crosses, whereas the model curves calculated from the corresponding models are drawn as thin, dark lines.

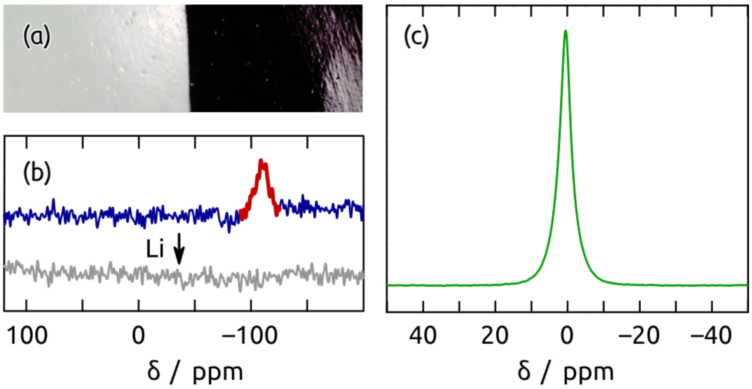

Figure 5: (a) Photograph of two nanoporous samples before and after the reduction by Li vapor with the subsequent acidic treatment (left and right, respectively). (b) ^{29}Si MAS NMR spectra before and after reduction. (c) ^{7}Li MAS NMR spectrum after reduction.

troscopy. In the ^{29}Si MAS NMR spectrum of an ALD sample (step (d) of Figure 2), a resonance is observed at −108.4 ppm (Figure 5b), which can be assigned to 'Q' functional groups ($Si(OR)_4$, R = Si or C) of siloxane compounds [23]. This is consistent with the identity of the material deposited by the ALD process into the porous samples as SiO_2. After reduction with Li metal, the ^{29}Si NMR signal at −108.4 ppm disappears. This indicates a quantitative conversion of SiO_2. However, no signal attributable to a crystalline Si phase can be seen. One possible explanation for the absence of ^{29}Si NMR signal is the highly amorphous character of Si formed by the reduction reaction. Indeed, extremely broad ^{29}Si NMR signals, which are very sensitive to the sample handling conditions, have been reported for Si anode materials [24]. Due to the low natural abundance of ^{29}Si and small quantities of the samples available from ALD, the detection of these broad signals can be challenging. Further investigations with ^{29}Si-enriched samples are conceivable to examine the reduction product and characterize possible structural changes during electrochemical cycling. In ^{7}Li MAS NMR, the reduced material shows a single resonance at +0.5 ppm (Figure 5c), a value characteristic of diamagnetic lithium salts. No signals that could be assigned to metallic lithium and lithium silicide are observed [24]. This substantiates the reaction scheme, in which Li_2O is produced.

The identity of the final material can be further confirmed by X-ray photoelectron spectroscopy (XPS). The survey XPS spectrum (Figure 6a) shows the signals expected for the elements Al, O, Si, and Li, as well as Na and C contaminants. The Si 2p peak position of 102.2 eV (Figure 6b) unambiguously excludes a significant presence of either crystalline Si (99.3 eV) or SiO_2 (103.3 eV) [25], in agreement with the ^{29}Si NMR data. The peak position is compatible with amorphous silicon, the Si 2p XPS line of which has been found at a somewhat more elevated binding energy than for crystalline silicon [26]. The XPS data do not exclude the possible presence or formation of silane or siloxane species in this system, where Si must be mixed with Li_2O intimately. The presence of the latter compound is demonstrated by the Li 1s spectrum (Figure 6c), which within the range from 51 eV to 59 eV displays an absolute maximum at 55.6 eV. For reference, the binding energies [27] of metallic Li (54.7 eV), LiOH (54.9 eV), Li_2CO_3 (55.2 eV), and Li_2O

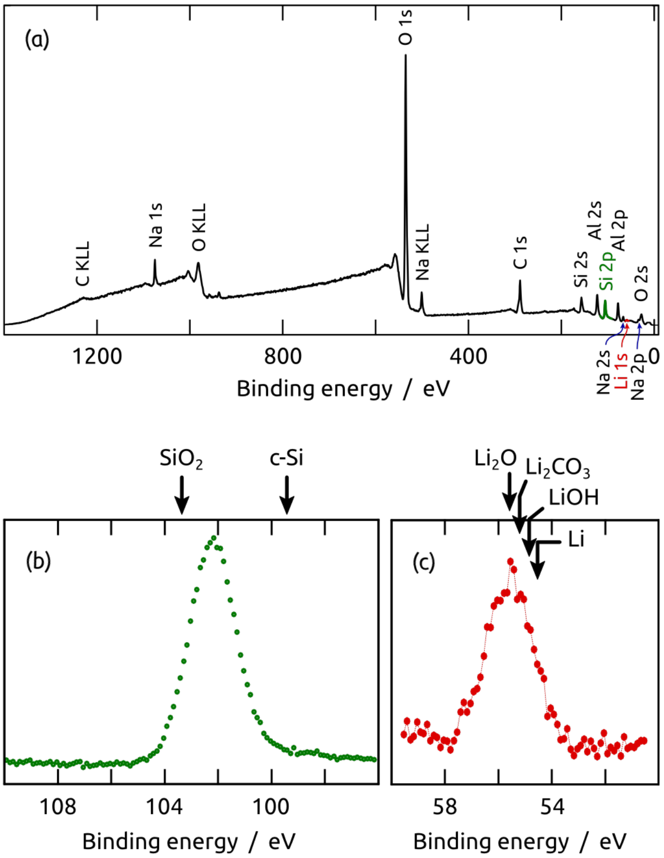

Figure 6: X-ray photoelectron spectrum of a Si nanotube sample at the end of the preparation: (a) survey spectrum, (b) Si 2p peak, and (c) Li 1s peak. The XPS peak positions of reference compounds are given by arrows.

(55.6 eV) are indicated in Figure 6. Some contribution of Li_2CO_3 (due to aerobic CO_2 capture) cannot be excluded, since the C 1s spectrum also suggests the presence of carbonates around 290 eV [25].

Scanning electron microscopy (SEM) provides a morphological check of the samples after all preparative steps have been performed. Indeed, the SEM investigation of a sample in cross-section demonstrates that the morphology has been retained throughout the preparative scheme (Figure S2 in Supporting Information File 1).

The final demonstration of a successful preparation is provided by the functional test. In the present case, this is the observation of a reduction wave at the expected potential in a Li^+-containing electrolyte. The cyclic voltammetry of the lithium/silicon system is typically characterized by a sharp reduction between +0.1 and +0.2 V (vs Li/Li^+) on the charging curve and a broader double oxidation peak situated between +0.3 and +0.7 V upon discharge [6-8]. Upon inclusion as the working electrode into an electrochemical setup with an organic lithium hexafluorophosphate electrolyte and a metallic lithium counter-electrode, our nanotubular silicon samples first display a resting potential on the order of +3.0 V, much more positive than +0.5 V and therefore in line with the chemical identification of the material as elemental silicon above [4]. After the initial charge to +50 mV, slow cyclic voltammetric scans between this value and +3.25 V give rise to the expected curve shape (Figure 7). In fact, the oxidation (discharge) peak appears narrower and at a less positive potential than in most cases reported to date. This could be interpreted as a hint to a particularly good availability of the lithium ions in the solid and their facile extraction out of it, related to the well-defined tubular structure.

Conclusion

A procedure for the preparation of silicon nanotubes as ordered arrays in an inert matrix has been established. The procedure relies on the combination of a nanoporous 'anodic' template with atomic layer deposition. The lack of an ALD reaction for elemental silicon is circumvented in two steps: the ALD of SiO_2 is followed by the crucial reaction, a thermal reduction of silicon dioxide to silicon by lithium vapor. The lithium oxide byproduct is removed subsequently. The reduction, performed under argon at 670 °C, is quantitative, homogeneous and well-behaved, in that the product contains neither remnants of silicon oxide nor any lithium silicide, as demonstrated by ellipsometry, MAS-NMR, and XPS. Finally, cyclic voltammetric investigation of the samples testifies to their function as a negative electrode material for lithium ion batteries.

This novel preparative procedure differs from those available to date for making silicon nanotube arrays in three ways [6-8]. Firstly, it is specifically designed so that the experimentalist can tune the geometry of the tubes, that is, their length, diameter and wall thickness, in a systematic and accurate manner.

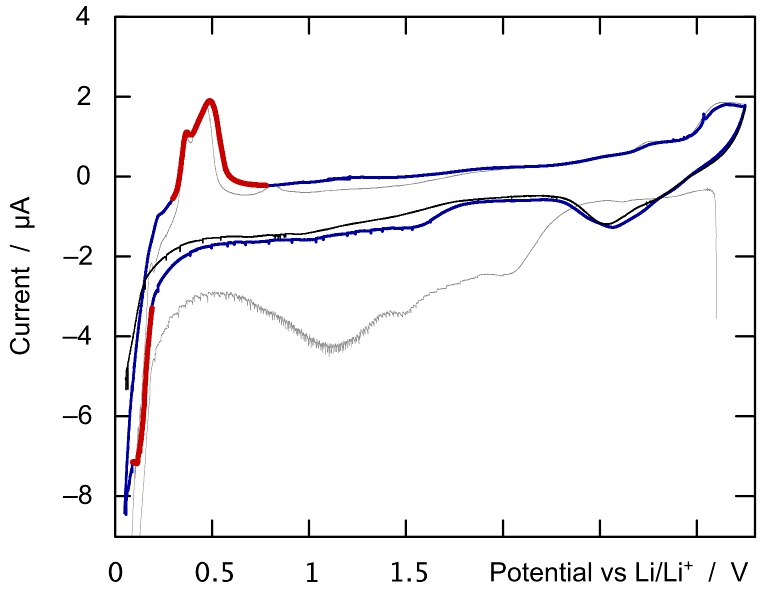

Figure 7: Cyclic voltammetry recorded on a silicon nanotube sample at 0.1 mV s^{-1} in 1 mol L^{-1} $LiPF_6$ in ethylene carbonate/dimethylcarbonate by using metallic lithium as the auxiliary electrode and pseudo-reference. The scans were performed between +3.25 V and +0.05 V. The first cycle is plotted as a thin gray line, the second cycle in blue and red, and the third charge in black. The red color highlights the main reduction (charge) and oxidation (discharge) events of the material.

Secondly, the negative electrode is combined with a membrane separator in a single unit. Thirdly, the discharge takes place at a lower potential than in previous comparable systems, a fact that may be indicative of an unusually good availability of the lithium in the electrode material.

Experimental

Materials

Metallic lithium granules, magnesium powder, 3-aminopropyltriethoxysilane, oxalic acid, phosphoric acid, copper(II) chloride dihydrate, chromium(VI) oxide, ethanol, hydrochloric acid, perchloric acid, argon, and dioxygen, were purchased from commercial suppliers and used as received. Ozone was generated from dioxygen in a generator BMT 803N from BMT Messtechnik. Aluminum (99.999%) was purchased from Goodfellow. Undoped [100] float-zone silicon wafers with 200 nm thermal oxide were obtained from Si-Mat. Water was purified immediately before use in a Millipore Direct-Q system.

Instruments

Atomic layer deposition was carried out in a home-built hot-wall reactor equipped with DP-series pneumatic valves from Swagelok and with an MV10C pump from Vacuubrand. Gold was deposited in a Cressington 108 sputter coater. The high-temperature reactions were performed in home-made thick-walled stainless steel cylinders sealed with copper plates, placed in a muffle furnace, model L3/11/P330 from Nabertherm. The reaction cylinders were loaded under argon in an Innovative Technologies InertLab glovebox. The glovebox was equipped with electrical feedthroughs and was also used for the electrochemical measurements. For these, electrochemical potentiostats from Gamry were used (G300 or Reference 600). The electrolyte was 1 M $LiPF_6$ in 1:1 ethylene carbonate/dimethylcarbonate (LP71 from Merck) and the counter-electrode was a piece of metallic lithium. The voltammetric curves were recorded at 0.1 mV s^{-1} from the open-circuit potential. Spectroscopic ellipsometry data were collected under a 70° incidence angle with an instrument model EL X-02 P Spec from DRE Dr. Riss Ellipsometerbau GmbH from 400 to 1000 nm. Fits were performed by using the database of material files provided with the instrument. Mixed layers were treated with the Lorentz–Lorentz model as implemented in the software of the instrument. Scanning electron micrographs were taken on a Zeiss Evo equipped with LaB_6 cathode or a Zeiss Sigma with field emission. Nuclear magnetic resonance spectra were recorded on a Bruker Avance II 400 spectrometer, equipped with a 4-mm magic angle spinning probe. For ^{29}Si NMR, 10000 free induction decays were collected at 79.52 MHz with 60° pulses of 3.3 μs and delay times of 20 s. ^{7}Li NMR experiments were performed at an operating frequency of 155.56 MHz by using 90° pulses of 3.1 μs and a delay time of 10 s. The ^{29}Si and ^{7}Li spectra were referenced to tetramethylsilane (TMS) at 0 ppm and to a 1 M LiCl solution (aq) at 0 ppm, respectively. All NMR experiments were carried out at room temperatures and at MAS rates of 10 kHz. XPS spectra were recorded by using a PHI 5600ci multitechnique spectrometer with monochromatic Al K ($h\nu$ = 1486.6 eV) radiation of 0.3 eV full width at half maximum. The resolution of the analyzer is 1.5% of the pass energy, i.e, 0.45 eV. All spectra were obtained by using 400-μm-diameter analysis area. During the measurements, the pressure in the main chamber was kept below 5×10^{-9} mbar. Because of the insulating character of the samples, an electrostatic charging effect was observed. All spectra are corrected for this charging effect by using the C 1s line of adsorbed carbon (E_B = 284.8 eV [23]).

Preparation steps (a) to (e)

(a) Anodization was performed in home-made two-electrode cells (Figure S3 in Supporting Information File 1) based on a PVC beaker containing the electrolyte. One or several circular openings are at the bottom of the beaker, under which aluminum plates of 2 cm diameter are held between an O-ring and a thick copper plate functioning as the electrical contact. The cell is closed with a lid that holds a silver wire mesh as the counter-electrode and a mechanical stirrer. The copper plate is in contact with a cold plate connected to a closed-circuit cooler by Haake, whereas the setup is thermally insulated laterally. The aluminium plates were first electropolished for 4 min under +20 V in a solution prepared by mixing one part $HClO_4$ (70%) with three parts EtOH. They were subsequently rinsed, cooled, and anodized under +40 V for 20 h at 7 °C in 3 M oxalic acid. The oxide was removed by treatment with a chromic acid solution (0.18 M CrO_3 in 6 wt % H_3PO_4) for 20 h at 45 °C. The second anodization was carried out for 60 h in the same conditions as the first anodization. (b) The pores were then widened in 5 wt % H_3PO_4 at 45 °C for 10 min. (c) SiO_2 was deposited by ALD at 150 °C in a three-step reaction based on 3-aminopropyltriethoxysilane (heated to 100 °C), water (maintained at 40 °C) and ozone (delivered at room temperature) [15]. The precursor pulse, exposure and pumping durations were 2/60/90 s, 0.5/60/90 s, and 0.2/60/90 s for the three steps, respectively. (d) The aluminum substrate was subsequently removed by treatment with a 0.7 M $CuCl_2$ solution in 10% HCl. The metallic Cu byproduct was removed with concentrated nitric acid. (e) The barrier layer of Al_2O_3 closing the pore extremities was opened in 5 wt % H_3PO_4 (45 °C, 10 min), after which the samples were dried for 4 h at 400 °C in air.

Thermal reductions of SiO_2 and subsequent steps

When flat films (thermal oxide layer on Si wafer pieces) were used as a starting material, their thickness was determined accurately by spectroscopic ellipsometry before reaction. (f) In a glovebox operated under argon, the silicon wafer pieces or nanoporous samples were placed into a stainless steel crucible of approximately 5 × 8 mm^2 and inserted into a stainless steel cylinder of 10 mm inner diameter, 60 mm length, and 4 mm wall thickness. The magnesium powder or lithium granules were loaded into another crucible and inserted next to the first. The cylinder was closed with two screw nuts sealed with copper plates. A high-temperature copper paste (LiquiMoly 3080) was used to lubricate the screw threads. The sealed cylinder was then heated to the desired reaction temperature (usually 670 or 700 °C) in an oven flushed with nitrogen for several hours (7 h or more), then cooled to room temperature and opened in air. (g) The lithium oxide byproduct was removed by dipping in 1 M aqueous HCl solution for 4 h at room temperature. (h) For electrochemical measurements, a thin gold contact (approximately 50 nm) was finally sputtered onto one side of the sample.

Supporting Information

The Supporting Information File contains the three Figures S1–S3 mentioned in the text.

Supporting Information File 1

Additional Figures.
[http://www.beilstein-journals.org/bjnano/content/supplementary/2190-4286-4-73-S1.pdf]

Acknowledgements

This research was supported in part by the cluster of excellence ‘Engineering of Advanced Materials’.

References

1. Whittingham, M. S. *Chem. Rev.* **2004,** *104,* 4271–4302. doi:10.1021/cr020731c
2. Wakihara, M. *Mater. Sci. Eng., R* **2001,** *33,* 109–134. doi:10.1016/S0927-796X(01)00030-4
3. Nikolaev, V. P.; Morachevskii, A. G.; Demidov, A. I.; Bairachnyi, E. V. *Russ. J. Appl. Chem.* **1980,** *53,* 1549–1551.
4. Cairns, E. J.; Albertus, P. *Annu. Rev. Chem. Biomol. Eng.* **2010,** *1,* 299–320. doi:10.1146/annurev-chembioeng-073009-100942
5. Boukamp, B. A.; Lesh, G. C.; Huggins, R. A. *J. Electrochem. Soc.* **1981,** *128,* 725–729. doi:10.1149/1.2127495
6. Song, T.; Xia, J.; Lee, J.-H.; Hyun Lee, D.; Kwon, M.-S.; Choi, J.-M.; Wu, J.; Doo, S. K.; Chang, H.; Park, W. I.; Zang, D. S.; Kim, H.; Huang, Y.; Hwang, K.-C.; Rogers, J. A.; Paik, U. *Nano Lett.* **2010,** *10,* 1710–1716. doi:10.1021/nl100086e
7. Ge, M. Y.; Rong, J. P.; Fang, X.; Zhou, C. W. *Nano Lett.* **2012,** *12,* 2318–2323. doi:10.1021/nl300206e
8. Chan, C. K.; Peng, H.; Liu, G.; McIlwrath, K.; Zhang, X. F.; Huggins, R. A.; Cui, Y. *Nat. Nanotechnol.* **2008,** *3,* 31–35. doi:10.1038/nnano.2007.411
9. Shin, H.-C.; Corno, J. A.; Gole, J. L.; Liu, M. L. *J. Power Sources* **2005,** *139,* 314–320. doi:10.1016/j.jpowsour.2004.06.073
10. Masuda, H.; Tanaka, H.; Baba, N. *Chem. Lett.* **1990,** *19,* 621–622. doi:10.1246/cl.1990.621
11. Nielsch, K.; Choi, J.; Schwirn, K.; Wehrspohn, R. B.; Gösele, U. *Nano Lett.* **2002,** *2,* 677–680. doi:10.1021/nl025537k
12. Elam, J. W.; Routkevitch, D.; Mardilovich, P. P.; George, S. M. *Chem. Mater.* **2003,** *15,* 3507–3517. doi:10.1021/cm0303080
13. Bachmann, J.; Jing, J.; Knez, M.; Barth, S.; Shen, H.; Mathur, S.; Gösele, U.; Nielsch, K. *J. Am. Chem. Soc.* **2007,** *129,* 9554–9555. doi:10.1021/ja072465w
14. Gemmer, J.; Hinrichsen, Y.; Abel, A.; Bachmann, J. *J. Catal.* **2012,** *290,* 220–224. doi:10.1016/j.jcat.2012.03.022
15. Wedemeyer, H.; Michels, J.; Chmielowski, R.; Bourdais, S.; Muto, T.; Sugiura, M.; Dennler, G.; Bachmann, J. *Energy Environ. Sci.* **2013,** *6,* 67–71. doi:10.1039/c2ee23205g
16. Leskelä, M.; Ritala, M. *Angew. Chem., Int. Ed.* **2003,** *42,* 5548–5554. doi:10.1002/anie.200301652
17. Bachmann, J.; Zierold, R.; Chong, Y. T.; Hauert, R.; Sturm, C.; Schmidt-Grund, R.; Rheinländer, B.; Grundmann, M.; Gösele, U.; Nielsch, K. *Angew. Chem., Int. Ed.* **2008,** *47,* 6177–6179. doi:10.1002/anie.200800245
18. Hiller, D.; Zierold, R.; Bachmann, J.; Alexe, M.; Yang, Y.; Gerlach, J. W.; Stesmans, A.; Jivanescu, M.; Müller, U.; Vogt, J.; Hilmer, H.; Löper, P.; Künle, M.; Munnik, F.; Nielsch, K.; Zacharias, M. *J. Appl. Phys.* **2010,** *107,* 064314. doi:10.1063/1.3327430
19. Gordon, R. G.; Hausmann, D.; Kim, E.; Shepard, J. *Chem. Vap. Deposition* **2003,** *9,* 73–78. doi:10.1002/cvde.200390005
20. Dendooven, J.; Deduytsche, D.; Musschoot, J.; Vanmeirhaeghe, R. L.; Detavernier, C. *J. Electrochem. Soc.* **2009,** *156,* P63–P67. doi:10.1149/1.3072694
21. Bao, Z.; Weatherspoon, M. R.; Shian, S.; Cai, Y.; Graham, P. D.; Allan, S. M.; Ahmad, G.; Dickerson, M. B.; Church, B. C.; Kang, Z. T.; Abernathy, H. W., III; Summers, C. J.; Liu, M. L.; Sandhage, K. H. *Nature* **2007,** *446,* 172–175. doi:10.1038/nature05570
22. Lide, D. R., Ed. *CRC Handbook of Chemistry and Physics,* 73rd ed.; CRC Press, 1992.
    Base for thermodynamic data. Calculated under the assumption of temperature-independent $\Delta_r S°$ and $\Delta_r H°$.
23. Lippmaa, E.; Mägi, M.; Samoson, A.; Engelhardt, G.; Grimmer, A.-R. *J. Am. Chem. Soc.* **1980,** *102,* 4889–4893. doi:10.1021/ja00535a008
24. Key, B.; Bhattacharyya, R.; Morcrette, M.; Seznéc, V.; Tarascon, J.-M.; Grey, C. P. *J. Am. Chem. Soc.* **2009,** *131,* 9239–9249. doi:10.1021/ja8086278
25. Chastain, J., Ed. *Handbook of X-ray Photoelectron Spectroscopy;* Perkin Elmer Cooperation: Eden Prairie, Minnesota, USA, 1992.
26. Nishimatsu, R.; Sluiter, M.; Mizuseki, H.; Kawazoe, Y.; Sato, Y.; Miyata, M.; Uehara, M. *Physica B* **2003,** *340–342,* 570–574. doi:10.1016/j.physb.2003.09.133
27. Contour, J. P.; Salesse, A.; Froment, M.; Garreau, M.; Thevenin, J.; Warin, D. *J. Microsc. Spectrosc. Electron.* **1979,** *4,* 483–491.

License and Terms

Beilstein Journal
of Nanotechnology

Evolution of microstructure and related optical properties of ZnO grown by atomic layer deposition

Adib Abou Chaaya[1,§], Roman Viter[*2,3,§], Mikhael Bechelany[*1,¶],
Zanda Alute[2], Donats Erts[4], Anastasiya Zalesskaya[2], Kristaps Kovalevskis[3],
Vincent Rouessac[1], Valentyn Smyntyna[2] and Philippe Miele[1]

Full Research Paper

Address:
[1]European institute of membranes (IEM, ENSCM-UM2-CNRS, UMR 5635), University of Montpellier 2, Place Eugène Bataillon, F-34095, Montpellier, France, [2]Faculty of Physics, Odessa National I.I. Mechnikov University, 42, Pastera, 65026, Odessa, Ukraine, [3]Institute of Atomic Physics and Spectroscopy & Institute of Chemical Physics, University of Latvia, 19, Raina Blvd., LV 1586, Riga, Latvia, and [4]Institute of Chemical Physics, University of Latvia, 19, Raina Blvd., LV 1586, Riga, Latvia

Email:
Roman Viter* - viter_r@mail.ru;
Mikhael Bechelany* - mikhael.bechelany@univ-montp2.fr

* Corresponding author
§ These authors contributed equally to the paper
¶ Phone. +33 4 67 14 91 67, Fax. +33 4 67 14 91 19

Keywords:
atomic layer deposition; optical properties; photoluminescence; thin films; ZnO

Beilstein J. Nanotechnol. **2013,** *4,* 690–698.
doi:10.3762/bjnano.4.78

Received: 24 July 2013
Accepted: 01 October 2013
Published: 28 October 2013

This article is part of the Thematic Series "Energy conversion applications of atomic layer deposition".

Guest Editor: J. Bachmann

Abstract

A study of transmittance and photoluminescence spectra on the growth of oxygen-rich ultra-thin ZnO films prepared by atomic layer deposition is reported. The structural transition from an amorphous to a polycrystalline state is observed upon increasing the thickness. The unusual behavior of the energy gap with thickness reflected by optical properties is attributed to the improvement of the crystalline structure resulting from a decreasing concentration of point defects at the growth of grains. The spectra of UV and visible photoluminescence emissions correspond to transitions near the band-edge and defect-related transitions. Additional emissions were observed from band-tail states near the edge. A high oxygen ratio and variable optical properties could be attractive for an application of atomic layer deposition (ALD) deposited ultrathin ZnO films in optical sensors and biosensors.

Introduction

Zinc oxide (ZnO) is an n-type semiconductor and a transparent conductive oxide (TCO) with excellent optoelectronic properties, a wide band gap (3.36 eV), a high dielectric constant, a high exciton binding energy (60 meV), and a high thermal stability [1]. Hence it is an important material for different applications in devices such as gas sensors [2], biosensors [3], transducers [4], solar cells [5-7], electronic and optoelectronic instruments (i.e., ultraviolet photo-detectors) [8], surface acoustic wave (SAW) gadgets [9], and transparent electrodes [10]. ZnO crystals with a grain size in the range of 1–50 nm have demonstrated optical properties, such as an UV shift of the absorption edge and strong photoluminescence at room temperature caused by quantum confinement [11] and, an improvement of the photovoltaic and sensor performance due to a high surface area [12,13]. ZnO nanostructures are obtained as nanoparticles [14], nanotubes [15], nanowires [5,7], and ultrathin films [16,17]. Ultrathin ZnO films can be synthesized by different deposition techniques such as sol–gel [18], chemical vapor deposition [19], electro-deposition [5-7], RF sputtering, and atomic layer deposition (ALD) [16,17].

It is well known that the optoelectronic properties of zinc oxide thin film [20,21] are strongly dependent on the structure [11,22]. Crystallinity and stochiometry of the film determine the concentration of point defects (zinc and oxygen vacancies, interstitial zinc and oxygen) [20]. The band gap of ZnO nanostructures decreases from 3.29 to 3.23 eV with an increase of the grain size [21]. The electrical conductivity of ZnO is affected by a defect concentration and diminishes at annealing in an oxygen environment (oxygen vacancy healing) [21].

One of the methods applied to analyze the crystalline structure and defect level in zinc oxide is photoluminescence. It has been shown that ZnO exhibits a narrow UV emission band in the 378–381 nm range and a broad emission band in the range of 480–620 nm [23-25]. The UV emission band in ZnO has been related to exciton emission, whereas the vis emission has been related to radiative transitions involving intrinsic point defects (O/Zn vacancies and O/Zn interstitials) [23-25].

ALD is an innovative deposition technique which allows depositing ultrathin metal oxide films with preferred thickness, grain size, chemical composition, texture, surface morphology, and defect concentration [26]. The mentioned structural parameters make a strong impact on optical, electrical and additional properties [16,17].

In this paper results of a study on tuning the optical properties (absorption and photoluminescence) along with impacts on grain size, texture, and strain at varying thickness of ultrathin ZnO films are reported. We also discuss our findings with regard to their potential usefulness for applications in photovoltaics [5,27], photocatalytics [16], sensors [16] and biosensors [28-30].

Results and Discussion

Chemical and structural characterizations

ZnO films with a thickness of 25, 49.8, 124 and 250 nm were obtained at 100, 200, 500 and 1000 deposition cycles, respectively. The average growth rate calculated from all results is 2.5 Å per cycle. Results of ellipsometric measurements are presented in Table 1.

SEM images of ZnO thin films grown by ALD on Si substrates at 200, 500, and 1000 cycles are shown in Figure 1a. The images indicate conformal coating of the Si substrate. A rough surface of columnar growth of the films develops with an increase of the film thickness. Cross section images of the same ZnO samples (Figure 1a and Supporting Information File 1, Figure S1) confirm the ellipsometric results.

EDX measurements were carried out to evaluate the chemical composition of ALD ZnO films deposited on Si substrates. The results of these measurements are presented in Figure 1b. An analysis of these results shows that in all the studied ZnO films grown at 100 °C the ratio of O/Zn exceeds 1. This might be caused by the presence of residual OH^- and a partially hydroxylated phase ZnO(OH) on the surface of the ZnO grains due to an incomplete removal of excess H_2O at such a low temperature or

Table 1: Thickness of ZnO thin films measured by SEM and ellipseometry. Content of Zn and O estimated from EDX analysis.

ZnO number of cycles	Thickness (nm) measured by ellipsometry	Thickness (nm) measured by SEM	O content (atom %)	Zn content (atom %)	O/Zn ratio
100	25	23	66	33	2
200	49.8	45	63	37	1.7
500	124	120	58	42	1.38
1000	250	241	56	44	1.27

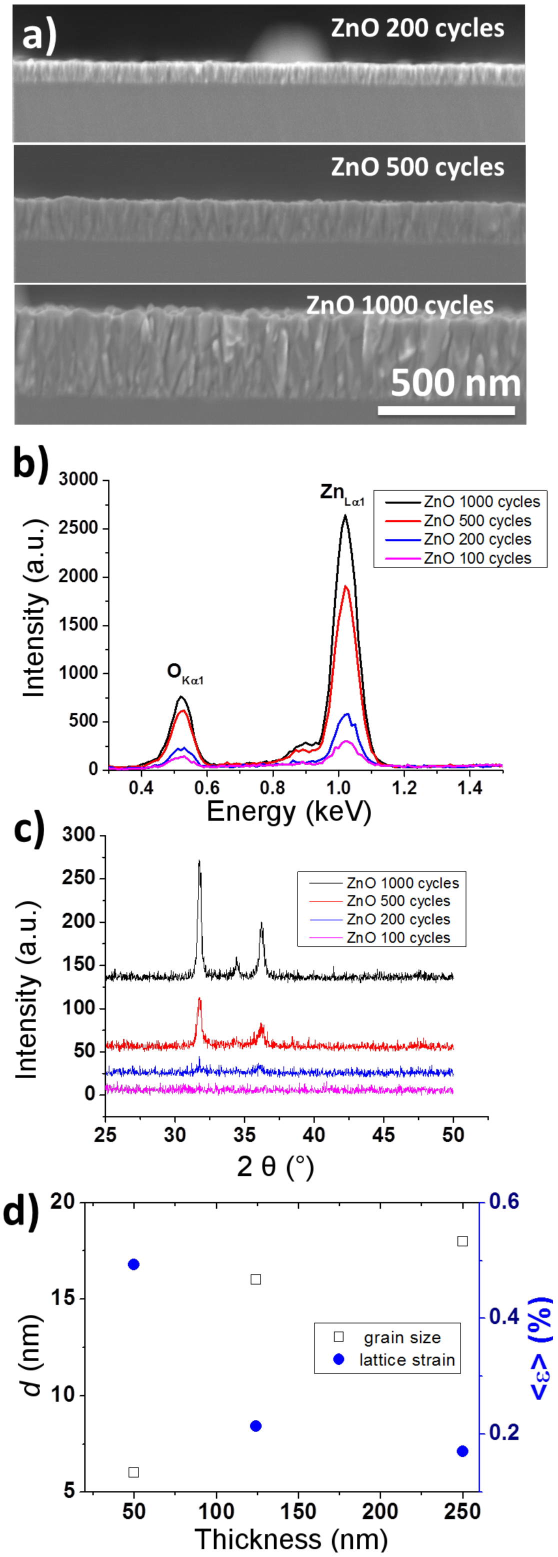

Figure 1: a) SEM images of a cross section of ZnO ALD films deposited on Si substrates by 200, 500, and 1000 cycles; b) EDX; c) GIXRD of ZnO ALD films deposited by 100, 200, 500, and 1000 cycles; d) grain size and lattice strain in ZnO ALD films of different thickness.

a fraction of unreacted hydroxyl groups observed earlier [31,32]. However, as the layers of ZnO are too thin the FTIR results do not confirm the presence of OH groups (Supporting Information File 1, Figure S2). We also did not detect any carbon that remained from the deposition process. Table 1 shows that the O/Zn ratio decreases with increasing thickness.

GIXRD diffraction patterns of thin ZnO films are shown in Figure 1c. The X-ray diffraction from the thinnest samples (25 nm) does not display any peaks. This indicates either an amorphous structure or small (<4 nm) grains [27]. Weak XRD peaks at $2\theta = 31.74$ and 36.22° corresponding to (100) and (101) reflections of ZnO, respectively, appear in 49.8 nm thick samples and become distinctly pronounced strong reflections in 124 and 250 nm thick samples. An XRD peak of low intensity at $2\theta = 34.42°$ is observed from thick films. Lattice constants calculated from GIXRD spectra of 49.8, 124, and 250 nm thick ZnO films are equal to $a = 0.325$ nm and $c = 0.52$ nm. No significant changes of lattice parameters are observed with increasing film thickness. The maximum values of the texture coefficients (TC) of 49.8, 124, and 250 nm thick ZnO films calculated according to Rivera et al. [33] (1.2, 1.66 and 2.12, respectively) match the preferred growth in the [100] direction. Calculations of the average grain size and lattice strain by the Warren–Averbach techniques with WinFit software show that the growth of the ZnO layers is assisted by a growth of grains and a decrease of lattice strain (Figure 1d).

Surface morphology of the samples was studied by atomic force microscopy (Figure 2a). Samples with a thickness of less than 100 nm have a smooth surface did not feature a significant roughness. Well shaped 100–150 nm elevations are observed on surfaces of thicker samples. The mean-square roughness, calculated from AFM data, has a non-linear (positively accelerated) relationship with the thickness (Figure 2b).

Figure S3 (Supporting Information File 1) shows the TEM cross-sectional analysis of 250 nm thick ZnO. An amorphous ZnO layer is observed at a thickness below 20 nm. No columnar grains are present on the surface of 20 to 50 nm thick films. The grains are mostly randomly oriented thereby indicating that the nano-crystalline grains in the ultrathin (20–50 nm thick) ZnO films are surrounded by amorphous pockets. This finding is consistent with earlier results [34]. The columnar growth is observed in ZnO films thicker than 50 nm. The studied columnar structures have amorphous ZnO surroundings.

Thus, the structure of ZnO ALD films strongly depends on the thickness. The ZnO samples obtained by 100 cycles were amorphous, had a smooth surface, and did not exhibit any XRD peaks. The increase of the film thickness was assisted by the

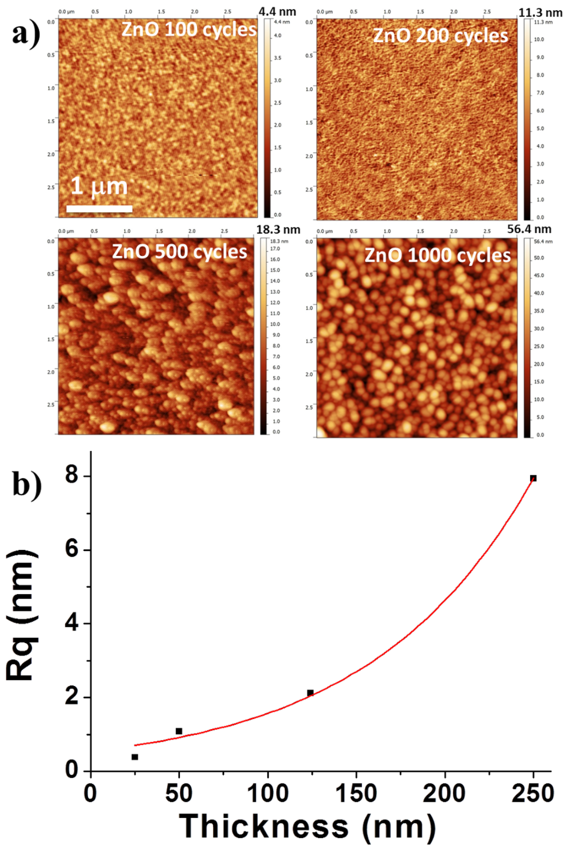

Figure 2: a) AFM images of the size of 3 × 3 µm^2 of ZnO thin films deposited by 100, 200, 500 and 1000 cycles. b) Roughness as a function of the film thickness.

growth of vertically oriented columns with well-defined boundaries, an improvement of the crystalline structure (narrowing of XRD peaks), a crystalline growth and an alleviation of lattice strain, and an enhancement of the surface roughness and the texture coefficient.

Optical properties

Transmittance spectra. Transmittance spectra of the samples are shown in Figure 3a. ZnO films with a thickness of less than 100nm are transparent in the 500–1100 nm range. Observed transmittance maxima and minima in the spectra of films with a thickness of more than 100 nm match the interference patterns. Since ZnO is an n-type semiconductor of direct optical transitions the optical density D is calculated as:

$$D = \ln\left(\frac{1}{T}\right) \tag{1}$$

where T is the optical transmittance. The optical density D is related to the band gap E_g by proportion [35]:

$$(D \cdot h\nu)^2 \sim (h\nu - E_g) \tag{2}$$

where $h\nu$ is the photon energy, and E_g is the band gap. Graphically estimated band gap values of thin ZnO films are shown in Figure 3c. The obtained values are lower than the value typical of a ZnO single crystal ($E_g = 3.37$ eV). This difference might be caused by the number of point defects (vacancies and interstitials of Zn and O) [36]. There is a non-typical dependence of the band gap value on the grain size. The small increase of the band gap value with the film thickness may be related to an improvement of the crystalline structure of deposited samples.

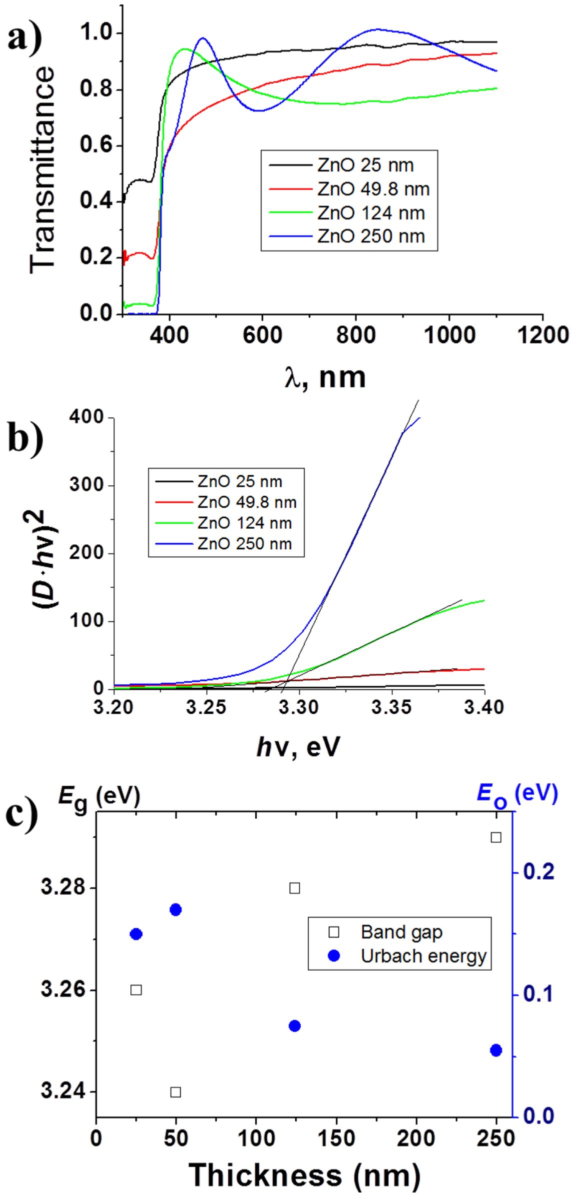

Figure 3: a) Transmittance spectra, b) band gap estimation, and c) band gap and Urbach energies of ZnO ALD films of different thickness.

The structure of 25 nm thick films is amorphous. The films might contain crystallites with a size of less than 3 nm which are difficult to detect by XRD. In this case, a band gap broadening due to the quantum confinement effect would be expected. However, results obtained from 25 nm films do not show any significant increase of the band gap value. This hints at an absence of small crystallites in the amorphous structure of the films.

Because of the disorder in amorphous and highly doped semiconductors, the absorption or the optical density D near the band edge is an exponential function of the photon energy as described by the Urbach law [37]:

$$D = D_0 \cdot \exp\left(\frac{h\nu}{E_0}\right) \qquad (3)$$

where E_0 is the Urbach energy interpreted as the width of the tail of the states localized close to the conductance band in the forbidden zone. Numerical calculations show a decrease of the Urbach energy while matching the thickness with an advancement of the crystalline structures. This finding correlates well with XRD data.

Photoluminescence and absorption spectra. The penetration depth of the laser spot in the ALD deposited thin films estimated from transmittance data according to the Beer–Lambert law was about 40 to 44 nm [38]. The latter means that the photoluminescence has an impact from the bulk and the surface of the samples. We suppose that the grain size could play a crucial role in the emitting properties, especially in thicker samples. The 3.08–3.30 eV UV and 1.80–2.28 eV vis emission bands are observed in PL spectra of all ultra-thin ZnO films (Figure 4a–d). The intensity is increasing with the thickness, so it can be controlled by the amount of ZnO material [39].

The shapes of the PL bands fit to a Gaussian peak function by the Origin 7.0 software are presented in Figure S4 of Supporting Information File 1. The main difference between Gaussian and a Lorentz profile is the long tails in the latter case [40] where a lot of the overall intensity is ‘hidden’ in the tails.

Obtained values of the absorption and positions of the PL peaks are shown in Table 2. An analysis of the absorption and the emission shows that the 3.28–3.30 eV PL in the region of the absorption edge is related to band–band transitions [41]. The 3.21–3.24 eV peaks are due to transitions in the band-tail states of ZnO [42]. The observed 3.21–3.24 eV emission belong to electron transitions from tail states of the conduction band to tail states of the valence band [43]. The 3.08–3.14 eV UV peaks correspond to defect states formed by neutral Zn vacancies (V(Zn)0) [44].

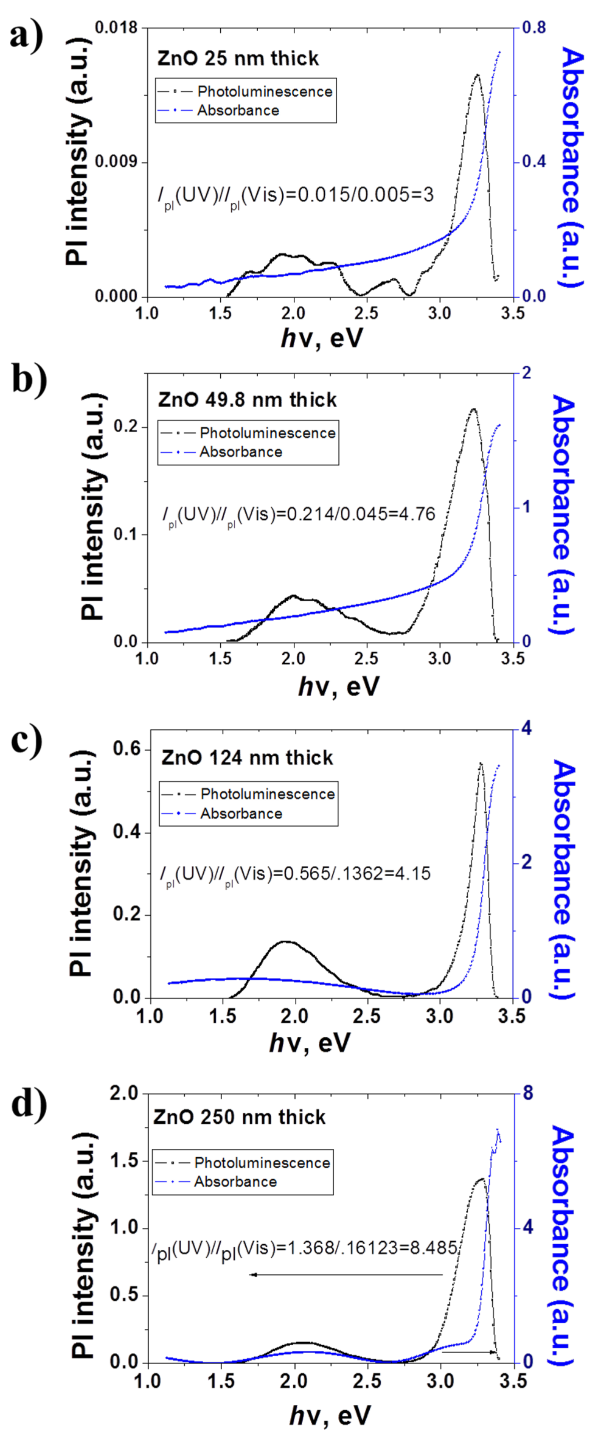

Figure 4: PL and absorption spectra of 25 (a), 49.8 (b), 124 (c), and 250 nm (d) thick ZnO ALD films.

The emission in the visible is caused by point defects [45]. The 2.21–2.25 eV peaks are attributed to oxygen interstitials (O_i)

Table 2: Positions of absorption and PL peaks of ZnO thin films of different thickness.

Thickness (nm)	Peak positions			
	$V(O^{++})$ (eV)	(O_i) (eV)	$V(Zn^0)$ (eV)	Band tail states (eV)
25	2.01103	—	3.08374	3.21019
49.8	1.96819	2.24953	3.09573	3.22453
124	1.88601	2.12068	3.14621	3.24162
250	2.01575	2.24768	3.12942	3.2352

[44,46,47]. According to Wang et al. [18], emission bands at 1.9–2.0 eV of ZnO ALD ultrathin films are due to doubly ionized oxygen vacancies ($V(O)^{++}$) [48]. The PL spectra correlate with the absorption spectra. Absorption spectra have tails and peaks in the 3.2–1.78 eV range matching the optical transitions defect state-valence band and the defect state-conduction band (Figure 4a–d) [49-52]. The binding energy of free exciton in ZnO is 0.06 eV. The exciton emission energy E_x and the energy gap E_g are correlated [53]:

$$E_x = E_g - E_b + \frac{\hbar^2 \cdot k^2}{2 \cdot m_{ex}} \qquad (4)$$

where, E_b , $\hbar$, k, m_{ex} are the exciton binding energy, Planck's constant, wave vector, and effective mass of the exciton, respectively. Since ZnO is a direct band gap semiconductor, the wave vector $k = 0$ and the value of the energy gap of the samples, according to Equation 4, is around 3.35–3.36 eV. The difference between the estimations and the experimental data is due to structural defects.

Correlation between optical and structural properties. The optical properties of ultrathin ZnO films are tailored by structural parameters (grain size, stoichiometry, etc.). A strong relation between the crystalline structures and photoluminescence of ZnO is described by the intensity ratio of the UV–vis PL bands [20].

In the present study the calculated UV–vis ratio of the PL band intensities of ZnO increase with the growth of film thickness. This may be associated with:

1. improvement of the stoichiometry and the structure of ZnO crystallites
2. grain growth and decreasing number of point effects
3. decreasing bend of the surface band as a result of an increasing grain size.

The structural characterization (GIXRD) shows an improvement of the crystalline structure with the thickness. The EDX results show a monotonous decrease of the O/Zn ratio with a growth of the film while remaining greater than unity, which points to an oxygen-rich stoichiometry of the studied samples. In oxygen-rich films Zn vacancies, oxygen interstitials and oxygen interstates can be formed [46]. The excess oxygen may also localize on grain boundaries to form a negative surface charge [54] and depletion layer. The electric field of the surface charge in the depletion layer would stimulate dissociation of excitons in ZnO [18,48].

The absorption spectra of ultrathin ZnO ALD films show that the defect states are present in the gap. The defect states at 3.08–3.14 eV formed by neutral Zn vacancies and oxygen interstitials at 2.21–2.25 eV identified in PL spectra of oxygen-rich samples correlate well with the EDX results. Doubly ionized oxygen vacancies show up in the PL spectra of all samples at 1.9–2.0 eV pointing to the active role of surface effects in the emission spectra.

An increasing thickness during the film growth stimulates an improvement of the crystalline structure related to a widening of the energy gap, an increasing intensity of the UV emission, and a decrease of the Urbach energy. An increase of the grain size induced a decrease of the active surface area and affects the concentration of oxygen adsorbed on the grain surface. Therefore, a growing UV–vis intensity ratio in ZnO PL being observed (Figure 5) a decrease of the bending of surface band and the depletion layer is expected if the UV–vis intensity ratio grows in ZnO PL.

The photo-generated electrons and holes are known to be separated by a strong electric field in the depletion region formed by the surface charge [55,56]. The negative charge at the surface and the band bending upward are primarily caused by the adsorbed species (oxygen, hydroxyl groups, etc.) [55,56].

Under steady-state conditions the equilibrium is achieved between the flow of holes to the surface and the flow of elec-

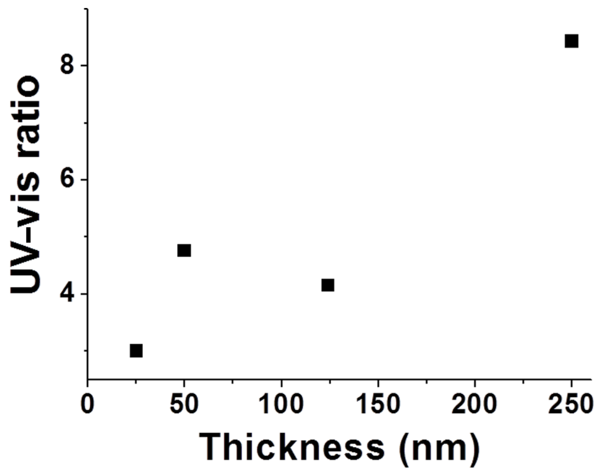

Figure 5: UV–vis intensity ratio of ZnO ALD films of different thickness.

trons to the "bulk" region [56]. The holes reaching the surface reduce the surface charge and, therefore, the bending of the surface band. As a result, the near-surface electric field and the width of the depletion region decrease with increasing intensity of the excitonic PL.

Liao et al. [48] and Wang et al. [18] report that the decrease of the depletion layer in ZnO nanostructures are capable to stimulate transitions between neutral, single-charged, and doubly ionized oxygen vacancies assisted by a UV shift of the visible emission. The neutral oxygen vacancies are located in the bulk, whereas the doubly ionized vacancies are located in the depleted region.

However, in the present study neither the UV shift of the visible emission, nor emission peaks corresponding to neutral oxygen vacancies have been observed. The UV–vis ratio facilitates the discrimination between completely depleted (UV–vis ratio significantly smaller than unity) and partially depleted ZnO grains (UV–vis ratio greater than unity) [18,48]. Since the UV–vis ratio exceeds unity in all measured cases the samples should contain partially depleted grains. Thus, the oxygen vacancies may be formed as point defects mostly in the surface region in an oxygen rich environment, and the concentration in the bulk of the grains may be negligible. Therefore, the change of the width of the depleted layer should not affect emission from oxygen vacancies.

Conclusion

As the thickness of oxygen-rich ultra-thin ZnO films is grown by atomic layer deposition from 25 nm to 250 nm a structural transition from the amorphous to the polycrystalline state occurs. The increase of the size of the crystalline grains at consecutive deposition cycles is accompanied by a decrease of lattice strain, a rise of the Zn/O ratio, and an uncharacteristic change of the energy gap. This uncharacteristic change of the energy gap is explained by a result of the decreasing concentration of point defects, i.e., an improved crystalline structure. Compared with the bulk ZnO crystals the values of the energy gap of the films are lower due to structural defects. The observed UV and visible photoluminescence emissions in the films correspond to band-edge and defect-related transitions, respectively. Additional UV emissions are observed from band-tail states. The defects related to observed PL bands are identified as neutral Zn vacancies, interstitial oxygen, and doubly ionized oxygen vacancies. The optical properties correlate with the crystalline structure, the point defect concentration, the grain size, and the depleted layer.

An increased intensity of the UV emissions reflects an improvement of the crystalline structure with a growing size of the grains. A narrowing of the depleted layer which does not affect the visible emissions is attributed to a low bulk concentration of oxygen vacancies mainly located on grain boundaries. The oxygen excess is attributed to the formation of Zn vacancies, oxygen interstitials and adsorbed molecular oxygen on the surface of grains. The ultra-thin ZnO ALD films are attractive for optical sensor/biosensor applications due to their high oxygen to zinc ratio and variable optical properties. In addition, the presence of hydroxyl terminals leads to the hydrophilicity of the films and improves the immobilization of selected kinds of bio-molecules, thus increasing the suitability for biosensor applications.

Experimental

Synthesis of ZnO thin films by ALD

Diethyl zinc (DEZ) ($Zn(CH_2CH_3)_2$, 95% purity, CAS: 557-20-0) purchased from Sterm Chemical, a p-type silicon(100) wafer obtained from the Korean MEMC company, ITO substrates from Sigma Aldrich, and glass substrates from RS (France) were used to prepare the samples for this study. In order to remove organic contaminants the substrates were precleaned in acetone, ethanol and de-ionized water for 5 min. A tailored ALD reactor [57] was used for the synthesis of ZnO. The ALD was performed by sequential exposures of DEZ and H_2O separated by nitrogen purge at a flow rate of 100 standard cubic centimeters per minute (sccm). The regime for the deposition of ZnO consisted of 0.1 s pulses of DEZ, 20 s of exposure to DEZ, 40 s of nitrogen purge followed by 2 s pulse of H_2O, 30 s exposure to H_2O, and a final 60 s nitrogen purge. ZnO films with 100, 200, 500, and 1000 ALD cycles were deposited on Si and glass substrates to study the influence of the thickness. The temperature was fixed at 100 °C.

Characterization

Structural properties of the ZnO films were characterized by scanning electron microscopy (SEM), ellipsometry, energy-dispersive X-ray spectroscopy (EDX), and grazing incidence X-ray diffraction (GIXRD). An Asylum Research MFP-3D atomic force microscope equipped with a commercial silicon tip was operated in the tapping mode to study the surface morphology on images of the size of 3 µm × 3 µm. SEM and EDX characterization of the samples were performed by using a Hitachi S-4800 microscope and EDX on Hitachi S-4500 coupled with a Thermofisher EDX detector, respectively. Thickness of the ZnO films were measured by a Semilab GES5E spectroscopic ellipsometer (of extended visible range: 1.23–5 eV) under conditions of a fixed incident angle of 75° close to the Brewster's angle of silicon substrate, and variable wavelength between 300 nm and 1 µm. Winelli II software was used to fit the experimental $\tan(\psi)$ and $\cos(\delta)$ data in the full wavelength range by using Cauchy dispersion law and a single-layer ZnO adjusted model to obtain the film thickness. A Bruker D5000 instrument was used for structural GIXRD characterizations.

A Shimadzu UV-1700 spectrophotometer was used to study the optical properties of ZnO thin films by 1 nm steps over the 300–1100 nm range, and photoluminescence in the 370–800 nm range. A solid state LCS-DTL-374QT Nd:YAG 355 nm laser source (Russia) at the intensity of 19 mW/cm^2 was used to excite the luminescence. Emission spectra were registered by the experimental setup described by Viter et al. [58].

Supporting Information

Supporting Information File 1

Additional figures.
[http://www.beilstein-journals.org/bjnano/content/supplementary/2190-4286-4-78-S1.pdf]

Acknowledgements

The study was partially supported by the EU grant under BIOSENSORS-AGRICULT, Contract PIRSES-GA-2012-318520 "DEVELOPMENT OF NANOTECHNOLOGY BASED BIOSENSORS FOR AGRICULTURE". The authors are thankful to Dr. Janis Abolins for scientific discussion and language correction.

References

1. Özgür, Ü.; Alivov, Ya. I.; Liu, C.; Teke, A.; Reshchikov, M. A.; Doğan, S.; Avrutin, V.; Cho, S.-J.; Morkoç, H. *J. Appl. Phys.* **2005,** *98,* 041301. doi:10.1063/1.1992666
2. Chou, S. M.; Teoh, L. G.; Lai, W. H.; Su, Y. H.; Hon, M. H. *Sensors* **2006,** *6,* 1420–1427. doi:10.3390/s6101420
3. Zhao, Z.; Lei, W.; Zhang, X.; Wang, B.; Jiang, H. *Sensors* **2010,** *10,* 1216–1231. doi:10.3390/s100201216
4. Srivastava, J. K.; Agarwal, L.; Bhattacharyya, A. B. *J. Electrochem. Soc.* **1989,** *136,* 3414–3417. doi:10.1149/1.2096463
5. Elias, J.; Bechelany, M.; Utke, I.; Erni, R.; Hosseini, D.; Michler, J.; Philippe, L. *Nano Energy* **2012,** *1,* 696–705. doi:10.1016/j.nanoen.2012.07.002
6. Elias, J.; Levy-Clement, C.; Bechelany, M.; Michler, J.; Philippe, L. Well ordered Hollow Urchin-like ZnO by Electrodeposition. In *Electroless Deposition Principles, Activation, and Applications;* Djokic, S.; Stickney, J. L., Eds.; 2011; Vol. 33, pp 67–73.
7. Elias, J.; Lévy-Clément, C.; Bechelany, M.; Michler, J.; Wang, G.-Y.; Wang, Z.; Philippe, L. *Adv. Mater.* **2010,** *22,* 1607–1612. doi:10.1002/adma.200903098
8. Bae, H. S.; Im, S. *Thin Solid Films* **2004,** *469–470,* 75–79. doi:10.1016/j.tsf.2004.06.196
9. Muthukumar, S.; Gorla, C. R.; Emanetoglu, N. W.; Liang, S.; Lu, Y. *J. Cryst. Growth* **2001,** *225,* 197–201. doi:10.1016/S0022-0248(01)00874-0
10. Assunção, V.; Fortunato, E.; Marques, A.; Águas, H.; Ferreira, I.; Costa, M. E. V.; Martins, R. *Thin Solid Films* **2003,** *427,* 401–405. doi:10.1016/S0040-6090(02)01184-7
11. Sun, C. Q. *Prog. Solid State Chem.* **2007,** *35,* 1–159. doi:10.1016/j.progsolidstchem.2006.03.001
12. Prajapati, C. S.; Sahay, P. P. *Sens. Actuators, B* **2011,** *160,* 1043–1049. doi:10.1016/j.snb.2011.09.023
13. Flickyngerová, S.; Tvarožek, V.; Gašpierik, P. *J. Electr. Eng. (Bratislava, Slovakia)* **2010,** *61,* 291–295.
14. Bechelany, M.; Toury, B.; Brioude, A.; Bernard, S.; Comu, D.; Miele, P. *J. Eur. Ceram. Soc.* **2009,** *29,* 863–867. doi:10.1016/j.jeurceramsoc.2008.07.010
15. Bechelany, M.; Amin, A.; Brioude, A.; Cornu, D.; Miele, P. *J. Nanopart. Res.* **2012,** *14,* 980. doi:10.1007/s11051-012-0980-8
16. Marichy, C.; Bechelany, M.; Pinna, N. *Adv. Mater.* **2012,** *24,* 1017–1032. doi:10.1002/adma.201104129
17. Raghavan, R.; Bechelany, M.; Parlinska, M.; Frey, D.; Mook, W. M.; Beyer, A.; Michler, J.; Utke, I. *Appl. Phys. Lett.* **2012,** *100,* 191912. doi:10.1063/1.4711767
18. Wang, D.; Reynolds, N. *ISRN Condens. Matter Phys.* **2012,** 950354. doi:10.5402/2012/950354
19. Faÿ, S.; Shah, A. Zinc Oxide Grown by CVD Process as Transparent Contact for Thin Film Solar Cell Applications. In *Transparent Conductive Zinc Oxide;* Ellmer, K.; Klein, A.; Rech, B., Eds.; Springer: Berlin Heidelberg, 2008; Vol. 104, pp 235–302. doi:10.1007/978-3-540-73612-7_6
20. Jin, B. J.; Woo, H. S.; Im, S.; Bae, S. H.; Lee, S. Y. *Appl. Surf. Sci.* **2001,** *169–170,* 521–524. doi:10.1016/S0169-4332(00)00751-0
21. Zandi, S.; Kameli, P.; Salamati, H.; Ahmadvand, H.; Hakimi, M. *Phys. B (Amsterdam, Neth.)* **2011,** *406,* 3215–3218. doi:10.1016/j.physb.2011.05.026
22. Armelao, L.; Heigl, F.; Brunet, S.; Sammynaiken, R.; Regier, T.; Blyth, R. I. R.; Zuin, L.; Sankari, R.; Vogt, J.; Sham, T.-K. *ChemPhysChem* **2010,** *11,* 3625–3631. doi:10.1002/cphc.201000730
23. Bethke, S.; Pan, H.; Wessels, B. W. *Appl. Phys. Lett.* **1988,** *52,* 138–140. doi:10.1063/1.99030
24. Vanheusden, K.; Seager, C. H.; Warren, W. L.; Tallant, D. R.; Voigt, J. A. *Appl. Phys. Lett.* **1996,** *68,* 403–405. doi:10.1063/1.116699

25. Egelhaaf, H.-J.; Oelkrug, D. *J. Cryst. Growth* **1996,** *161,* 190–194. doi:10.1016/0022-0248(95)00634-6
26. Hausmann, D. M.; Gordon, R. G. *J. Cryst. Growth* **2003,** *249,* 251–261. doi:10.1016/S0022-0248(02)02133-4
27. Elias, J.; Utke, I.; Yoon, S.; Bechelany, M.; Weidenkaff, A.; Michler, J.; Philippe, L. *Electrochimica Acta* **2013,** in press. doi:10.1016/j.electacta.2013.04.168
28. Kim, Y. W.; Sardari, S. E.; Meyer, M. T.; Iliadis, A. A.; Wu, H. C.; Bentley, W. E.; Ghodssi, R. *Sens. Actuators, B* **2012,** *163,* 136–145. doi:10.1016/j.snb.2012.01.021
29. Abou Chaaya, A.; Le Poitevin, M.; Cabello-Aguilar, S.; Balme, S.; Bechelany, M.; Kraszewski, S.; Picaud, F.; Cambedouzou, J.; Balanzat, E.; Janot, J.-M.; Thami, T.; Miele, P.; Dejardin, P. *J. Phys. Chem. C* **2013,** *117,* 15306–15315. doi:10.1021/jp403330d
30. Cabello-Aguilar, S.; Balme, S.; Chaaya, A. A.; Bechelany, M.; Balanzat, E.; Janot, J.-M.; Pochat-Bohatier, C.; Miele, P.; Dejardin, P. *Nanoscale* **2013,** *5,* 9582–9586. doi:10.1039/C3NR03683A
31. Kim, S. K.; Hwang, C. S.; Park, S.-H. K.; Yun, S. J. *Thin Solid Films* **2005,** *478,* 103–108. doi:10.1016/j.tsf.2004.10.015
32. Huby, N.; Ferrari, S.; Guziewicz, E.; Godlewski, M.; Osinniy, V. *Appl. Phys. Lett.* **2008,** *92,* 023502. doi:10.1063/1.2830940
33. Rivera Márquez, J. A.; Bautista Rodríguez, C. M.; Mendoza Herrera, C.; Rubio Rosas, E.; Zelaya Angel, O.; Tzili Pozos, O. *Int. J. Electrochem. Sci.* **2011,** *6,* 4059–4069.
34. Tapily, K.; Gu, D.; Baumgart, H.; Namkoong, G.; Stegall, D.; Elmustafa, A. A. *Semicond. Sci. Technol.* **2011,** *26,* 115005. doi:10.1088/0268-1242/26/11/115005
35. Yu, C.-F.; Sung, C.-W.; Chen, S.-H.; Sun, S.-J. *Appl. Surf. Sci.* **2009,** *256,* 792–796. doi:10.1016/j.apsusc.2009.08.061
36. Shan, F. K.; Yu, Y. S. *J. Eur. Ceram. Soc.* **2004,** *24,* 1869–1872. doi:10.1016/S0955-2219(03)00490-4
37. Boukhachem, A.; Ouni, B.; Karyaoui, M.; Madani, A.; Chtourou, R.; Amlouk, M. *Mater. Sci. Semicond. Process.* **2012,** *15,* 282–292. doi:10.1016/j.mssp.2012.02.014
38. Bozsóki, I.; Balogh, B.; Gordon, P. *Opt. Laser Technol.* **2011,** *43,* 1212–1218. doi:10.1016/j.optlastec.2011.03.011
39. Shim, E. S.; Kang, H. S.; Kang, J. S.; Kim, J. H.; Lee, S. Y. *Appl. Surf. Sci.* **2002,** *186,* 474–476. doi:10.1016/S0169-4332(01)00746-2
40. Meier, R. J. *Vib. Spectrosc.* **2005,** *39,* 266–269. doi:10.1016/j.vibspec.2005.03.003
41. Cui, L.; Wang, G.-G.; Zhang, H.-Y.; Sun, R.; Kuang, X.-P.; Han, J.-C. *Ceram. Int.* **2013,** *39,* 3261–3268. doi:10.1016/j.ceramint.2012.10.014
42. Giri, P. K.; Bhattacharyya, S.; Chetia, B.; Kumari, S.; Singh, D. K.; Iyer, P. K. *J. Nanosci. Nanotechnol.* **2012,** *12,* 201–206. doi:10.1166/jnn.2012.5113
43. Wang, Q. P.; Zhang, D. H.; Xue, Z. Y.; Hao, X. T. *Appl. Surf. Sci.* **2002,** *201,* 123–128. doi:10.1016/S0169-4332(02)00570-6
44. Djurišić, A. B.; Leung, Y. H. *Small* **2006,** *2,* 944–961. doi:10.1002/smll.200600134
45. Chen, C.-Y.; Chen, M.-W.; Ke, J.-J.; Lin, C.-A.; Retamal, J. R. D.; He, J.-H. *Pure Appl. Chem.* **2010,** *82,* 2055–2073. doi:10.1351/PAC-CON-09-12-05
46. Liu, X.; Wu, X. H.; Cao, H.; Chang, R. P. H. *J. Appl. Phys.* **2004,** *95,* 3141–3147. doi:10.1063/1.1646440
47. Chawla, S.; Jayanthi, K.; Singh, S.; Chander, H. *J. Cryst. Growth* **2008,** *310,* 3517–3521. doi:10.1016/j.jcrysgro.2008.04.050
48. Liao, Z.-M.; Zhang, H.-Z.; Zhou, Y.-B.; Xu, J.; Zhang, J.-M.; Yu, D.-P. *Phys. Lett. A* **2008,** *372,* 4505–4509. doi:10.1016/j.physleta.2008.04.013
49. Wang, J.; Wang, Z.; Huang, B.; Ma, Y.; Liu, Y.; Qin, X.; Zhang, X.; Dai, Y. *ACS Appl. Mater. Interfaces* **2012,** *4,* 4024–4030. doi:10.1021/am300835p
50. Srikant, V.; Clarke, D. R. *J. Appl. Phys.* **1997,** *81,* 6357–6364. doi:10.1063/1.364393
51. Hong, R. J.; Qi, H. J.; Huang, J. B.; He, G. B.; Fan, Z. X.; Shao, J. A. *Thin Solid Films* **2005,** *473,* 58–62. doi:10.1016/j.tsf.2004.06.159
52. Singh, S.; Srinivasa, R. S.; Major, S. S. *Thin Solid Films* **2007,** *515,* 8718–8722. doi:10.1016/j.tsf.2007.03.168
53. Pelant, I.; Valent, J. *Luminescence spectroscopy of semiconductors;* Oxford University Press: Oxford, New York, 2012; pp 162–165. doi:10.1093/acprof:oso/9780199588336.001.0001
54. Comini, E.; Faglia, G.; Sberveglieri, G.; Pan, Z. W.; Wang, Z. L. *Appl. Phys. Lett.* **2002,** *81,* 1869–1871. doi:10.1063/1.1504867
55. Liu, K. W.; Chen, R.; Xing, G. Z.; Wu, T.; Sun, H. D. *Appl. Phys. Lett.* **2010,** *96,* 023111. doi:10.1063/1.3291106
56. Reshchikov, M. A.; Behrends, A.; Bakin, A.; Waag, A. J. *Vac. Sci. Technol., B* **2009,** *27,* 1688–1692. doi:10.1116/1.3130159
57. Bachmann, J.; Zierold, R.; Chong, Y. T.; Hauert, R.; Sturm, C.; Schmidt-Grund, R.; Rheinländer, B.; Grundmann, M.; Gösele, U.; Nielsch, K. *Angew. Chem., Int. Ed.* **2008,** *47,* 6177–6179. doi:10.1002/anie.200800245
58. Viter, R.; Starodub, N.; Smyntyna, V.; Tereschenko, A.; Kusevitch, A.; Sitnik, J.; Buk, J.; Macak, J. *Procedia Eng.* **2011,** *25,* 948–951. doi:10.1016/j.proeng.2011.12.233

License and Terms

Beilstein Journal
of Nanotechnology

Surface passivation and optical characterization of Al_2O_3/a-SiC_x stacks on c-Si substrates

Gema López*, Pablo R. Ortega, Cristóbal Voz, Isidro Martín, Mónica Colina, Anna B. Morales, Albert Orpella and Ramón Alcubilla

Full Research Paper

Open Access

Address:
Electronic Engineering Department, Polytechnic University of Catalonia, Jordi Girona 1-3, Mòdul C4, 08034 Barcelona, Spain

Email:
Gema López* - gema.lopez@upc.edu

* Corresponding author

Keywords:
aluminum oxide (Al_2O_3); antireflection coating; atomic layer deposition; silicon carbide (SiC_x); surface passivation

Beilstein J. Nanotechnol. **2013,** *4,* 726–731.
doi:10.3762/bjnano.4.82

Received: 12 July 2013
Accepted: 17 October 2013
Published: 06 November 2013

This article is part of the Thematic Series "Energy conversion applications of atomic layer deposition".

Guest Editor: J. Bachmann

Abstract

The aim of this work is to study the surface passivation of aluminum oxide/amorphous silicon carbide (Al_2O_3/a-SiC_x) stacks on both p-type and n-type crystalline silicon (c-Si) substrates as well as the optical characterization of these stacks. Al_2O_3 films of different thicknesses were deposited by thermal atomic layer deposition (ALD) at 200 °C and were complemented with a layer of a-SiC_x deposited by plasma-enhanced chemical vapor deposition (PECVD) to form anti-reflection coating (ARC) stacks with a total thickness of 75 nm. A comparative study has been carried out on polished and randomly textured wafers. We have experimentally determined the optimum thickness of the stack for photovoltaic applications by minimizing the reflection losses over a wide wavelength range (300–1200 nm) without compromising the outstanding passivation properties of the Al_2O_3 films. The upper limit of the surface recombination velocity ($S_{\mathrm{eff,max}}$) was evaluated at a carrier injection level corresponding to 1-sun illumination, which led to values below 10 cm/s. Reflectance values below 2% were measured on textured samples over the wavelength range of 450–1000 nm.

Introduction

Surface passivation has become a relevant issue in high efficiency crystalline silicon (c-Si) solar cells. The importance is even increasing as thinner wafers are used to reduce the cost for photovoltaic applications [1]. Aluminum oxide (Al_2O_3) grown by atomic layer deposition (ALD) is a good alternative for passivating both lightly and highly doped n- and also p-type c-Si substrates [2-4]. The excellent passivation quality is due to a double effect: (i) chemical passivation that involves a low density of interface defects, D_{it} ($\approx 10^{11}$ $\mathrm{eV^{-1}cm^{-2}}$), and (ii) field-effect passivation due to a high negative fixed-charge density, Q_{fix} ($\approx 10^{12}$ $\mathrm{cm^{-2}}$) [5-8], which acts as an electrostatic shielding and significantly reduces the density of one type of charge carrier at the interface c-Si/Al_2O_3 [9,10]. In order to achieve the lowest surface recombination velocity (S_{eff}), it is necessary to perfom a thermal treatment after deposition (post-deposition annealing) to activate the passivating properties of Al_2O_3 layers [11,12]. In a previous work [13] we showed that an annealing process for 10 to 20 min at temperatures between 350 °C and 400 °C is enough to obtain an excellent passivation on polished p-type c-Si substrates.

In this work, we complement our preceding work by studying the surface recombination velocity on both n- and p-type wafers (polished and randomly textured), which were passivated with Al_2O_3/a-SiC_x stacks. In previous works we demonstrated that an a-SiC_x capping layer on the Al_2O_3 improves the laser contact formation on p-type c-Si solar cells in comparison to the typical laser fired contact (LFC) process [14,15]. Moreover, it is well known that the ALD deposition of Al_2O_3 has very low deposition rates. Inserting an a-SiC_x capping layer by PECVD technique can overcome this drawback. In this study, we have investigated different combinations of layers that provide good antireflection properties while maintaining a total film thickness of 75 nm. In addition to the passivation, a high-quality antireflection coating (ARC) plays a vital role in highly efficient solar cells [16]. We have measured the reflectance over a wide wavelength range, 300–1200 nm, in order to determine the optimum layer thicknesses for the stack to be used as an ARC without compromising the surface passivation quality.

Results and Discussion

Surface recombination results

The passivation characteristics of the c-Si/Al_2O_3/a-SiC_x stacks were tested the deposition of Al_2O_3 and a-SiC_x, and after a final post-deposition annealing process (Figure 1). Moderate $S_{eff,max}$ values were achieved for as-deposited Al_2O_3 layers with better results on polished than on randomly textured samples. This level of surface passivation can be explained by the relatively low D_{it} ($\approx 10^{11}$ $eV^{-1}cm^{-2}$) prior to the annealing step [17,18], which is responsible for the chemical passivation. The higher

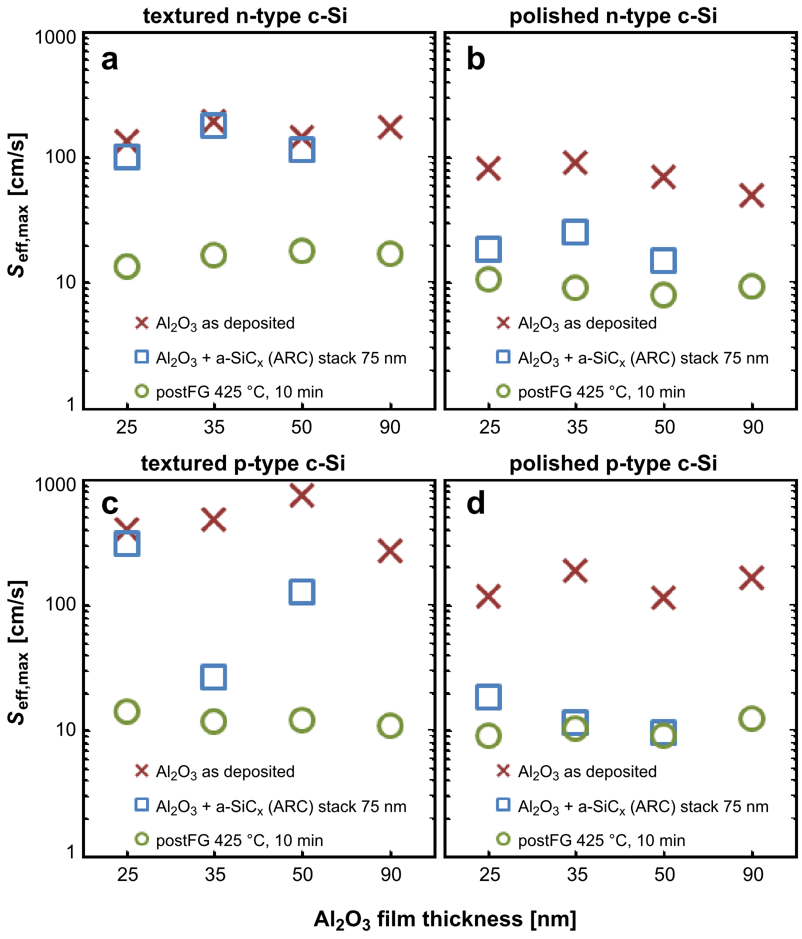

Figure 1: Surface recombination velocity, $S_{eff,max}$ [cm/s]. **(a)** and **(b)** $S_{eff,max}$ for randomly textured and polished n-type wafers respectively. **(c)** and **(d)** $S_{eff,max}$ for randomly textured and polished p-type wafers respectively. $S_{eff,max}$ was determined at 1-sun injection level as a function of the Al_2O_3 thickness. The aluminum oxide layers were complemented up to 75 nm with an a-SiC_x film.

$S_{eff,max}$ results obtained on textured samples (>130 cm/s) could be attributed to a higher surface area due to the pyramid-shaped surface and a higher D_{it} value on the exposed {111} planes [19-21]. Regarding the field-effect passivation, it has been reported that ALD Al_2O_3 films exhibit a low Q_{fix} present at the c-Si/Al_2O_3 interface ($\approx 10^{11}$ cm^{-2}) prior to the annealing step [18]. Under these conditions, the electrostatic shielding of the interface does not induce an increase of the τ_{eff} value and the effect of the chemical passivation becomes more determinant. After the a-SiC_x deposition by PECVD, we observe in general a considerable improvement of the $S_{eff,max}$ parameter. Values close to 10 cm/s were achieved on polished n- and p-type samples. This effect can be attributed to a small in-situ annealing effect that takes place in the PECVD chamber (deposition temperature T_{dep}= 300 °C). The improvement of the passivation quality after an annealing step has been widely reported [3,7,18,22], and it has been related to a lower $D_{it} \leq 1 \times 10^{11}$ eV^{-1}cm^{-2} [17] combined with a higher concentration of fixed negative charges. The presence of these charges provides an electrostatic shielding due to a built-in electric field at the c-Si/Al_2O_3 interface [4,23]. Here, we also see that textured substrates showed higher S_{eff} values after the SiC_x deposition.

The final annealing treatment at T_{ann} = 425 °C for 10 min in forming gas improved the surface passivation, which led to a significant decrease in $S_{eff,max}$ for most of the samples. As a result, outstanding $S_{eff,max}$ values of less than 10 cm/s, i.e., τ_{eff}(1 sun) > 1.3 ms, were achieved independently of doping and surface morphology. We have to note that the final values on randomly textured substrates were quite similar to those of polished ones. Thus, the annealing temperature is a crucial parameter to activate the surface passivation and it should be higher for textured samples (T_{ann} = 425 °C) than that found for polished substrates in a previous work (T_{ann} = 375 °C) [13]. In fact, some polished samples already showed an optimum passivation quality just after the PECVD process. On the other hand, an annealing temperature of 425 °C is a critical limit to avoid a blistering effect, which we have observed on polished samples with a 90 nm thick Al_2O_3 layer. The blistering effect consists in a partial delamination of the Al_2O_3 film and the corresponding bubble formation. It is caused by a gaseous desorption where the layer acts as a gas barrier. The density and dimensions of the bubbles are directly related to the annealing and the ALD process temperatures and the thickness of the Al_2O_3 layer [13,24,25].

Regarding the effect of the film thickness, it is interesting to note that a rather constant high level of surface passivation is obtained after the annealing for the whole range of Al_2O_3 thicknesses. The field-effect passivation remains constant independently of the thickness of the alumina layer probably because fixed negative charges seem to be located at the interface between Al_2O_3 and c-Si [6]. Other authors have demonstrated that a thin interfacial SiO_x layer between the c-Si and the Al_2O_3 film and generated during the Al_2O_3 deposition process, plays an important role in the formation of the negative fixed-charge density [26-30].

Optical properties of Al_2O_3 and the Al_2O_3/a-SiC_x stack

The refractive index of Al_2O_3 measured by ellipsometry was around 1.6 at a wavelength of 632 nm, whereas for the a-SiC_x layers it was quite close to 2.0. On the other hand, the absorbance of Al_2O_3/a-SiC_x stacks deposited on borosilicate glass was analyzed by means of an UV–vis–NIR Spectrometer equipped with an integrating sphere in the wavelength range from 300 to 600 nm. The stack absorbance was calculated from the reflectance and transmittance measurements following Equation 1 and Equation 2,

$$A_L\left(\%\right) = 100 - T_{L+G} - R_{L+G} - A_G \tag{1}$$

$$A_G\left(\%\right) = 100 - T_G - R_G\ , \tag{2}$$

where A is the absorbance, T the transmittance and R the reflectance. The subscritps L and G correspond to the layer stack and glass respectively. The results of the absorbance measurements are shown in Figure 2.

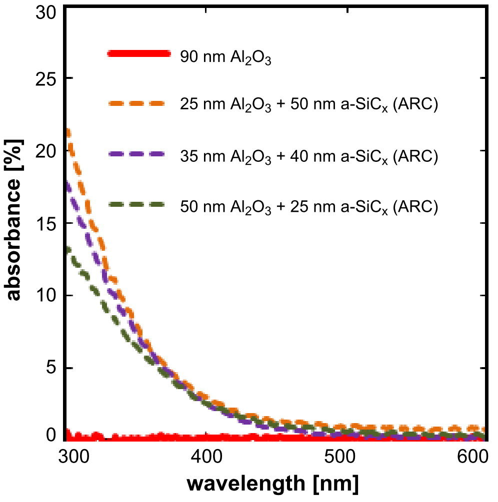

Figure 2: Absorbance as a function of the wavelength in the range from 300 to 600 nm. Dashed lines belong to stacks with different Al_2O_3 thicknesses while the continuous red line is the absorbance of 90 nm Al_2O_3.

Other works have previously reported an optical bandgap of E_{opt} = 6.4 ± 0.1 eV for as-deposited and annealed ALD Al_2O_3 films [18]. This means that this material is transparent for wavelengths above 200 nm. Therefore, absorption of light by the Al_2O_3 layer does not occur in the wavelength range relevant for photovoltaic applications. For the sake of clarity, only the 300 to 600 nm wavelength range is depicted, i.e, in which a relevant absorbance can exist. However, it can be seen that as the a-SiC_x layer thickness increases, the optical absorbance also increases up to a value of 21.1% at 300 nm. Thus, the SiC_x capping layer is less attractive to be used as an antireflection layer on the illuminated side of the solar cell compared to a single 90 nm Al_2O_3 film.

Reflectance measurements were also carried out. No significant differences were found between n and p-type c-Si substrates. These measurements of single Al_2O_3 films as well as Al_2O_3/SiC_x stacks are shown in Figure 3.

The textured sample without ARC coating (black lines in Figure 3, left) exhibits an integrated average reflectance of 13.3%, much lower than that of polished c-Si substrates. For a randomly textured surface, the reduced reflectance is explained by a second reflection of the incident light at the sidewalls of an opposite pyramid [31]. After coating the silicon substrates, the optical reflectance was further reduced.

When a 90 nm Al_2O_3 film is deposited on a polished surface, the reflectance yields a minimum of 3.2% at a wavelength of about 600 nm, but it increases quickly for shorter and longer wavelengths. Moreover, the reflectance properties become worse as the Al_2O_3 film thickness decreases. Next, the reflectance is strongly reduced when the polished samples are coated, but it still increases for longer wavelengths.

On the other hand, when a textured c-Si sample is coated by 90 nm of Al_2O_3 the reflectance values measured are below 2%

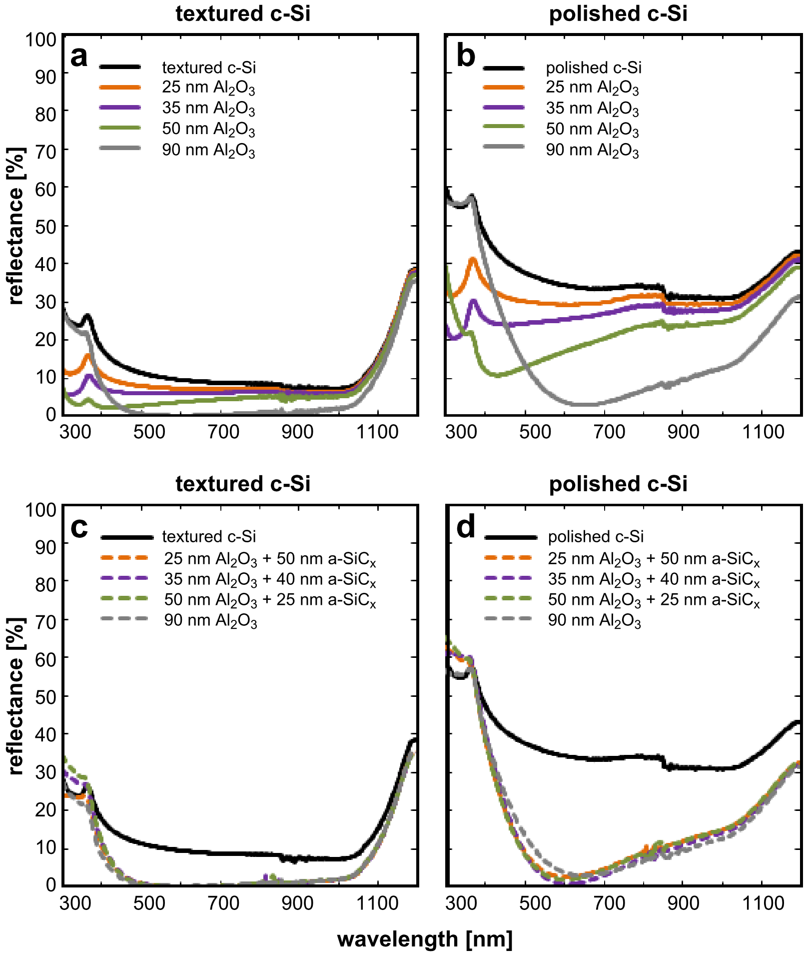

Figure 3: Reflectance curves of Al_2O_3-coated randomly textured c-Si **(a)** and polished c-Si **(b)** for different film thicknesses. Reflectance curves of Al_2O_3/a-SiC_x coated randomly textured c-Si **(c)** and polished c-Si **(d)**. As a reference, bare polished and textured c-Si reflectances are also included (black line).

between 460 and 1000 nm. Similar results were obtained with the textured samples coated by 75 nm Al_2O_3/a-SiC_x stacks. Thus, both 90 nm Al_2O_3 film and 75 nm Al_2O_3/a-SiC_x stacks on textured surfaces are excellent anti-reflection options.

Conclusion

Al_2O_3 layers and Al_2O_3/a-SiC_x stacks with different thicknesses were deposited on polished and randomly textured p- and n-type c-Si substrates by combining thermal ALD and PECVD technique. Outstanding $S_{\text{eff,max}}$ values below about 15 cm/s were achieved independently of the surface morphology and doping type of the samples. This value is low enough to obtain highly efficient c-Si solar cells. Concerning the optical properties, the absorbance of Al_2O_3 layers with different thicknesses and also of different Al_2O_3/a-SiC_x stacks was calculated by evaluating reflectance and transmittance measurements. We found that the absorption loss in a-SiC_x layers in the range of short wavelengths of is the reason for the superior overall optical performance of a single 90 nm thick Al_2O_3 film. Therefore, the latter represents the better option as an antireflection coating compared to Al_2O_3/a-SiC_x stacks. This result is supported by the reflectance measurements of Al_2O_3 films with different thicknesses and Al_2O_3/a-SiC_x stacks on polished and textured c-Si substrates in the wavelength range from 300 to 1200 nm. In any case, the measured reflectance was less than 2% for all the Al_2O_3/a-SiC_x stacks and also for the single 90 nm layer of Al_2O_3. Nevertheless, an a-SiC_x capping layer could be useful if the Al_2O_3 layer needs to be protected from some chemical treatment during the solar cell fabrication. Moreover, on the rear side of a c-Si solar cell, where the optical absorbance is not critical, an a-SiC_x layer on top of the passivated Al_2O_3 film acts as a back reflector that reflects photons towards the bulk. This a-SiC_x capping layer on the Al_2O_3 also improves the laser contact formation on p-type c-Si solar cells.

In summary, we can conclude that a 90 nm Al_2O_3 film on textured c-Si substrates results in a good scheme for both passivation and anti-reflection coating on the illuminated side of highly efficient solar cells, whereas an a-SiC_x capping layer on Al_2O_3 films on the rear side of the solar cell provides better back contacts and a better back reflector scheme.

Experimental

As starting material, n- and p-type (2.5 ± 0.3 Ωcm) FZ silicon(100) wafers with a thickness of approximately 290 µm were used. One p-type and one n-type wafer were textured on both sides with solution of tetramethylammonium hydroxide (TMAH) in isopropanol (IPA) solution. Before film deposition, four wafers, two n-type (one textured and one polished) and two p-type (one textured and one polished) were cleaned following an RCA sequence and cut to quarters. Al_2O_3 films were subsequently deposited by thermal ALD (Savannah S200, Cambridge Nanotech; Cambridge, MA, USA) at T_{dep} = 200 °C. This technique is based on sequential, self-limiting chemical reactions at the surface. The surface of the substrate is exposed to the precursor gases in alternating manner. The reactions are cyclical and after each reaction, there is a purge with N_2. The typical ALD cycle to deposit Al_2O_3 layers consists of the injection into the chamber of trimethylaluminum ($Al(CH_3)_3$) for 15 ms followed by N_2 purging and the injection of water vapour for 50 ms followed by N_2 purging. The precursor doses and exposure times were chosen such that all films were deposited under saturated self-limiting conditions leading to a film growth of 1.1 Å/cycle. On each sample, belonging to a different type of wafer, films with a thickness of 25, 35, 50 and 90 nm, respectively, were deposited (deposition times of 38, 53, 73 and 137 min respectively). On top of these films, we deposited an amorphous silicon carbide (a-SiC_x) film by PECVD that uses silane (SiH_4) and methane (CH_4) as precursor gases. The thicknesses of these a-SiC_x films were 50, 40 and 25 nm, respectively (deposition times of 12 min 50 sec, 10 min 15 sec and 6 min 24 sec, respectively) in order to complement the 25, 35 and 50 nm Al_2O_3 films for a total stack thickness of 75 nm. Substrates with an Al_2O_3 thickness of 90 nm were also studied without any a-SiC_x capping layer. A post-deposition annealing process in a forming gas environment (H_2/N_2) at 425 °C for 10 min was done to activate the passivation properties. All these substrates were symmetrically covered to measure the effective lifetime τ_{eff} by measuring the quasi-steady-state photoconductance (QSSPC) with a Wafer Lifetime Tester Sinton WCT-100 [32,33]. The upper limit of the surface recombination velocity ($S_{\text{eff,max}}$) was deduced from the effective lifetime τ_{eff} measurements as a function of the excess carrier density (Δn) at 1 sun injection level as

$$S_{\text{eff,max}} = \frac{W}{2\tau_{\text{eff}}} \tag{3}$$

where W is the substrate thickness and an infinite bulk lifetime has been assumed.

Concerning the optical characterization, the thickness and refractive index of the individual Al_2O_3 and SiC_x layers were measured by ellipsometry (Plasmos SD 2100) at a wavelength of 632 nm. Finally, in order to know the optical absorbance, we also deposited the same Al_2O_3/a-SiC_x stacks on transparent substrates (Borosilicate glass). The reflectance (diffuse and specular) and the transmittance were measured in the wavelength range from 300 to 1200 nm by using a UV–visible–NIR spectrometer (Shimadzu 3600) equipped with an ISR 3100 integrating sphere.

Acknowledgements

This work has been supported by the Spanish Ministry of Science and Innovation under projects ENE2010-21384-C04-04, TEC2011-26329 and INNDISOL IPT-420000-2010-6 (FEDER funded “Una manera de hacer Europa”).

References

1. Hofmann, M.; Janz, S.; Schmidt, C.; Kambor, S.; Suwito, D.; Kohn, N.; Rentsch, J.; Preu, R.; Glunz, S. W. *Sol. Energy Mater. Sol. Cells* **2009,** *93,* 1074–1078. doi:10.1016/j.solmat.2008.11.056
2. Hoex, B.; Van de Sanden, M. C. M.; Schmidt, J.; Brendel, R.; Kessel, W. M. M. *Phys. Status Solidi RRL* **2012,** *6,* 4–6. doi:10.1002/pssr.201105445
3. Agostinelli, G.; Delabie, A.; Vitanov, P.; Alexieva, Z.; Dekkers, H. F. W.; De Wolfa, S.; Beaucarne, G. *Sol. Energy Mater. Sol. Cells* **2006,** *90,* 3438–3442. doi:10.1016/j.solmat.2006.04.014
4. Hoex, B.; Schmidt, J.; Bock, R.; Altermatt, P. P.; van de Sanden, M. C. M.; Kessels, W. M. M. *Appl. Phys. Lett.* **2007,** *91,* 112107. doi:10.1063/1.2784168
5. Werner, F.; Veith, B.; Tiba, V.; Poodt, P.; Roozeboom, F.; Brendel, R.; Schmidt, J. *Appl. Phys. Lett.* **2010,** *97,* 162103. doi:10.1063/1.3505311
6. Dingemans, G.; Seguin, R.; Engelhart, P.; van de Sanden, M. C. M.; Kessels, W. M. M. *Phys. Status Solidi RRL* **2010,** *4,* 10–12. doi:10.1002/pssr.200903334
7. Seguini, G.; Cianci, E.; Wiemer, C.; Saynova, D.; van Rossmalen, J. A. M. *Appl. Phys. Lett.* **2013,** *102,* 131603. doi:10.1063/1.4800541
8. Liao, B.; Stangl, R.; Mueller, T.; Lin, F.; Bhatia, C. S.; Hoex, B. *J. Appl. Phys.* **2013,** *113,* 024509. doi:10.1063/1.4775595
9. Hoex, B.; Schmidt, J.; Pohl, P.; van de Sanden, M. C. M.; Kessels, W. M. M. *J. Appl. Phys.* **2008,** *104,* 044903. doi:10.1063/1.2963707
10. Terlinden, N. M.; Dingemans, G.; van de Sanden, M. C. M.; Kessels, W. M. M. *Appl. Phys. Lett.* **2010,** *96,* 112101. doi:10.1063/1.3334729
11. Rafí, J. M.; Zabala, M.; Bedarrain, O.; Campabadal, F. *J. Electrochem. Soc.* **2011,** *158,* G108–G114. doi:10.1149/1.3559458
12. Frascaroli, J.; Seguini, G.; Cianci, E.; Saynova, D.; van Roosmalen, J.; Perego, M. *Phys. Status Solidi A* **2013,** *210,* 732–736. doi:10.1002/pssa.201200568
13. Lopez, G.; Ortega, P.; Voz, C.; Martín, I.; Colina, M.; Orpella, A.; Alcubilla, R. Optimization of Al_2O_3 films obtained by ALD to passivate p-type c-Si wafers. In *Proccedings of the 27th European Photovoltaic Solar Energy Conference and Exhibition,* Frankfurt, Sept 24–28, 2012; Germany, 2012.
14. Ortega, P.; Martín, I.; López, G.; Colina, M.; Orpella, A.; Voz, C.; Alcubilla, R. *Sol. Energy Mater. Sol. Cells* **2012,** *106,* 80–83. doi:10.1016/j.solmat.2012.05.012
15. Martín, I.; Ortega, P.; Colina, M.; Orpella, A.; López, G.; Alcubilla, R. *Prog. Photovoltaics* **2012,** *21,* 1171–1175. doi:10.1002/pip.2207
16. Green, M. A. *Higher Efficiency Silicon Solar cells;* Trans. Tech. Pub.: Aedermannsdorf, Switzerland, 1987.
17. Dingemans, G.; Terlinden, N. M.; Pierreux, D.; Profijt, H. B.; van de Sanden, M. C. M.; Kessels, W. M. M. *Electrochem. Solid-State Lett.* **2011,** *14,* H1–H4. doi:10.1149/1.3501970
18. Dingemans, G.; Kessels, W. M. M. *J. Vac. Sci. Technol., A* **2012,** *30,* 040802. doi:10.1116/1.4728205
19. McIntosh, K. R.; Johnson, L. P. *J. Appl. Phys.* **2009,** *105,* 124520. doi:10.1063/1.3153979
20. Angermann, H. *Appl. Surf. Sci.* **2008,** *254,* 8067–8074. doi:10.1016/j.apsusc.2008.03.022
21. Basore, P. A. *IEEE Trans. Electron Devices* **1990,** *37,* 337–343. doi:10.1109/16.46362
22. Benick, J.; Richter, A.; Hermle, M.; Glunz, S. W. *Phys. Status Solidi RRL* **2009,** *3,* 233–235. doi:10.1002/pssr.200903209
23. Hoex, B.; Schmidt, J.; Van de Sanden, M. C. M.; Kessels, W. M. M. Crystalline silicon surface passivation by negative-charge-dielectric Al_2O_3. Photov.Spec.Conf. PVSC 08, 33th IEEE, May 11–16, 2008; pp 1–4.
24. Vermang, B.; Goverde, H.; Lorenz, A.; Vereecke, G.; Meersschaut, J.; Cornglliotti, E.; Rothschild, A.; John, J.; Poortmans, J.; Mertens, R. On the blistering of atomic layer deposited Al_2O_3 as Si surface passivation. Photov. Spec. Conf. PVSC11, 37th IEEE, June 19–24, 2011; pp 3562–3567.
25. Beldarrain, O.; Duch, M.; Zabala, M.; Rafí, J. M.; Bargalló González, M.; Campabadal, F. *J. Vac. Sci. Technol., A* **2012,** *31,* 01A128. doi:10.1116/1.4768170
26. Gielis, J. J. H.; Van de Sanden, M. C. M.; Kessels, W. M. M. *J. Appl. Phys.* **2008,** *104,* 073701. doi:10.1063/1.3658246
27. Dingemans, G.; Terlinden, N. M.; Verheijen, M. A.; van de Sanden, M. C. M.; Kessels, W. M. M. *J. Appl. Phys.* **2011,** *110,* 093715. doi:10.1063/1.3658246
28. Hoex, B.; Heil, S. B. S.; Langereis, E.; van de Sanden, M. C. M.; Kessels, W. M. M. *Appl. Phys. Lett.* **2006,** *89,* 042112. doi:10.1063/1.2240736
29. Hoex, B.; Gielis, J. J. H.; van de Sanden, M. C. M.; Kessels, W. M. M. *J. Appl. Phys.* **2008,** *104,* 113703. doi:10.1063/1.3021091
30. Lei, D.; Yu, X.; Song, L.; Gu, X.; Li, G.; Yang, D. *Appl. Phys. Lett.* **2011,** *99,* 052103. doi:10.1063/1.3616145
31. Zhao, J.; Green, M. *IEEE Trans. Electron Devices* **1991,** *38,* 1925–1934. doi:10.1109/16.119035
32. Sinton, R. A.; Cuevas, A. *Appl. Phys. Lett.* **1996,** *69,* 2510. doi:10.1063/1.117723
33. Cuevas, A.; Macdonald, D. *Sol. Energy* **2004,** *76,* 255–262. doi:10.1016/j.solener.2003.07.033

License and Terms

Beilstein Journal
of Nanotechnology

Ellipsometry and XPS comparative studies of thermal and plasma enhanced atomic layer deposited Al_2O_3-films

Jörg Haeberle[1], Karsten Henkel[*1], Hassan Gargouri[2], Franziska Naumann[2],
Bernd Gruska[2], Michael Arens[2], Massimo Tallarida[1] and Dieter Schmeißer[1]

Full Research Paper

Open Access

Address:
[1]Brandenburg Technical University, Applied Physics and Sensors,
K.-Wachsmann-Allee 17, 03046 Cottbus, Germany and [2]Sentech
Instruments GmbH, Schwarzschildstraße 2, 12489 Berlin, Germany

Email:
Karsten Henkel[*] - henkel@tu-cottbus.de

* Corresponding author

Keywords:
Al_2O_3; ALD; ellipsometry; PE-ALD; XPS

Beilstein J. Nanotechnol. **2013,** *4,* 732–742.
doi:10.3762/bjnano.4.83

Received: 30 June 2013
Accepted: 23 October 2013
Published: 08 November 2013

This article is part of the Thematic Series "Energy conversion applications of atomic layer deposition".

Guest Editor: J. Bachmann

Abstract

We report on results on the preparation of thin (<100 nm) aluminum oxide (Al_2O_3) films on silicon substrates using thermal atomic layer deposition (T-ALD) and plasma enhanced atomic layer deposition (PE-ALD) in the SENTECH SI ALD LL system. The T-ALD Al_2O_3 layers were deposited at 200 °C, for the PE-ALD films we varied the substrate temperature range between room temperature (rt) and 200 °C. We show data from spectroscopic ellipsometry (thickness, refractive index, growth rate) over 4” wafers and correlate them to X-ray photoelectron spectroscopy (XPS) results. The 200 °C T-ALD and PE-ALD processes yield films with similar refractive indices and with oxygen to aluminum elemental ratios very close to the stoichiometric value of 1.5. However, in both also fragments of the precursor are integrated into the film. The PE-ALD films show an increased growth rate and lower carbon contaminations. Reducing the deposition temperature down to rt leads to a higher content of carbon and CH-species. We also find a decrease of the refractive index and of the oxygen to aluminum elemental ratio as well as an increase of the growth rate whereas the homogeneity of the film growth is not influenced significantly. Initial state energy shifts in all PE-ALD samples are observed which we attribute to a net negative charge within the films.

Introduction

Thin aluminum oxide (Al_2O_3) layers deposited by atomic layer deposition (ALD) have been investigated for several applications like surface passivation or encapsulation in organic and inorganic photovoltaic devices [1,2], interfacial buffering for high-k dielectrics [3,4], organic memories [5], and nano-laminates [6] as well as work function modification [7], gas diffusion barrier [8] or corrosion protection [9]. Recently, there is a growing activity in covering photo-electrodes or electrodes by ultra-thin Al_2O_3 ALD layers for electrochemical energy generation and storage systems [10] in order to enhance the efficiency and durability of such devices. This includes for example solar energy conversion systems like dye sensitized solar cells [11,12] and water splitting devices [13] or lithium ion batteries [14]. Here, in particular the excellent conformability of ALD growth over high surface area materials and its uniformity and self-termination [15] were beneficially applied. Furthermore, Al_2O_3 ALD layers have shown their ability as gate dielectrics for future graphene based electronics [16].

The most commonly used ALD sequence for thermal ALD (T-ALD) is the pulsed alternation of trimethyl-aluminum (TMA) as metal source and water as oxygen source, respectively [1,15,17]. Within the last decade the research have been extended to plasma enhanced ALD (PE-ALD) in which the H_2O as oxygen source is replaced by a plasma exposure (O_2, O_3) [1,17,18]. Caused by the higher reactivity of the plasma generated oxygen radicals the PE-ALD extends the capabilities of ALD such as improved film quality, increased flexibility in process conditions [17,18], and is in particular preferred over thermal ALD for lower substrate temperatures due to lower impurity levels [1,18]. The latter allows further the ALD use in organic and in particular flexible electronic applications or on thermally fragile substrates [2,8,15,18].

Recently the Kessels group has reviewed the state of the art of plasma-assisted ALD [18] and surface passivation schemes of Al_2O_3 prepared by ALD [1]. This group has reported also on the modeling of reaction regimes influencing the conformality of the PE-ALD process [19]. Herein the typical parameters like growth rate per cycle (GPC), density and refractive index were determined by ellipsometry whereas the elemental composition was mostly deduced from Rutherford Backscattering Spectrometry (RBS). The influence of the substrate temperature onto these parameters was discussed, also when a commercial 200 mm ALD reactor was used [20]. However characterizations based X-ray photoelectron spectroscopy (XPS) in dependence of the substrate temperature are not shown in that reviews. Furthermore to our knowledge there seems to be a lack in reports about dielectric parameters in dependence of the substrate temperature for PE-ALD as mostly comparisons are given at fixed temperatures [1,21] or only for T-ALD samples [22].

In this paper we show a comparison of Al_2O_3 samples prepared by T-ALD and PE-ALD respectively based on ellipsometry and on X-ray photoelectron spectroscopy measurements (XPS). The substrate temperature in the PE-ALD process was varied from 200 °C downwards to room temperature (rt). The Sentech ALD reactor system is applicable for both processes (see Experimental section). In that way we are able to investigate samples which are produced in the same chamber avoiding the influence which might be caused by variations of different ALD systems. In the first part we evaluate the newly developed SENTECH's SI ALD LL system by comparison of homogeneity, GPC, and refractive index with recently reported values in the literature whereas in the second part the oxygen to aluminum (O/Al) ratio and carbon contaminations are discussed. Dielectric parameters of these films will be discussed elsewhere [23].

Results and Discussion

Thickness and homogeneity (ellipsometry)

First, we report on the thickness homogeneity of the T-ALD and PE-ALD layers. Film thickness and refractive index of the deposited layers were determined using a SENTECH SE 800 spectroscopic ellipsometry instrument (for details see experimental section). Figure 1 depicts the thickness distributions of the PE-ALD layers prepared at 200 °C, 80 °C and rt; for comparison a film produced at typical T-ALD conditions at 200 °C is shown.

Figure 2a summarizes these homogeneity results in dependence of the substrate temperature. Both, the T-ALD and PE-ALD layers prepared at 200 °C show very good homogeneities with non-uniformities of only ±0.5% and ±0.8%, respectively. For the PE-ALD layers produced at 80 °C (±1.1%) and rt (±1.2%) the values are only slightly increased. For thinner PE-ALD layers (≈10 nm, also shown in Figure 2a) the homogeneity remains approximately the same for $T > 100$ °C. Below this temperature the inhomogeneity increases to ±2.5% and ±3.8% at 80 °C and rt, respectively. Assuming the same roughness in the thicker and thinner layers at the same process temperature, the influence of the roughness on the thickness distribution is increased for the thinner layer. Therefore we argue that at lower temperatures the roughness is increased compared to the layers at $T > 100$°C.

Parasitic chemical vapour deposition (CVD) like reactions due to remaining TMA precursor within the reactor caused by not optimal purge times as well as a radial non-uniformity of the plasma species are believed to be responsible for the thickness non-uniformity in the PE-ALD process [1].

Growth rate and refractive index (ellipsometry)

The growth rate per cycle and the refractive index at 632.8 nm wavelength are deduced from the ellipsometry data and plotted versus growth temperatures in Figure 2b and 2c. For the PE-ALD process the growth rate of the Al_2O_3 film increases from 1.2 Å/cycle to 2 Å/cycle, whereas the refractive index decreases from 1.64 to 1.56 when the substrate temperature is

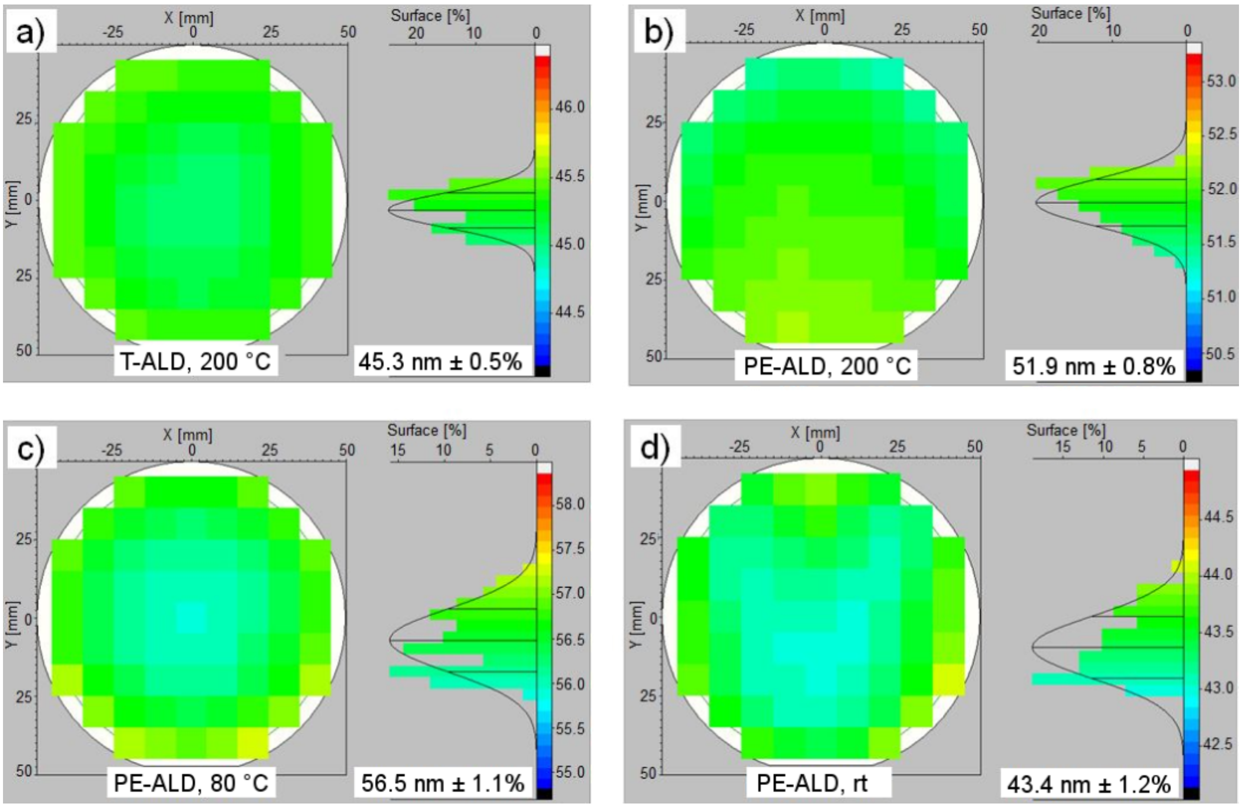

Figure 1: Thickness distributions of T-ALD at 200 °C (a) and PE-ALD films at 200 °C (b), 80 °C (c) and rt (d). The data were recorded by ellipsometry. The left part of every fraction shows the thickness distribution over 4 inch wafers (Ø = 100 mm) and the right part its statistics. The thickness average and the uniformity of the layer over the 4 inch wafer are given within the graphs.

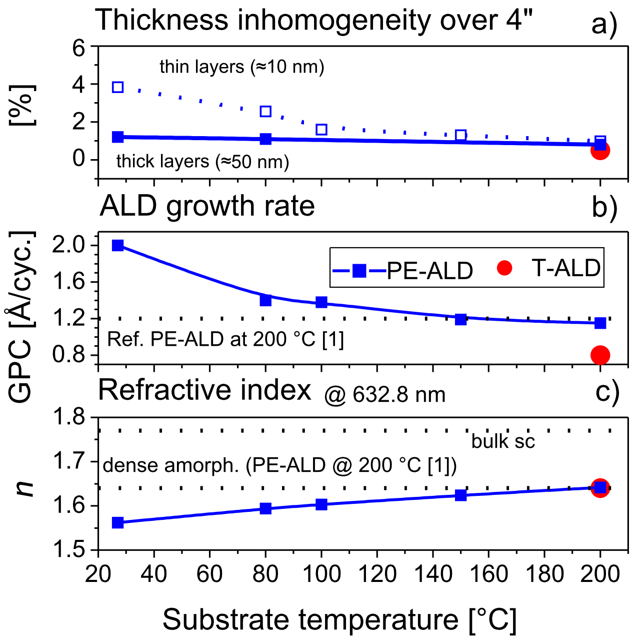

Figure 2: Ellipsometry results showing thickness homogeneity (a), growth rate (b) and refractive index at 632.8 nm (c) in dependence of the substrate temperature of PE-ALD layers (blue squares, filled: ≈50 nm thick films, open: ≈10 nm thick films). The data of the T-ALD film at 200 °C are included (red filled circle). For orientation the reference values of the growth rate and refractive index reported for dense amorphous layers (PE-ALD, 200 °C) in literature [1] and the bulk single crystalline (sc) value of the refractive index are illustrated by dashed lines.

reduced from 200 °C down to rt. The data of the PE-ALD at 200 °C and also the temperature dependency of the growth rate are in very good agreement with values reported by the Kessels group [1]. Also the trend of the refractive index is very similar to reported values by the George group [8,15] for the thermal ALD in the temperature range between 33 °C and 177 °C. For comparison, our thermal ALD procedure for Al_2O_3 (200 °C) delivers a growth rate of 0.8 Å/cycle and a refractive index of 1.64, these value are also included in Figure 2.

The observed reduction of the refractive index at lower temperatures corresponds to a slightly reduced mass density [8,15,18]. This might be also partly responsible for the increased GPC values. However, the main driving force for the higher GPC at lower temperatures is attributed to an increased incorporation of aluminum atoms into the layers due to a higher surface density of hydroxyl groups as the dominant adsorption sites for TMA [18]. At higher temperatures thermally activated dehydroxylation reactions occur and the GPC decreases [1]. In addition the CVD parasitic reactions mentioned above may lead to the dissociation of the TMA precursor resulting in higher GPC values [1].

Oxygen to aluminum elemental ratios (XPS)

The chemical composition of the Al_2O_3 films prepared at different temperatures was investigated by XPS. Based on the general trends reported above, here the PE-ALD layers at 200 °C, 80 °C and rt as well as the T-ALD sample (200 °C) were measured. The XPS survey spectra (Figure 3) of PE-ALD samples (200 °C, 80 °C, rt) and of the T-ALD (200 °C) sample depict mainly Al and O contributions but also carbon contamination. The latter will be discussed below.

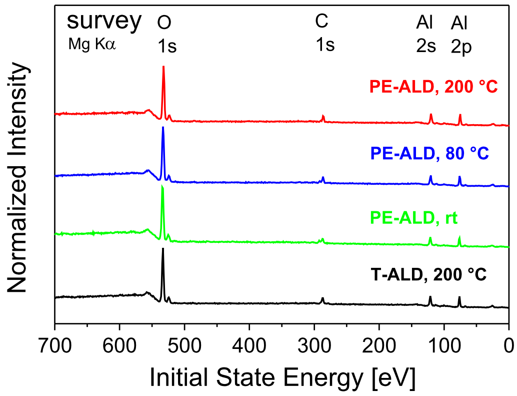

Figure 3: XPS survey spectra (Mg Kα) of the PE-ALD layers deposited at 200 °C (red curve), 80 °C (blue) and rt (green) and the T-ALD at 200 °C (black). The main core levels are labeled. For better comparison the data are normalized to each O1s peak maximum and separated vertically, but shown in the same scaling.

Now we focus on the details of the XPS analysis, in particular on the values of the observed peak positions, the carbon content, the contributions in the peak profiles of the Al2p and O1s core levels. We also discuss the origin of the observed peak shifts.

Peak positions

In Figure 4a and 4b we show the detailed spectra of the O1s and Al2p core levels. First we notice that all observed peak positions appear at very high initial state (IS) energy values. Second, the observed values depend significantly on the preparation conditions and vary within 1 to 1.5 eV. The peak maxima of the O1s and Al2p core levels of the T-ALD sample appear at 533.2 eV and 76.3 eV IS energy. It is obvious that the positions of the peak maxima are shifted towards lower IS energy in both, the O1s and the Al2p data for the PE-ALD samples, except for the O1s of the rt sample discussed below. The observed energy values for the individual core levels and the corresponding FWHM are listed also in Table 1 for the individual samples.

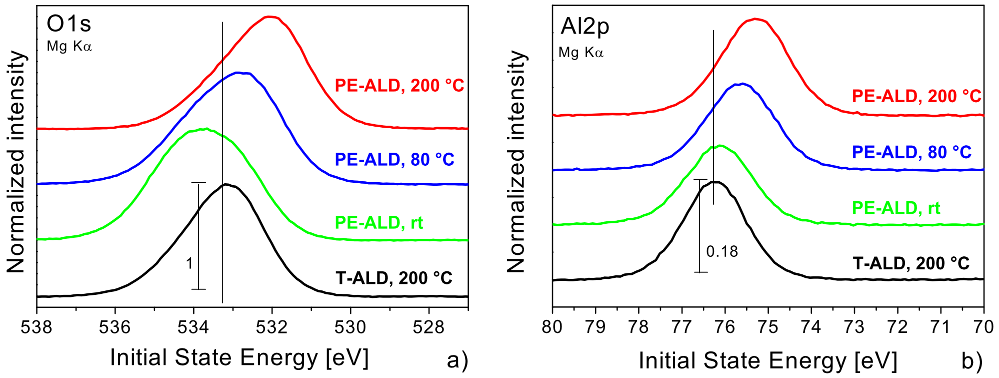

Figure 4: O1s (a) and Al2p (b) core level spectra (Mg Kα) of the PE-ALD layers deposited at 200 °C (red curve), 80 °C (blue) and rt (green) and the T-ALD at 200 °C (black). The data are normalized to each O1s peak maximum and separated vertically, but shown in the same scaling. The IS energy is referred to the Fermi energy.

Table 1: Summary of the data determined in this contribution for PE-ALD layers at (200 °C, 80 °C, rt) and the T-ALD film at 200 °C. The XPS data shown here are based on Mg Kα excitation.

ALD – Process		T	PE	PE	PE
Temperature [°C]		200	27 (rt)	80	200
Thickness Inhomogeneity [%]	≈50 nm	0.5	1.2	1.1	0.8
	≈10 nm	n.d.	3.8	2.5	0.98
Growth rate [Å/cycle]		0.8	2.0	1.4	1.2
Refractive index		1.64	1.56	1.59	1.64
O/Al ratio (XPS)		1.46	1.20	1.32	1.47
C/Al (EDX)		n.d.	0.22	0.16	0.07
C (XPS) [%]		11	14	14	8
Al2p peak position/FWHM [eV]		76.3/1.7	76.1/1.8	75.6/1.9	75.3/1.9
O1s peak position/FWHM [eV]		533.2/2.4	533.7/3.0	532.8/2.9	532.1/2.6
C1s peak position/FWHM [eV]		286.9/1.8	287.1/1.9	286.5/1.9	286.2/2.0

Carbon contributions

It should be noted that the generally used approach to refer the IS energy to the position of the C1s contribution cannot be applied here. One reason is that the carbon species are not associated with adsorbed methyl groups (284.5 eV) or adsorbed hydro-carbons (285 eV) but are inserted in an oxidic matrix. The formation of C–O bonds results in core level energies at around 286 eV (Figure 5). Second, the peak position of the C1s (Figure 5) varies in the same way as that of the Al2p and the O1s core levels. This indicates that all peak positions are shifted due to the individual preparation conditions.

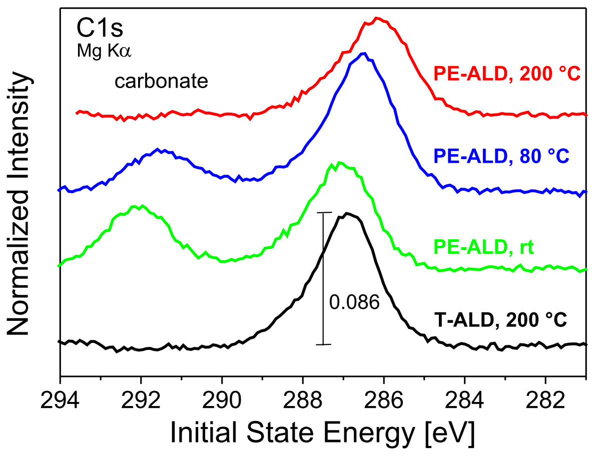

Figure 5: C1s core level spectra (Mg Kα) of the PE-ALD layers deposited at 200 °C (red curve), 80 °C (blue) and rt (green) and the T-ALD at 200 °C (black). The data are normalized to each O1s peak maximum and separated vertically, but shown in the same scaling. The energy is referred to the Fermi energy.

In case that the peak positions would be referred to C1s positions at a fixed energy (e.g., 285 eV) we would still observe a shift in the IS energies of both the O1s and Al2p core levels. This is exemplarily illustrated in Figure 6 for the Al2p. All PE-ALD samples exhibit a similar remaining shift of about 400 meV. This we attribute to fixed oxide charges (see below).

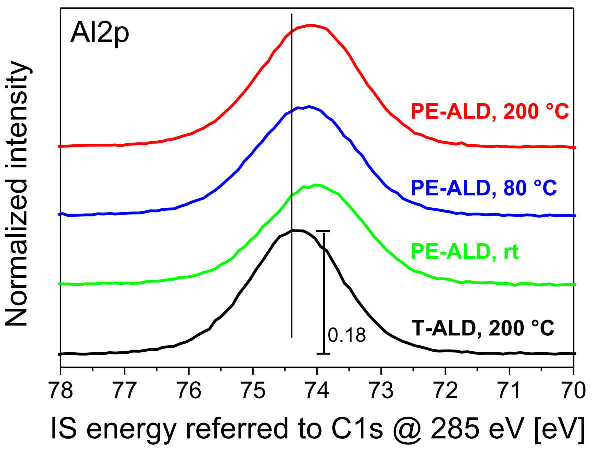

Figure 6: Al2p core level spectra (Mg Kα) of the PE-ALD layers deposited at 200 °C (red curve), 80 °C (blue) and rt (green) and the T-ALD at 200 °C (black) when referred to a fixed C1s peak position of 285 eV for every sample. The data are normalized to each O1s peak maximum and separated vertically, but shown in the same scaling.

Also, due to the fact that we observe significant C1s intensities – we have to consider the contributions from carbonate species [24]. These are incorporated by the precursor side groups which do not desorb completely during the purging periods. The combustion like character of the PE-ALD process yields also COO side products [1,18].

Peak profiles

The profiles and FWHM of the core levels can be analyzed to give information about the chemical neighborhood of the individual elements. The data in Figure 4 indicate that both, the

Al2p and the O1s levels are rather broad and have some asymmetric profile. Only for the T-ALD sample the shape of the Al2p is rather symmetric and can be decomposed by one single peak which we assign to Al–O [1,24,25]. In contrast, the O1s signal exhibits a shoulder towards higher IS energies. For the PE-ALD samples the line width is broader, in general, and the asymmetries are more pronounced.

We attribute the broadening to the existence of hydroxyl (OH) groups [24] which are incorporated within the films by the usage of the H_2O oxidant in T-ALD or the higher oxidation potential of the PE-ALD process causing other H_2O side products [1,18].

In Figure 7 we have analyzed the profiles of the O1s signals of the PE-ALD samples at rt (Figure 7a) and at 80 °C (Figure 7b) in more detail. In order to allow a comparison to literature values the spectra are referred in this case to fixed C1s core levels. Here the main signal arising from the Al–O bonds [24,25] is found at 531.2 eV for both samples. The second contribution caused by the additional hydroxyl and carbonate species [24] appear at 532.6 eV and 532.7 eV, respectively.

Our assignment of the peak positions is for thick Al_2O_3 films where the screening of the photo-excited hole is by the electrostatic potentials of the oxide neighbors while screening from the substrate is negligible [26]. It should be mentioned that these values may differ from those of ultra-thin Al-oxide films reported elsewhere [1,24]. We should emphasize again that the individual IS energy positions for the main Al–O signal depends on the preparation condition of the individual films as these influence the dielectric screening significantly [3,6,27].

From the combination of these data with the C1s core level data (Figure 5) it becomes evident that the rt PE-ALD sample has the highest carbonate content leading to distinct contribution at higher IS energy within the O1s core level data. They compete with the above mentioned and below discussed peak shifting to lower IS energy. Therefore the O1s peak maximum of the rt PE-ALD sample is shifted to higher IS energy with respect to the T-ALD 200 °C sample whereas the peak maximum is moved to lower IS energy in the Al2p core level, where the carbonate has no influence. The same fact is due for the 80 °C PE-ALD sample where the O1s peak maxima is almost at the same position like in the T-ALD 200 °C sample but the Al2p exhibits a shift into the same direction like in the other PE-ALD samples.

Relative O/Al ratios

Based on this data analysis the elemental ratio of oxygen to aluminum was determined. We used the peak areas of the Al–O contributions within the O1s and Al2p core levels (i.e., the contributions assigned to COO and OH groups were not considered). We used the element specific cross sections of 0.063467 and of 0.012295 for O1s and Al2p, respectively [28]. The resulting $\mathrm{O1s_{Al–O}/Al2p_{Al–O}}$ ratios are plotted versus the substrate temperature in Figure 8. For the samples prepared at 200 °C substrate temperature we find ratios of 1.46 and 1.47 for both, the T-ALD and the PE-ALD samples. These values are close to the stoichiometric value of 1.5. When the temperature in the PE-ALD process is lowered we observe a significant reduction of the O/Al ratio as shown in Figure 8. It points out that at these lower temperatures (80 °C, rt) the oxygen radicals are less efficient in oxidizing the aluminum precursor. This is true also for the chemisorbed organic precursor molecules.

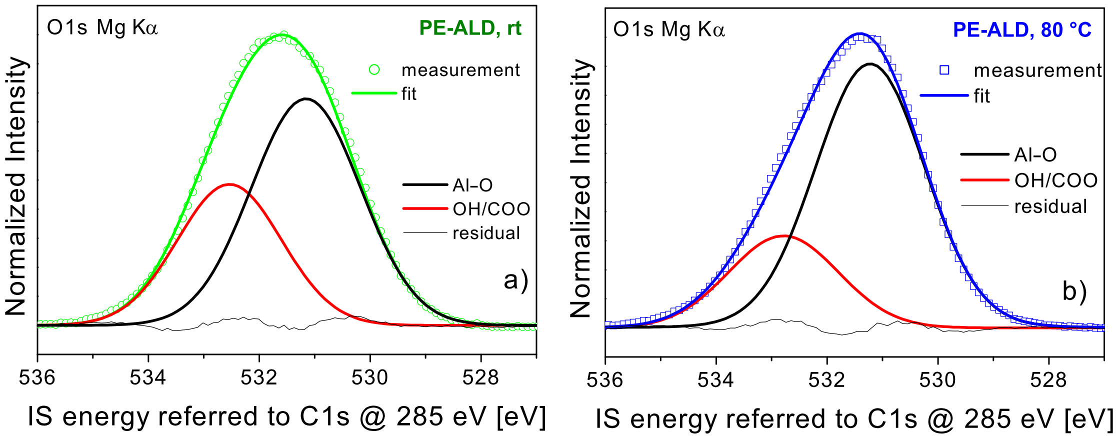

Figure 7: O1s core level spectra (Mg Kα) of the PE-ALD samples prepared at rt (a) and 80 °C (b) substrate temperature. The peak decomposition into Al–O (black curves) and OH/COO components (red) are indicated. The measured data are given by green hollow circles (rt) and blue hollow squares (80 °C) whereas the resulting fitting curve is shown in corresponding line colors (residual: thin black line). The data are normalized to the measured O1s peak maximum of each sample and both diagrams are shown in an identical scale. The IS energy is referred to fixed C1s levels for every sample at 285 eV.

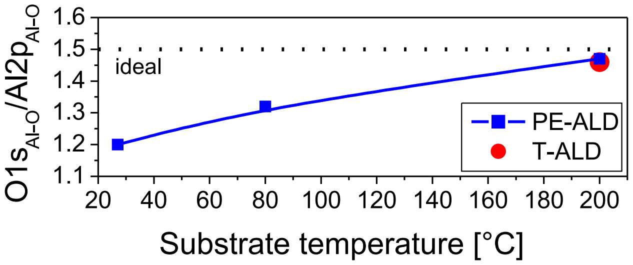

Figure 8: O1s to Al2p elemental ratio versus substrate temperature of PE-ALD layers (blue squares); the data point of the T-ALD film at 200 °C is included (red filled circle). Here, only the Al–O contributions were considered for the analysis. For orientation the ideal stoichiometric value is illustrated by the dashed line.

At first sight our results might contradict the composition results of the Kessels group based on RBS data where oxygen rich layers were found at lower temperatures [1,20]. However, we have analyzed here only the Al–O specific contributions. In case that also OH and COO contributions would be considered for the analysis O/Al ratios of 1.9 and 1.8 would be deduced for the PE-ALD samples at rt and 80 °C substrate temperature, respectively, very similar to the results in [20].

Influence of fixed charges

Regarding the shifts of the IS energy of the O1s and distinctly in the Al2p core levels of the PE-ALD samples we argue that they might be caused by a net negative fixed charge which is built-up in particular in PE-ALD samples as reported in literature [1,18,22,29]. Our capacitance–voltage measurements on these layers (to be reported elsewhere, [23]) indeed yield a negative fixed charge which is in the range of 0.5 to 5×10^{12} cm^{-2} for the PE-ALD samples. For the 200 °C T-ALD sample it is only about 2×10^{11} cm^{-2}.

Tetrahedral coordinated Al has a charge of −3 [29] and can be counted as an aluminum vacancy which can react with an oxygen atom originating from the SiO_2 interface resulting in a net negative charge [1,29]. Moreover, oxygen interstitials may be responsible for the net negative fixed charge [1]. However, the microscopic origin of this charge is still under discussion [1]. Therefore, we plan to conduct X-ray absorption as well as resonant photoemission measurements using synchrotron radiation (SR) in near future.

Now we report on a direct comparison of the 200 °C PE-ALD and T-ALD samples. The results are depicted in Figure 9. First, we focused on the line positions of the O1s (Figure 9a) and Al2p (Figure 9b) core levels using SR and observed the same or only slightly shifted IS energies compared to the lab experiments with Mg Kα excitation (compare to Figure 4a and Figure 4b). The IS energy shifts between the PE-ALD and T-ALD samples in the synchrotron experiment are a bit smaller compared to the Mg Kα lab measurement. This might be due to

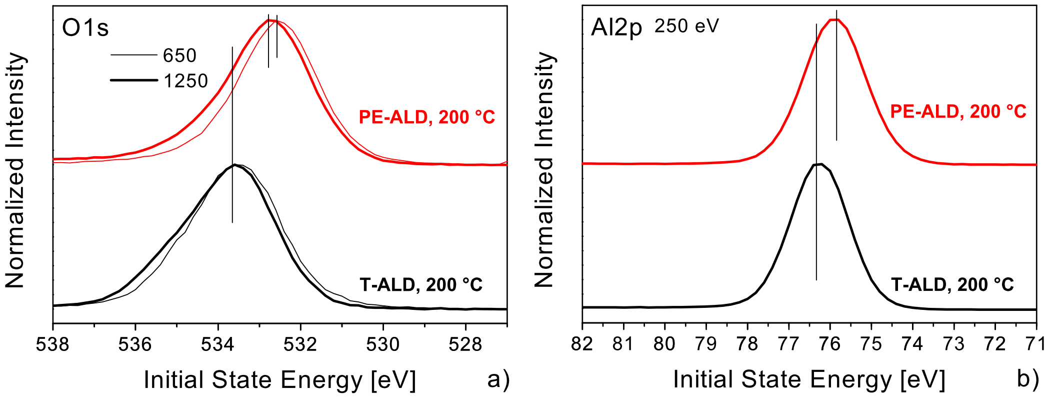

Figure 9: O1s (a) and Al2p (b) core level spectra of the PE-ALD (red curves) and T-ALD layers (black) deposited at 200 °C. These data were recorded with synchrotron excitation. The excitation energies were 650 eV (thick lines) and 1250 eV (thin lines) for the O1s and 250 eV for the Al2p, respectively. The data are normalized to each individual peak maximum and separated vertically, but shown in the same scaling. The IS energy is referred to Fermi energy.

the higher light intensity at the synchrotron which might lead to a filling/defilling of fixed charges. To check further whether the mentioned shifts of the core levels of the PE-ALD samples in comparison to the T-ALD sample originate from some surface bend bending we measured the O1s core level at different excitation energies (Figure 9a). In the T-ALD sample we observe no difference in the line position between the more surface (650 eV) and more bulk sensitive (1250 eV) mode, whereas in the PE-ALD a small shift of 150 meV is within experimental error bars. Therefore we conclude that the shifts in the core levels of the PE-ALD samples are real and not caused by effects like surface bend bending or other experimental uncertainties.

The influence of the substrate is important in these considerations. Bayer et al. report on Al_2O_3 films prepared by T-ALD on ITO and found Al2p IS energies between 74.5 eV and 75.5 eV [30]. On ruthenium and ruthenium oxide we found also values between 74.5 eV and 75.0 eV depending on substrate and film thickness [7]. For these conductive oxide substrates the variation in the core level energies may be attributed to surface diploes caused by adsorbed OH groups. This interpretation is based on the fact that there is a change in the energies of about 0.5 eV when spectra are taken after the precursor pulse and after the oxygen pulse.

In contrast, on non-conductive substrates an interface charge is built up. This is proposed based on electrical studies [29,31] which indicated that a fixed charge is generated at the interface of Al_2O_3/interfacial SiO_2. This interface charge induces Coulomb scattering to the surface channel of a field effect transistor which reduces the electron mobility. In our experiments the interface charges cause the additional shift of the core level energies. The amount of such charges varies depending on the individual preparation conditions.

We like to mention that based on our accurate determination of the IS energy we are able to follow shifts in the samples very accurately. In all samples, the IS energy values of the Al2p, O1s, and the C1s level appear to be different. In fact, the variation of the Al2p IS energy values for the highest charge level amounts 75.3 eV and for the lowest charge level we find a value of 76.3 eV. In total, the shifts of about 1 to 1.5 eV are explained by different charge accumulated. In the PE-ALD samples series (Figure 4, Figure 5 and Figure 6) we find an additional trend as upon increasing temperature there is an additional shift of the O1s and Al2p levels with respect to that of the C1s level. This shift is attributed to a structural change in the Al_2O_3.

To summarize our XPS data analysis, we have identified fragments of the precursor and the H_2O oxidant within the films. OH and COO groups appear in the O1s core level, TMA fragments and carbon–oxygen reaction products up to COO show up in the C1s core level. The relative intensity of both is higher in the PE-ALD films because of the higher reactivity of the plasma enhanced mode. The peak positions of all films are influenced by charged species within the films.

Carbon contamination (EDX, XPS, ellipsometry)

In order to discuss the integration of carbon atoms into the films we conducted energy dispersive X-ray spectroscopy (EDX), XPS C1s core level spectroscopy, and spectroscopic ellipsometry.

The chemical composition of the Al_2O_3 films at different temperatures was investigated by EDX. Hereby, the relation between C-atoms and Al-atoms within the films was determined. Figure 10a displays the ratio of carbon to aluminum depending on the substrate temperature of the film. With

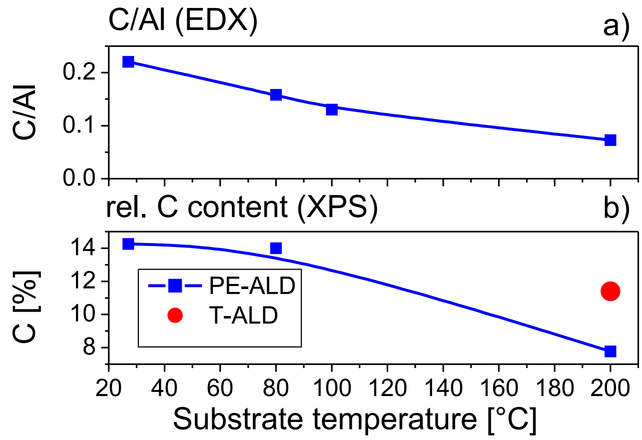

Figure 10: Carbon content within PE-ALD layers (blue squares) versus substrate temperature determined by EDX (a) and XPS (b). For comparison the XPS result of the T-ALD film at 200 °C is included (red filled circle).

decreasing deposition temperature, the carbon proportion within the Al_2O_3 films increases significantly.

The same trend is observed in the XPS data (refer to Figure 5). Here the C1s peak areas with a cross section of 0.021314 [28] were related to the total sum of the cross section weighted O1s, Al2p and C1s peak areas of every sample. The resulting total carbon concentrations are shown in Figure 10b; the corresponding C1s core level data are presented in Figure 5. Remarkably, the PE-ALD at 200 °C exhibits a clear reduction to around 8% compared to 11% of the T-ALD at this temperature. The lower carbon content of the PE-ALD sample at 200 °C is also evident by a qualitative comparison of the normalized C1s core levels as depicted in Figure 5. At lower temperatures of 80 °C and rt the carbon concentration increases to about 14%. As the carbon concentration shows the same trend as the O/Al ratios reported above we argue that the metal precursor interaction with the substrate is not completed leading to higher carbon and lower oxygen contents.

This fact is further supported by carbonate contributions rising in the C1s core level data of the PE-ALD samples prepared at 80 °C and rt (see Figure 5). In the PE-ALD combustion-like reactions occur with the formation of COO and H_2O [1] which may also support secondary reaction pathways [18] leading for example to carbonates and carbon contamination.

It has to be pointed out that the XPS measurements were performed ex-situ and the results might be strongly influenced by surface contamination due to the ex-situ handling of the samples in particular in the surface sensitive XPS method. Nevertheless, our elemental composition data confirm findings of other authors based on RBS data [1,20]. In addition, the observed trend of carbon components within the films is similar to the EDX measurements shown above and the infrared data reported now.

The incorporation of CH-molecule groups was also monitored by means of infrared spectroscopy. For this purpose, spectroscopic ellipsometry is particularly suitable because hereby the influence of substrate properties can be neglected and no distracting overlays with substrate bands occur and the measured spectra can be directly fitted using an appropriate model. The optical properties of the deposited films were modeled using a Brendel oscillator model. The parameters of the oscillator model are: oscillator frequency, oscillator strength, oscillator damping, and a distribution factor taking into account the influence of surrounding materials of the single oscillator. This model can be applied for all absorbing molecule groups in the Al_2O_3 film. In the infrared the thin native oxide film cannot be measured and was neglected. Figure 11 shows the measured spectral dependency between the extinction coefficients (absorption indices) of PE-ALD films with different deposition temperatures. In the graph the positions of oscillation bands caused by Al–O, methyl (CH_3), and CH groups are indicated. For lower growth temperatures (80 °C, rt) the spectra exhibit distinct contributions of methyl and CH groups indicating not terminated surface reactions of the TMA precursor. At 200 °C no more carbon-based bands are detectable. In reverse, with decreasing concentration of carbon groups, the absorption by the Al–O oscillation band increases indicative for efficient ALD Al_2O_3 reaction [15]. These data are in good agreement to the O/Al ratios and the EDX and XPS carbon measurements. However in the 200 °C PE-ALD sample no more CH_x bands are detected, whereas the XPS still reflects carbon and carbonate contributions within the films. XPS is a more surface sensitive method than the infrared spectroscopy. Therefore, we conclude that CH_x bonds are integrated within the volume of the PE-ALD layers at lower temperatures, whereas carbon contamination and carbonate formation is occurring at the surface.

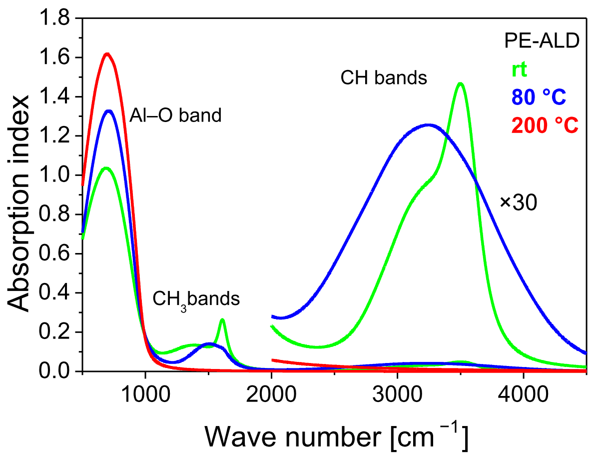

Figure 11: Infrared absorption index data for PE-ALD layers deposited at 200 °C (red curve), 80 °C (blue) and rt (green). The region of the CH bands is magnified (×30).

Conclusion

Thin homogenous Al_2O_3 layers were successfully produced by standard thermal (200 °C) and plasma enhanced ALD in the SENTECH SI ALD LL system at substrates temperatures ranging from 200 °C down to rt. Comparing the 200 °C processes similar refractive indices of 1.64 and oxygen to aluminum elemental ratios near the stoichiometric value of 1.5 were observed. However, the PE-ALD at this temperature exhibits favorably increased growth rates and reduced carbon contaminations. The reduction of the deposition temperature of the PE-ALD down to rt leads to the integration of carbon, COO and CH_x compounds. Methyl groups and derivatives of the

TMA precursor are integrated into the film due to not completed surface reactions of the aluminum and oxygen precursors. As a result the refractive index and oxygen to aluminum elemental ratio are decreased whereas the growth rate is increased. Nevertheless, the homogeneity of the film growth is not significantly influenced. We conclude that the PE-ALD process at lower temperatures needs therefore an optimization of the cycle and purge time combinations.

Our results contribute to possible deposition on thermally fragile substrates [8,15] and to higher throughput processes in industrial applications [18].

Experimental

SENTECH's SI ALD LL system shown schematically in Figure 12 is equipped with a plasma source for PE-ALD processes. The capacitive coupled plasma source (CCP source) was developed by SENTECH Instruments and guarantees a stable pulse operation in ALD cycles. Furthermore, no automatic matching of CCP source during PE-ALD process is needed: the plasma source is pulsed with constant matching parameters during the deposition process. Substrate shuck, reactor and precursor lines are equipped with different heaters. The substrate temperature can be controlled in the range between room temperature and 500 °C, reactor and precursor lines can be heated up to 150 °C and 200 °C respectively. The system consists of 3 precursor lines.

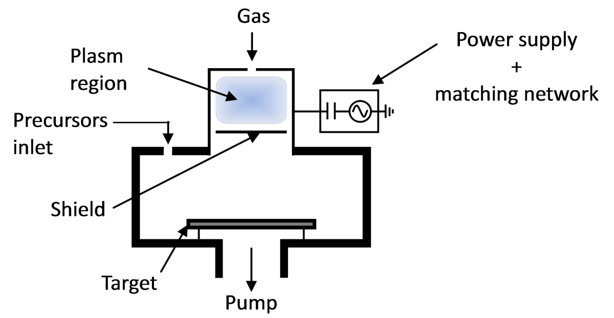

Figure 12: Reactor and CCP source of the SENTECH ALD system: SI ALD LL.

The true remote CCP source, driven by a 13.56 MHz generator, is attached to the upper flange of the reactor. During the deposition process the substrate is placed outside of the plasma generation region; the coated surface is not bombarded with destructive ions and does not see the light from plasma generation region.

PE-ALD Al_2O_3 films were deposited on 4” n-type silicon wafers (consisting of a native oxide of approximately 1.5 nm) by the SI ALD LL system at 200 °C, 150 °C, 100 °C, 80 °C, and 27 °C (rt) substrate temperature. Nitrogen (N_2) with 40 sccm flow was used as carrier gas for TMA. Atomic oxygen was generated by SENTECH's CCP source. Thereby, a constant oxygen flow rate of 75 sccm was adjusted. The pulse duration of the TMA was 120 ms whereas for the oxygen semi-cycle 5 s (200 °C), 6 s (80 °C) or 7 s (rt) were chosen. The plasma source was run in a pulsed mode as it was operated only during the oxygen step of the ALD cycle with a power of 100 W except for the rt sample (50 W). Process pressure was 20 Pa.

For the T-ALD also N_2 with 120 sccm flow rate was used as carrier gas for TMA and H_2O which was applied as oxygen source. Here, the pulse duration was 60 ms for both the TMA and H_2O. Process pressure was 12 Pa.

Layers of about 50 nm were produced for the ellipsometry investigation of the film properties. To determine film thickness and refractive index spectroscopic ellipsometry (SE 800, SENTECH Instruments GmbH) was used within the UV–vis spectral range. The SENTECH SE 800 is equipped with a scan analyzer for highly accurate spectra. The measurements were performed at an angle of incidence of 70° using a spectral range of 280–850 nm (1.5–4.4 eV). The accumulated spectra were modeled using SpectraRay 3 software. The model layers comprised a Si substrate, a fixed layer of 1.5 nm native SiO_2 and the deposited Al_2O_3 film. The SiO_2 and the Al_2O_3 layers were defined as Cauchy layers. For the detection of CH_x compounds within the deposited films spectroscopic ellipsometry in the middle infrared wavelength range (MIR) the SENDIRA ellipsometer from SENTECH Instruments GmbH was performed. A Step scan analyser for high spectroscopic accuracy was used at an angle of incidence of 70°. Modelling was carried out using SpectraRay 3 software. The model layer comprised Al_2O_3 on Si-substrate and the layer was modelled over the wave number range of 600 cm^{-1} to 4500 cm^{-1}. Additionally, EDX was applied on these samples (≈50 nm).

For XPS measurements Al_2O_3 films with a thickness of about 10 nm were prepared in order to avoid charging of the samples. XPS measurements were performed either by Specs Mg Kα source (in the lab) or by synchrotron radiation (undulator beamline U49/2-PGM2 at BESSY-II in Berlin/Adlershof). The data were recorded using semispherical electron analyzers made by Leybold–Heraeus (lab) or Omicron NanoTechnology GmbH (EA125 at BESSY). Both, beam line monochromator and analyzers are controlled for their accuracy in determining the IS energy by running Au4f (87 eV IS energy) spectra at different excitation energies. All spectra shown in this contribution were Shirley background corrected [32]. The kind of normalization of the XPS spectra is given separately in every related figure caption.

Acknowledgements

The authors like to thank experimental support of. G. Beuckert and the BESSY staff. This work is supported by German Federal Ministry of Education and Research (BMBF, 03IN2V4A, 03IN2V4B).

References

1. Dingemans, G.; Kessels, W. M. M. *J. Vac. Sci. Technol., A* **2012,** *30,* 040802. doi:10.1116/1.4728205
2. Sarkar, S.; Culp, J. H.; Whyland, J. T.; Garvan, M.; Misra, V. *Org. Electron.* **2010,** *11,* 1896–1900. doi:10.1016/j.orgel.2010.08.020
3. Henkel, K.; Torche, M.; Sohal, R.; Karavaev, K.; Burkov, Y.; Schwiertz, C.; Schmeißer, D. *Phys. Status Solidi A* **2011,** *208,* 317–329. doi:10.1002/pssa.201026404
4. Cho, M.; Park, H. B.; Park, J.; Hwang, C. S.; Lee, J.-C.; Oh, S.-J.; Jeong, J.; Hyun, K. S.; Kang, H.-S.; Kim, Y.-W.; Lee, J.-H. *J. Appl. Phys.* **2003,** *94,* 2563–2571. doi:10.1063/1.1590414
5. Henkel, K.; Seime, B.; Paloumpa, I.; Müller, K.; Schmeißer, D. *IOP Conf. Ser.: Mater. Sci. Eng.* **2010,** *8,* 012036. doi:10.1088/1757-899X/8/1/012036
6. Tallarida, M.; Weisheit, M.; Kolanek, K.; Michling, M.; Engelmann, H.-J.; Schmeißer, D. *J. Nanopart. Res.* **2011,** *13,* 5975–5983. doi:10.1007/s11051-011-0319-x
7. Tallarida, M.; Kukli, K.; Michling, M.; Ritala, M.; Leskelä, M.; Schmeißer, D. *Chem. Mater.* **2011,** *23,* 3159–3168. doi:10.1021/cm200276z
8. Groner, M. D.; Fabreguette, F. H.; Elam, J. W.; George, S. M. *Chem. Mater.* **2004,** *16,* 639–645. doi:10.1021/cm0304546
9. Potts, S. E.; Schmalz, L.; Fenker, M.; Díaz, B.; Światowska, J.; Maurice, V.; Seyeux, A.; Marcus, P.; Radnóczi, G.; Tóth, L.; Kessels, W. M. M. *J. Electrochem. Soc.* **2011,** *158,* C132–C138. doi:10.1149/1.3560197
10. Peng, Q.; Lewis, J. S.; Hoertz, P. G.; Glass, J. T.; Parsons, G. N. *J. Vac. Sci. Technol., A* **2012,** *30,* 010803. doi:10.1116/1.3672027
11. Prasittichai, C.; Hupp, J. T. *J. Phys. Chem. Lett.* **2010,** *1,* 1611–1615. doi:10.1021/jz100361f
12. Tien, T.-C.; Pan, F.-M.; Wang, L.-P.; Tsai, F.-Y.; Lin, C. *J. Phys. Chem. C* **2010,** *114,* 10048–10053. doi:10.1021/jp1023229
13. Le Formal, F.; Tétreault, N.; Cornuz, M.; Moehl, T.; Grätzel, M.; Sivula, K. *Chem. Sci.* **2011,** *2,* 737–743. doi:10.1039/c0sc00578a
14. Jung, Y. S.; Cavanagh, A. S.; Dillon, A. C.; Groner, M. D.; George, S. M.; Lee, S.-H. *J. Electrochem. Soc.* **2010,** *157,* A75–A81. doi:10.1149/1.3258274
15. George, S. M. *Chem. Rev.* **2010,** *110,* 111–131. doi:10.1021/cr900056b
16. Speck, F.; Ostler, M.; Röhrl, J.; Emtsev, K. V.; Hundhausen, M.; Ley, L.; Seyller, T. *Phys. Status Solidi C* **2010,** *7,* 398–401. doi:10.1002/pssc.200982496
17. Heil, S. B. S.; Kudlacek, P.; Langereis, E.; Engeln, R.; van de Sanden, M. C. M.; Kessels, W. M. M. *Appl. Phys. Lett.* **2006,** *89,* 131505. doi:10.1063/1.2357886
18. Profijt, H. B.; Potts, S. E.; van de Sanden, M. C. M.; Kessels, W. M. M. *J. Vac. Sci. Technol., A* **2011,** *29,* 050801. doi:10.1116/1.3609974
19. Knoops, H. C. M.; Langereis, E.; van de Sanden, M. C. M.; Kessels, W. M. M. *J. Electrochem. Soc.* **2010,** *157,* G241–G249. doi:10.1149/1.3491381
20. van Hemmen, J. L.; Heil, S. B. S.; Klootwijk, J. H.; Roozeboom, F.; Hodson, C. J.; van de Sanden, M. C. M.; Kessels, W. M. M. *J. Electrochem. Soc.* **2007,** *154,* G165–G169. doi:10.1149/1.2737629
21. Jinesh, K. B.; van Hemmen, J. L.; van de Sanden, M. C. M.; Roozeboom, F.; Klootwijk, J. H.; Besling, W. F. A.; Kessels, W. M. M. *J. Electrochem. Soc.* **2011,** *158,* G21–G26. doi:10.1149/1.3517430
22. Rafi, J. M.; Zabala, M.; Beldarrain, O.; Campabadal, F. *J. Electrochem. Soc.* **2011,** *158,* G108–G114. doi:10.1149/1.3559458
23. Henkel, K.; Gargouri, H.; Gruska, B.; Arens, M.; Tallarida, M.; Schmeißer, D. *J. Vac. Sci. Technol., A* **2014,** in press.
24. Gougousi, T.; Barua, D.; Young, E. D.; Parsons, G. N. *Chem. Mater.* **2005,** *17,* 5093–5100. doi:10.1021/cm0510965
25. Paparazzo, E. *Appl. Surf. Sci.* **1986,** *25,* 1–12. doi:10.1016/0169-4332(86)90021-8
26. Himpsel, F. J.; Morar, J. F.; McFeely, F. R.; Pollak, R. A.; Hollinger, G. *Phys. Rev. B* **1984,** *30,* 7236–7241. doi:10.1103/PhysRevB.30.7236
27. Sohal, R.; Torche, M.; Henkel, K.; Hoffmann, P.; Tallarida, M.; Schmeißer, D. *Mater. Sci. Semicond. Process.* **2006,** *9,* 945–948. doi:10.1016/j.mssp.2006.10.047
28. Yeh, J. J.; Lindau, I. *At. Data Nucl. Data Tables* **1985,** *32,* 1–155. doi:10.1016/0092-640X(85)90016-6
29. Johnson, R. S.; Lucovsky, G.; Baumvol, I. *J. Vac. Sci. Technol., A* **2001,** *19,* 1353–1360. doi:10.1116/1.1379316
30. Bayer, T. J. M.; Wachau, A.; Fuchs, A.; Deuermeier, J.; Klein, A. *Chem. Mater.* **2012,** *24,* 4503–4510. doi:10.1021/cm301732t
31. Hiratani, M.; Torii, K.; Shimamoto, Y.; Saito, S.-I. *Appl. Surf. Sci.* **2003,** *216,* 208–214. doi:10.1016/S0169-4332(03)00432-X
32. Repoux, M. *Surf. Interface Anal.* **1992,** *18,* 567–570. doi:10.1002/sia.740180719

License and Terms

Beilstein Journal
of Nanotechnology

Synthesis of indium oxi-sulfide films by atomic layer deposition: The essential role of plasma enhancement

Cathy Bugot[*], Nathanaëlle Schneider, Daniel Lincot
and Frédérique Donsanti[*]

Full Research Paper

Address:
Institut de Recherche et Développement sur l'Energie Photovoltaïque (IRDEP), UMR 7174 – EDF – CNRS – Chimie Paristech, 6 quai Watier, 78401 Chatou, France

Email:
Cathy Bugot[*] - cathy-externe.bugot@edf.fr;
Frédérique Donsanti[*] - frederique.donsanti@edf.fr

* Corresponding author

Keywords:
atomic layer deposition; buffer layer; indium oxi-sulfide; plasma enhancement; thin film solar cells

Beilstein J. Nanotechnol. **2013,** *4,* 750–757.
doi:10.3762/bjnano.4.85

Received: 31 July 2013
Accepted: 24 October 2013
Published: 13 November 2013

This article is part of the Thematic Series "Energy conversion applications of atomic layer deposition".

Guest Editor: J. Bachmann

Abstract

This paper describes the atomic layer deposition of $In_2(S,O)_3$ films by using $In(acac)_3$ (acac = acetylacetonate), H_2S and either H_2O or O_2 plasma as oxygen sources. First, the growth of pure In_2S_3 films was studied in order to better understand the influence of the oxygen pulses. X-Ray diffraction measurements, optical analysis and energy dispersive X-ray spectroscopy were performed to characterize the samples. When H_2O was used as the oxygen source, the films have structural and optical properties, and the atomic composition of pure In_2S_3. No pure In_2O_3 films could be grown by using H_2O or O_2 plasma. However, $In_2(S,O)_3$ films could be successfully grown by using O_2 plasma as oxygen source at a deposition temperature of $T = 160$ °C, because of an exchange reaction between S and O atoms. By adjusting the number of In_2O_3 growth cycles in relation to the number of In_2S_3 growth cycles, the optical band gap of the resulting thin films could be tuned.

Introduction

Chalcopyrite-type thin film solar cells that are based on a $Cu(In,Ga)Se_2$ (CIGS) absorber have reached high efficiencies, up to 20.3% [1] in 2011 and 20.4% [2] on flexible substrates in 2013. The best efficiencies were obtained by using cadmium sulfide (CdS) as buffer layer in solar cells with a glass/Mo/CIGS/CdS/i-ZnO/ZnO:Al stack. The buffer layer is an n-type semiconductor that forms the p–n junction with the p-type CIGS absorber, and also modifies the CIGS surface chemistry, which is usually too sensitive for a direct deposition of the window layers. However, because of the toxicity of cadmium and the low optical band gap of CdS (2.4 eV [3]) that limits the light conversion of CIGS in the UV range of the solar spectrum, alternative materials have been developed. Most Cd-free buffer layers are based on zinc and indium-compounds, with current record efficiencies obtained by chemical bath deposition (CBD, 19.7% and 19.1% for Zn(S,O,OH) [4,5], 15.7% for In(S,O,OH) [6]) or atomic layer deposition (ALD, 18.5% for Zn(O,S) [7], 18.1% for (Zn,Mg)O [8], 16.4% for In_2S_3 [9], and 18.2% for (Zn,Sn)O [10]). Recently, our group has synthesized new mixed films of ZnS/In_2S_3 by using ALD and applied them as buffer layers in CIGS solar cells [11,12]. ALD is based on sequential self-saturated reactions that allows the conformal and uniform growth of thin films with a high control of their properties [13-15]. It is therefore a suitable technique for the deposition of buffer layers. Platzer-Björkman et al. have used ALD to improve the energy-band alignment between the CIGS and the front electrode by controlling the oxygen concentration in Zn(S,O) buffer layers [4,16]. Oxygen-doping of In_2S_3 films is known to increase their optical band gap value [6,17,18]. Indeed, by O-doping of In_2S_3 films deposited by thermal evaporation, Barreau et al. could increase the optical band gap value of In_2S_3 thin films from 2.1 to 2.9 eV [17]. In the same way, by using the spray pyrolysis technique, Maha et al. have inserted sulfur atoms in In_2O_3 thin films and obtained optical band gaps in the range from 3.85 to 3.96 eV [18]. Thus, based on our previous results and those studies, we became interested in adjusting the optical properties of In_2S_3 by incorporating oxygen atoms while using the advantages of ALD. Typical ALD processes for the deposition of In_2S_3 and In_2O_3 are referenced in Table 1. As ALD processes of In_2O_3 report relatively small growth rates, we will consider the case of plasma enhancement. Indeed, plasma-enhanced ALD (PEALD), in which various reactive species are generated, has been the key for the development of fast thin-film deposition processes at low temperature. It is widely used to enhance the thin-film deposition of materials such as Al_2O_3, ZnO, Ta_2O_5, TiN, TaN and SiN_x [19].

In this study, ALD and PEALD have been used to synthesize $In_2(S,O)_3$ thin films and carry out optical band-gap engineering. The structural, optical and growth properties of the films will be studied and the role of the plasma will be discussed.

Results

Study of $In(acac)_3$, H_2S and H_2O system

First, a controlled growth of pure In_2S_3 films was established and the film properties were measured in order to clearly identify the influence of oxygen pulse later in the study. For that, In_2S_3 growth was achieved in the temperature range between 140 and 240 °C. An In_2S_3 growth cycle consists of the following steps: $In(acac)_3$ exposure/N_2 purge/H_2S exposure/N_2 purge = 0.1/5/0.1/5 s, the relative long purge time being chosen to ensure a good homogeneity. Figure 1a shows the growth rate of In_2S_3 thin films at various temperatures. It globally increases with the temperature. An ALD window can be speculatively observed between 160 °C and 200 °C with a mean growth rate of 0.84 Å/cycle. The variation of the In_2S_3 growth rate with different $In(acac)_3$ pulse lengths at a process temperature of 160 °C is illustrated in Figure 1b. This variation only slightly influences the growth rate and a saturation by lengthening the precursor pulse is not observed. The data suggest that the results displayed on Figure 1a may not have been obtained under completely self-limiting conditions. Structural and optical properties of the films were also investigated. In_2S_3 thin films have an amorphous structure for deposition temperatures below 180 °C and a β-tetragonal crystal structure at higher temperatures. Their indirect optical band gap varies from 2.0 eV to 2.2 eV.

Then, we attempted to synthesize $In_2(S,O)_3$ film by inserting an In_2O_3 growth cycle. For this H_2O was pulsed, instead of H_2S in the growth of pure In_2S_3, which led to the supercycles $n\cdot\{In_2S_3\} + \{In_2O_3\}$ with n = 1,2,3,5,9,14,19, which corres-

Table 1: Typical ALD processes for the deposition of In_2O_3 and In_2S_3.

reactant A	reactant B	temperature (°C)	growth rate (Å/cycle)	reference
		indium oxide		
$InCl_3$	H_2O	500	0.27	[20]
InCp	$O_3/O_2/H_2O$	250	1.3/0.16/0.068	[21]
InCp	H_2O & O_2	100–250	1.0–1.6	[22]
TmIn	H_2O	217	0.39	[23]
$In(acac)_3$	H_2O/O_3	165–225	0.2/0.12	[24]
		indium sulfide		
$InCl_3$	H_2S	300	1.4	[25]
$In(acac)_3$	H_2S	160, 180, 160, 150	0.6, 0.7, 0.44, 0.3	[9,26-28]

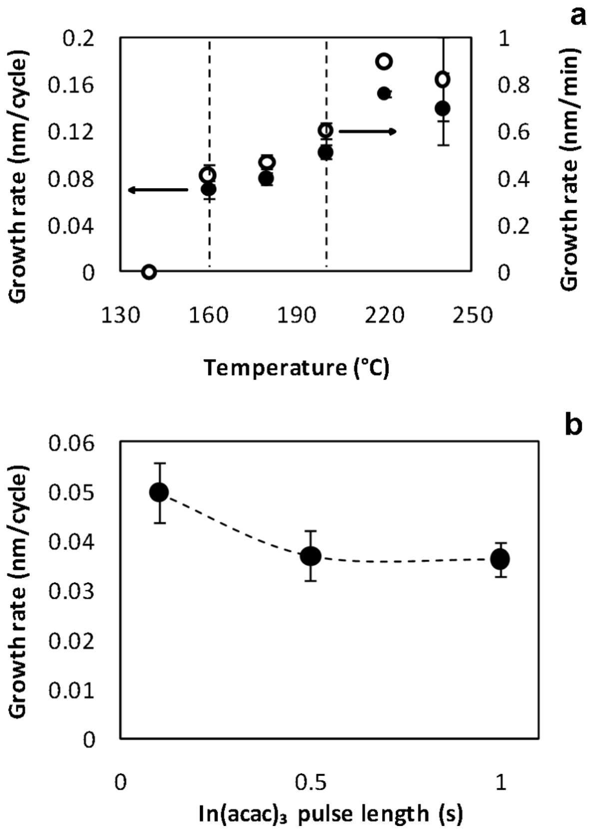

Figure 1: Growth rate of pure In_2S_3 a) as function of the process temperature b) as function of the In(acac)$_3$ pulse length.

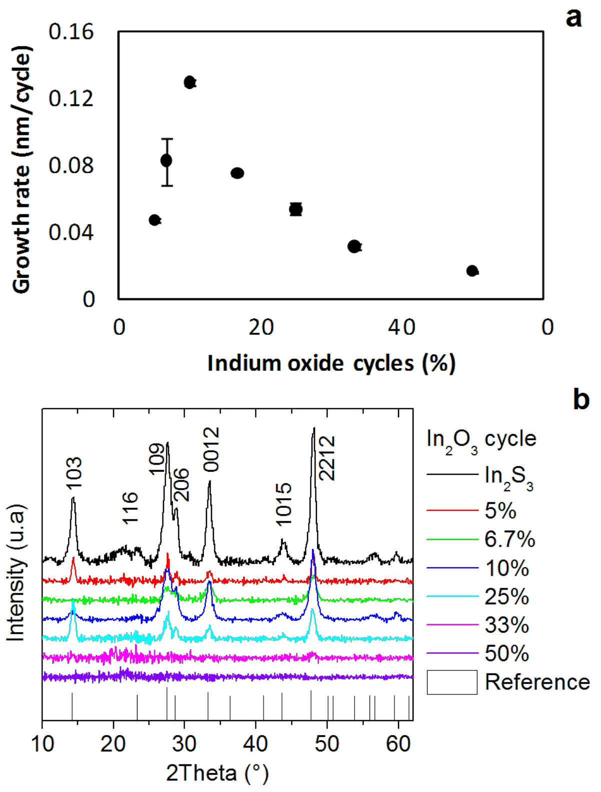

Figure 2: Influence of the number of In_2O_3 cycles on (a) the growth rate while using H_2O as oxygen precursor and (b) GIXRD diffractogram. The reference diffraction pattern for In_2S_3 is taken from the database JCPDS 00-005-0731.

pond to ratios of {50%, 33%, 25%, 10%, 6.7%, 5%} of In_2O_3 cycles at a deposition temperature of 200 °C. All samples were deposited performing a total of 2000 growth cycles, i.e., 100 supercycles for $n = 19$, 133 supercycles for $n = 14$, etc. Energy dispersive X-ray spectroscopy analysis was performed on the samples and gave atomic ratios of 0.4 for In/(In+S) and 0.6 for S/(In+S), which correspond to typical In_2S_3 atomic ratios. The oxygen contents are similar to those of pure In_2S_3 films, which is assigned to the oxygen contamination of the substrate. Those results were confirmed by GI-XRD measurements. They were performed to investigate the influence of the H_2O pulse on the microstructure of the films (Figure 2b). Not all samples were crystalline and the crystalline ones can be attributed to β-In_2S_3 with a random orientation by comparing the diffraction patterns with the reference data and with the literature [27]. Indeed, we should observe a peak shift due to increasing oxygen doping when changing the In_2O_3/In_2S_3 ratio. However, the peaks remain at the same diffraction angles. Comparing the FWHM of the (109) peak, the maximum FWHM measured was 1.2° for the 10%-In_2O_3 sample, which corresponds to the thickest film. In general it can be said that the thinner the films, the lower the FWHM. From these observations, it seems that we obtained In_2S_3 films only.

Thin films optical absorption were determined from transmittance (T) and reflectance (R) measurements by using the following formula [29]

$$\alpha = -\frac{1}{t}\cdot\ln\left(\frac{(1-T)}{R}\right),$$

where α is the absorption coefficient and t is the film thickness. Figure 3 shows absorption spectra of the thin films. They are presented in the form of $(\alpha)^{0.5} = f(E)$, which is linear for indirect band gap materials and allows for the determination of the optical transition. The optical band gaps correspond to an indirect transition in the range from 1.9 to 2.2 eV, which is roughly similar to that of pure In_2S_3 film optical properties. No correlation could be found between either the ratio of In_2O_3 cycles or the film thickness and the optical measurements. These results are in accordance with the observations of the structural analysis. Consequently, this method is not suitable to synthesize $In_2(S,O)_3$ thin films. In parallel, we attempted to synthesize pure In_2O_3 films from In(acac)$_3$ and H_2O at temperatures of 160 and 200 °C. This remained unsuccessful, because no films could be grown under these conditions.

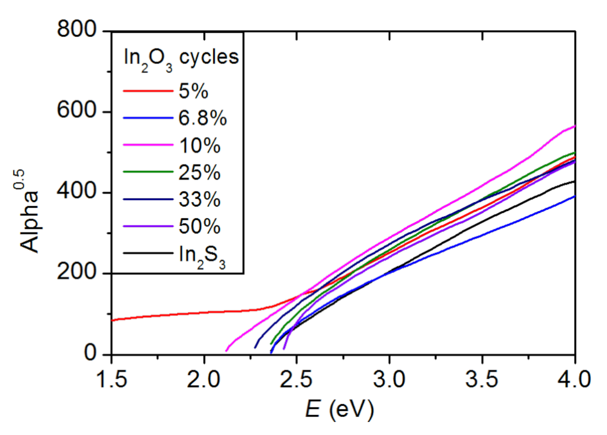

Figure 3: Influence of the ratio of In_2O_3 cycles on the film absorption spectra when using H_2O as oxygen precursor.

Study of the In(acac)$_3$, H_2S and O_2 plasma system

As O_2 plasma is known to have a different reactivity, it was evaluated as potential oxygen source for the deposition of $In_2(S,O)_3$. Thin film syntheses were performed by incorporating In_2O_3 growth cycles that use O_2 plasma pulses in the growth of In_2S_3: In(acac)$_3$ exposure/N_2 purge/O_2 + plasma exposure/N_2 purge = 0.1/5/7/3 s in the following supercycles $n\cdot\{In_2S_3\} + 2\cdot\{In_2O_3\}$ with n = 15,20,25,30,35,40 which correspond to ratios of {11.8%, 9.1%, 7.4%, 6.25%, 5.4%, 4.8%} of In_2O_3 cycles at a deposition temperature of 160 °C. A total of 2000 cycles was achieved for all samples as described in the previous section. The dependence of the growth rate on the number of In_2O_3 cycles is shown in Figure 4a. When increasing the ratio from 4.8% to 9.1%, the growth rate increases up to 1.4 Å/cycle and then decreases again. The variation of the film thickness with the number of ALD cycles for a ratio of 10% of In_2O_3 cycles is illustrated in Figure 4b. A linear growth is observed up to 1500 ALD cycles. GIXRD measurements revealed an amorphous structure in all the samples.

Transmittance and reflectance measurements were carried out on the $In_2(S,O)_3$ samples. Figure 5 shows the transmittance of $In_2(S,O)_3$ films as a function of the percentage of In_2O_3 cycles. A shift of the onset absorption can be observed, which suggests an evolution in the properties of the films. The indirect optical transitions were identified for all samples from their respective absorption spectra (Figure 6a). The values are plotted as a function of the ratio of In_2O_3 cycles in Figure 6b. The maximum value corresponds to the theoretical optical gap of In_2O_3 [30]. The optical band gaps vary from 2.2 ± 0.1 eV for pure In_2S_3 to 3.3 ± 0.1 eV for $In_2(S,O)_3$ and increase with the number of In_2O_3 cycles during the deposition process of In_2S_3.

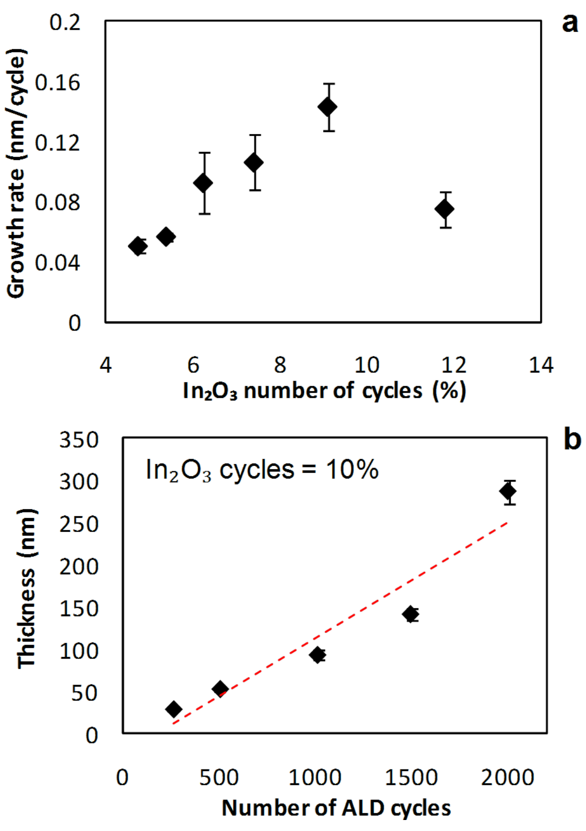

Figure 4: Influence of a) the number of In_2O_3 cycles on the growth rate b) the number of process cycles on the film thickness when using O_2 plasma as oxygen precursor. The dotted line is a guide to the eyes.

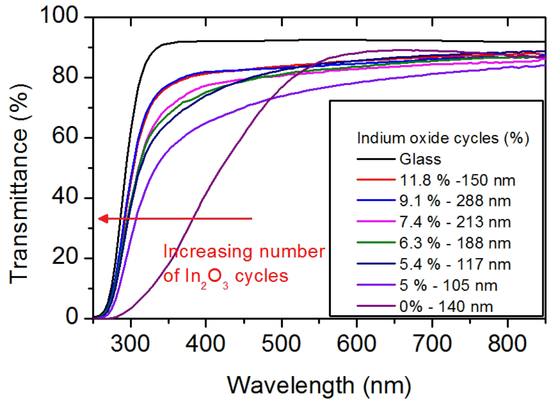

Figure 5: Influence of the number of In_2O_3 cycle on the film transmittance when using O_2 plasma as oxygen precursor.

The atomic ratios of oxygen, sulfur and indium determined by using EDX are presented in Table 2 and correlated to the optical band gap values. The dependence of the atomic ratio of oxygen and the optical band gap on the number of In_2O_3 cycles is not clear. In general, high oxygen concentrations of more than 66 atom % were measured in the films.

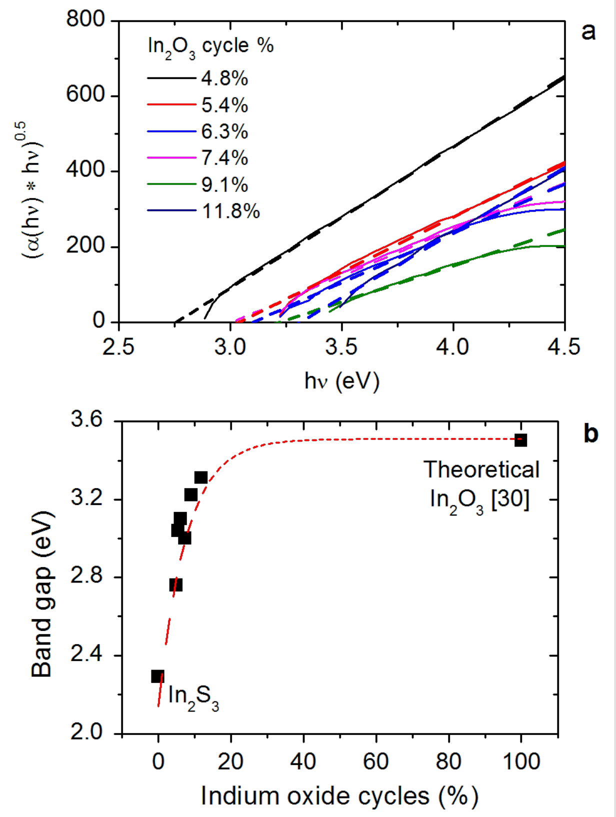

Figure 6: Influence of the number of In_2O_3 cycles a) on the absorption and b) optical band gap when using O_2 plasma as oxygen precursor. The dotted line is a guide to the eyes.

We also tried to synthesize $In_2(S,O)_3$ by using a single O_2 plasma pulse instead of In_2O_3 pulse cycles. The following cycle program was used: 20·{In_2S_3} + 2·{O_2+plasma exposure}/N_2 purge with the same process parameters. This corresponds to 9.1% of indium cycles, which can be compared to the previous deposition with a pulse of $In(acac)_3$ before the O_2 plasma exposure. Table 3 shows the properties of these two samples, along with those of pure In_2S_3. Even without the $In(acac)_3$ pulse, O and S atomic ratios indicate that the synthesized film corresponds to a $In_2(S,O)_3$ film and no significant differences were observed between the samples.

The growth of $In_2(S,O)_3$ growth could be achieved when using O_2 plasma as oxygen precursor. The maximum growth rate was 1.4 Å/cycle, which is higher than the growth rates of In_2S_3 shown in Figure 1 and those reported in the literature for this deposition temperature [9,26-28]. Optical measurements revealed an onset absorption moving to higher energies when increasing the number of In_2O_3 cycles. At the same time, the optical band gap increased from 2.2 eV to 3.3 eV for In_2O_3 cycle ratios in the range from 0 to 11.8%. EDX analysis showed that those films have a high oxygen content. Finally, all attempts to synthesize pure In_2O_3 films from $In(acac)_3$ and O_2 plasma remained unsuccessful .

Discussion

It has been observed that inserting an In_2O_3 cycle during the deposition of In_2S_3 when using H_2O as oxygen precursor has no influence on the oxygen content and on the film properties. It only affects the growth rate as the thickness varies. Attempts to synthesize pure In_2O_3 thin films were also unsuccessful, which suggests a low reactivity of H_2O towards $In(acac)_3$. Several authors reported the difficulty to synthesize In_2O_3 by ALD using β-diketonates ($In(acac)_3$, In(hfac = hexafluoropenta-

Table 2: EDX measurements data from $In_2(S,O)_3$ thin films when using O_2 plasma.

In_2O_3 (%)	optical band gap (eV)	(O+S)/(In+S+O) (atom %)	In/(In+S+O) (atom %)	S/(In+S+O) (atom %)	O/(In+S+O) (atom %)
4.80	2.76	83	17	15	68
5.41	3.04	85	15	10	75
6.25	3.10	85	15	11	74
7.41	3.00	80	20	14	66
9.09	3.22	79	21	10	69
11.76	3.31	83	17	9	74

Table 3: Comparison between $In_2(S,O)_3$ films, synthesized with and without $In(acac)_3$ during the oxidation pulse, and In_2S_3.

program	E_g (eV)	growth rate (Å/cycle)	In/(In+S+O) (atom %)	S/(S+O) (atom %)	O/(S+O) (atom %)
20·{In_2S_3} + 2·{In_2O_3}	3.2 ± 0.1	1.4 ± 0.2	21	13	87
20·{In_2S_3} + 2·O_2 plasma	3.3 ± 0.1	1.2 ± 0.2	17	15	85
In_2S_3	2.2 ± 0.2	0.7 ± 0.08	35	70	30

dionate)$_3$, In(thd = 2,2,6,6-tetramethyl-3,5-heptanedioneate)) and water [20,21,25]. In most cases, they assigned the low growth rates or the absence of grown films to the low reactivity of water toward β-diketonates.

As no pure In_2O_3 films could be grown in our case, the synthesis of mixed films by a simple addition of two layers, i.e., In_2O_3 + In_2S_3, is not possible. However, the deposition of ternary materials can also occur via exchange reactions. For instance, when synthesizing zinc indium sulfide (ZIS) thin films, substitution mechanisms between diethylzinc (DEZ) and In_2S_3 could be demonstrated [11]. Similar mechanisms also occur when inserting H_2O in pure ZnS during the growth of Zn(S,O) by using ALD [4,16]. Such processes do not seem to occur in our case, because the $In_2(S,O)_3$ deposition method that uses H_2O remained unsuccessful. A possible thermodynamic explanation for the unfavorable deposition of $In_2(S,O)_3$ using H_2O as oxygen precursor is that the following exchange reaction is endothermic and thus unlikely to occur [31].

$$\begin{aligned}&In_2S_3(s) + 3\,H_2O(g) \rightarrow In_2O_3(s) + 3H_2S(g),\\ &\Delta G = 98.4 \text{ kJ/mol at } 200\ ^\circ\text{C}\end{aligned} \quad (1)$$

Due to the high reactivity of radicals, PEALD generally allows the achievement of many chemical reactions that cannot occur with thermal ALD [13,19]. Here $In_2(S,O)_3$ films could be grown while using O_2 plasma as oxygen source. But the growth of pure In_2O_3 films remained unsuccessful. This suggests that the oxygen contained in $In_2(S,O)_3$ films is not generated from single layers of In_2O_3 but rather by exchange reactions as described in the previous section. Indeed, the O_2 plasma can directly react with the film surface and induce an exchange reaction with surface sulfur atoms. Figure 7 presents a scheme of the assumed substitution mechanism at the surface.

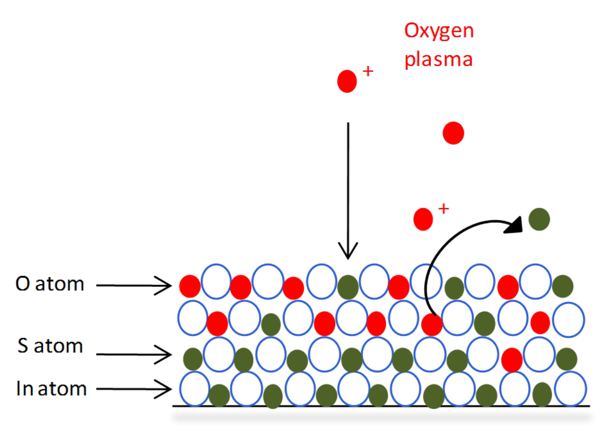

Figure 7: Surface mechanisms during the O_2 plasma pulse.

The following exchange reactions can explain the substitution of S atoms by reactive oxygen species generated in the plasma. Indeed, their free standard enthalpies all have negative values:

$$\begin{aligned}&In_2S_3(s) + 3O^{+\circ}(g) \rightarrow In_2O_3(s) + 3S^{+}(g),\\ &\Delta G = -1413.3 \text{ kJ/mol at } 200\ ^\circ\text{C}\end{aligned} \quad (2)$$

$$\begin{aligned}&In_2S_3(s) + 3O(g) \rightarrow In_2O_3(s) + 3S(g),\\ &\Delta G = -462.3 \text{ kJ/mol at } 200\ ^\circ\text{C}\end{aligned} \quad (3)$$

$$\begin{aligned}&2In_2S_3(s) + 3O_2^{+\circ}(g) \rightarrow 2In_2O_3(s) + 3S^{+}(g) + 3S(g),\\ &\Delta G = -95.8 \text{ kJ/mol at } 200\ ^\circ\text{C}\end{aligned} \quad (4)$$

Thus, when comparing these reactions with the reaction between In_2S_3 and H_2O, it seems that the doping is only favorable when using O_2 plasma as oxygen precursor, because these reactions are all exothermic. This thermochemical analysis and the observation that $In_2(O,S)_3$ films obtained from the two different ALD pulse programs $20\cdot\{In_2S_3\} + 2\cdot\{In_2O_3\}$ and $20\cdot\{In_2S_3\} + 2\cdot O_2$ plasma have similar properties, show the critical role of activated oxygen during the deposition of $In_2(S,O)_3$.

Commonly existing species in oxygen plasmas are atomic oxygen that is created from molecular oxygen dissociation, excited oxygen species at different electronic levels, ionized oxygen or recombined species like O_3 [32,33]. Consequently, exchange reactions between adsorbed oxygen and oxygen species from the gas phase or recombination reactions have to be considered. Marinov et al. studied the interactions between a radiofrequency O_2 plasma and oxide surfaces like TiO_2, SiO_2 and Pyrex [32]. They demonstrated that these materials surfaces are continuously re-structured under O_2 plasma exposure because of the exchange reactions that occur between O atoms in the films and oxygen species of the gas phase. They also reported that reaction products undergo oxidation at the surface and assumed that two surface mechanisms could occur; $O + O \rightarrow O_2$ and $O + O_2 \rightarrow O_3$. Such mechanisms might also occur in our case considering the exchange reactions described in Figure 7 during the first O_2 plasma pulse. Indeed, no match was found between the ratios of In_2O_3 cycles during the deposition of $In_2(S,O)_3$ films and the oxygen content of the films determined by EDX. When the number of In_2O_3 cycles varied from 4.8% to 11.8%, in the same time the oxygen content of the films varied from 68 atom % to 75 atom %. Oxidation mechanisms during deposition process can explain these high differences between the expected values and those measured.

Comparing $In_2(S,O)_3$ films synthesized with and without an $In(acac)_3$ pulse before the O_2 plasma pulse, no significant differences in the band gap values or the atomic ratios of the samples were observed. This confirms that the formation of an In_2O_3 single layer is not required to synthesize $In_2(S,O)_3$ films. These results are in fair agreement with the fact that the growth of pure In_2O_3 remained unsuccessful. Thus, we can assume that only activated oxygen is involved during the deposition of $In_2(S,O)_3$, and In_2S_3 can be considered as an intermediate state for the formation of $In_2(S,O)_3$.

On-going studies focus on a better understanding on the nature of the oxygen species generated by the plasma, their role in oxidizing mechanisms and the reason of the relatively low indium content. One of them could be an excessive adsorption of oxygen in the film and the formation of sulfates. Further studies, in particular by using X-ray photoelectron spectroscopy, are in progress to assess the presence or not of such groups. Experiments will also be performed to study the influence of other oxygen sources such as O_2 alone and O_3.

Conclusion

In this study we reported the atomic layer deposition of $In_2(S,O)_3$ films by using $In(acac)_3$ (acac = acetylacetonate), H_2S, and either H_2O or O_2 plasma as oxygen sources. $In_2(S,O)_3$ films could only be obtained with O_2 plasma as oxygen source, and all attempts to synthesize In_2O_3 remained unsuccessful. Thus, synthesis of $In_2(S,O)_3$ films is likely to occur through an exchange reaction instead of simple mixing of In_2S_3 and In_2O_3 layers. A thermochemical analysis can explain such observations. Indeed, this reaction is endothermic for H_2O and exothermic for O_2 plasma.

With this new synthesis method, the optical band gap of the thin films could be tuned from 2.2 eV to 3.3 eV by increasing the number of O_2 plasma pulses. The high oxygen contents measured in the films (>66 atom %) in comparison to the initial number of In_2O_3 pulses might be explained by the fact that oxidation mechanisms occurred on the film surfaces during the O_2 plasma pulses. Due to the reactivity of the plasma, the film surfaces cannot be considered as a static system but should rather be seen as continually re-structured surfaces. In our future studies, those films will be applied as buffer layer in $Cu(In,Ga)Se_2$ solar cells to investigate their suitability as Cd-free buffer layer for thin film solar cells.

Experimental

In_2S_3 and $In_2(S,O)_3$ thin films were deposited on borosilicate glass and Si(100) substrates in a SUNALE R-200 ALD reactor (Picosun Oy.) with a modified 15 cm × 15 cm square reaction chamber. All samples were deposited performing a total of 2000 growth cycles. The source material for indium was indium acetylacetonate ($In(CH_3COCHCOCH_3)_3$), $In(acac)_3$, (98%, Strem Chemicals). Hydrogen sulfide, H_2S (99.5%, Messer) was used as the sulfur source. Deionized Millipore vapor water and O_2, (99.9995%, Messer) were used as oxygen source. O_2 was introduced in a remote RF plasma generator with Argon (99.9997%, Messer) as carrier gas, and the plasma power was kept at 2600 W. All sources were kept at room temperature while $In(acac)_3$ was heated to 200 °C. The carrying and purge gas was nitrogen with a purity of 99.9999% (Messer). The pressure in the reaction chamber was kept in the range from 1 to 4 mbar.

The thickness of the films was measured using a VEECO DEKTAK 6M profilometer on glass substrates. Thicknesses were determined after creating steps in the films, by masking film parts with chemically resistant tape and dipping the film in nitric acid (45% in water) at room temperature for 60 s. The uncertainty given for the thickness is the standard deviation of six measurements taking into account the uncertainty of the profilometer, the sharpness of steps, the film roughness, and the film inhomogeneity. Transmittance and reflectance spectra were obtained by using a PerkinElmer lambda 900 Spectrophotometer with a PELA-1000 integrating sphere. All optical measurements were performed on borosilicate glass substrates. X-Ray diffraction (XRD) studies were performed under grazing incidence X-ray diffraction conditions with a PANalytical Empyrean diffractometer while using Cu Kα radiation. X-Ray reflectometry analyses were also performed to confirm thickness measurements. Thin film compositions were obtained by using a Magellan 400L scanning electron microscope provided by FEI. It is equipped with an energy dispersive X-ray spectroscopy detector INCASynergy 350. All EDX measurements were carried out on Si(100) substrates and the values reported are atomic percentages (atom %).

Acknowledgements

This work is supported by Ministry of Higher Education and Research via Pierre and Marie Curie University (UPMC, ED390) and EDF. Energy Dispersive X-Ray Specroscopy measurements were performed by S.Borenztajn (CNRS) and Laboratoire de Photonique et Nanostructures (CNRS).

References

1. Jackson, P.; Hariskos, D.; Lotter, E.; Paetel, S.; Wuerz, R.; Menner, R.; Wischmann, W.; Powalla, M. *Prog. Photovoltaics* **2011,** *19,* 894–897. doi:10.1002/pip.1078
2. Empa – CIGS. http://www.empa.ch/plugin/template/empa/*/79143 (accessed July 31, 2013).
3. Çetinörgü, E.; Gümüş, C.; Esen, R. *Thin Solid Films* **2006,** *515,* 1688–1693. doi:10.1016/j.tsf.2006.06.004

4. Nakamura, M.; Kouji, Y.; Chiba, Y.; Hakuma, H.; Kobayashi, T.; Nakada, T. Achievement of 19.7% efficiency with a small-sized Cu(InGa)(SeS)2 solar cells prepared by sulfurization after selenizaion process with Zn-based buffer. 38th IEEE Photovoltaic Specialists Conference, June 3–8, 2012; Austin, TX.
5. Hariskos, D.; Menner, R.; Jackson, P.; Paetel, S.; Witte, W.; Wischmann, W.; Powalla, M.; Bürkert, L.; Kolb, T.; Oertel, M.; Dimmler, B.; Fuchs, B. *Prog. Photovoltaics* **2012,** *20,* 534–542. doi:10.1002/pip.1244
6. Hariskos, D.; Ruckh, M.; Rühle, U.; Walter, T.; Schock, H. W.; Hedström, J.; Stolt, L. *Sol. Energy Mater. Sol. Cells* **1996,** *41–42,* 345–353. doi:10.1016/0927-0248(96)80009-2
7. Zimmermann, U.; Ruth, M.; Edoff, M. In *21st European Photovoltaic Solar Energy Conference: Proceedings of the international conference held in Dresden,* Dresden, Germany, Sept 4–8, 2006; pp 1831–1834.
8. Platzer-Björkman, C.; Hultqvist, A.; Pettersson, J.; Törndahl, T. *Proc. SPIE* **2010,** *7603,* 76030F. doi:10.1117/12.846017
9. Naghavi, N.; Spiering, S.; Powalla, M.; Cavana, B.; Lincot, D. *Prog. Photovoltaics* **2003,** *11,* 437–443. doi:10.1002/pip.508
10. Lindahl, J.; Zimmermann, U.; Szaniawski, P.; Torndahl, T.; Hultqvist, A.; Salome, P.; Platzer-Bjorkman, C.; Edoff, M. *IEEE J. Photovoltaics* **2013,** *3,* 1100–1105. doi:10.1109/JPHOTOV.2013.2256232
11. Genevée, P.; Donsanti, F.; Renou, G.; Lincot, D. *J. Phys. Chem. C* **2011,** *115,* 17197–17205. doi:10.1021/jp203604j
12. Genevée, P.; Donsanti, F.; Renou, G.; Lincot, D. Atomic Layer Deposition of ZnInxSy Buffer Layers For Copper Indium Gallium Diselenide Thin Film Solar Cells. In *26th European Photovoltaic Solar Energy Conference and Exhibition: EU PVSEC Proceedings,* Hamburg, Germany, Sept 5–8, 2011; pp 2428–2431. doi:10.4229/26thEUPVSEC2011-3CO.4.4
13. Miikkulainen, V.; Leskela, M.; Ritala, M.; Puurunen, R. L. *J. Appl. Phys.* **2013,** *113,* 021301. doi:10.1063/1.4757907
14. van Delft, J. A.; Garcia-Alonso, D.; Kessels, W. M. M. *Semicond. Sci. Technol.* **2012,** *27,* 074002. doi:10.1088/0268-1242/27/7/074002
15. Bakke, J. R.; Pickrahn, K. L.; Brennan, T. P.; Bent, S. F. *Nanoscale* **2011,** *3,* 3482–3508. doi:10.1039/c1nr10349k
16. Platzer-Björkman, C.; Törndahl, T.; Abou-Ras, D.; Malmström, J.; Kessler, J.; Stolt, L. *J. Appl. Phys.* **2006,** *100,* 044506. doi:10.1063/1.2222067
17. Barreau, N.; Marsillac, S.; Albertini, D.; Bernede, J. C. *Thin Solid Films* **2002,** *403–404,* 331–334. doi:10.1016/S0040-6090(01)01512-7
18. Maha, M. H. Z.; Bagheri-Mohagheghi, M.-M.; Azimi-Juybari, H.; Shokooh-Saremi, M. *Phys. Scr.* **2012,** *86,* 055701. doi:10.1088/0031-8949/86/05/055701
19. Kim, H. *Thin Solid Films* **2011,** *519,* 6639–6644. doi:10.1016/j.tsf.2011.01.404
20. Asikainen, T.; Ritala, M.; Leskelä, M. *J. Electrochem. Soc.* **1994,** *141,* 3210–3213. doi:10.1149/1.2059303
21. Elam, J. W.; Martinson, A. B. F.; Pellin, M. J.; Hupp, J. T. *Chem. Mater.* **2006,** *18,* 3571–3578. doi:10.1021/cm060754y
22. Elam, J. W.; Libera, J. A.; Hryn, J. N. *ECS Trans.* **2011,** *41,* 147–155. doi:10.1149/1.3633663
23. Lee, D.-J.; Kwon, J.-Y.; Lee, J. I.; Kim, K.-B. *J. Phys. Chem. C* **2011,** *115,* 15384–15389. doi:10.1021/jp2024389
24. Nilsen, O.; Balasundaraprabhu, R.; Monakhov, E. V.; Muthukumarasamy, N.; Fjellvåg, H.; Svensson, B. G. *Thin Solid Films* **2009,** *517,* 6320–6322. doi:10.1016/j.tsf.2009.02.059
25. Asikainen, T.; Ritala, M.; Leskelä, M. *Appl. Surf. Sci.* **1994,** *82–83,* 122–125. doi:10.1016/0169-4332(94)90206-2
26. Yousfi, E. B.; Weinberger, B.; Donsanti, F.; Cowache, P.; Lincot, D. *Thin Solid Films* **2001,** *387,* 29–32. doi:10.1016/S0040-6090(00)01838-1
27. Sterner, J.; Malmström, J.; Stolt, L. *Prog. Photovoltaics* **2005,** *13,* 179–193. doi:10.1002/pip.595
28. Sarkar, S. K.; Kim, J. Y.; Goldstein, D. N.; Neale, N. R.; Zhu, K.; Elliott, C. M.; Frank, A. J.; George, S. M. *J. Phys. Chem. C* **2010,** *114,* 8032–8039. doi:10.1021/jp9086943
29. Hishikawa, Y.; Nakamura, N.; Tsuda, S.; Nakano, S.; Kishi, Y.; Kuwano, Y. *Jpn. J. Appl. Phys.* **1991,** *30,* 1008–1014. doi:10.1143/JJAP.30.1008
30. Liu, D.; Lei, W. W.; Zou, B.; Yu, S. D.; Hao, J.; Wang, K.; Liu, B. B.; Cui, Q. L.; Zou, G. T. *J. Appl. Phys.* **2008,** *104,* 083506. doi:10.1063/1.2999369
31. *HSC Chemistry;* Chemistry Software Ltd, 2013.
32. Marinov, D. Adsorption réactive des molécules et radicaux sur des surfaces sous exposition plasma. Ph.D. Thesis, Ecole Polytechnique X, Palaiseau, France, 2012.
33. Lopaev, D. V.; Malykhin, E. M.; Zyryanov, S. M. *J. Phys. D: Appl. Phys.* **2011,** *44,* 015202. doi:10.1088/0022-3727/44/1/015202

License and Terms

Beilstein Journal
of Nanotechnology

Quantum size effects in TiO_2 thin films grown by atomic layer deposition

Massimo Tallarida*, Chittaranjan Das and Dieter Schmeisser

Full Research Paper

Open Access

Address:
Applied Physics - Sensors, Brandenburg University of Technology
Cottbus–Senftenberg, Konrad-Wachsmann-Allee 17, 03046 Cottbus,
Germany

Email:
Massimo Tallarida* - tallamas@tu-cottbus.de

* Corresponding author

Keywords:
atomic layer deposition (ALD); charge transfer multiplet; covalency;
energy conversion; quantum size effects; titanium dioxide (TiO_2);
water splitting; X-ray absorption spectroscopy (XAS)

Beilstein J. Nanotechnol. **2014,** *5,* 77–82.
doi:10.3762/bjnano.5.7

Received: 30 September 2013
Accepted: 09 January 2014
Published: 22 January 2014

This article is part of the Thematic Series "Energy conversion applications of atomic layer deposition".

Guest Editor: J. Bachmann

Abstract

We study the atomic layer deposition of TiO_2 by means of X-ray absorption spectroscopy. The Ti precursor, titanium isopropoxide, was used in combination with H_2O on Si/SiO_2 substrates that were heated at 200 °C. The low growth rate (0.15 Å/cycle) and the in situ characterization permitted to follow changes in the electronic structure of TiO_2 in the sub-nanometer range, which are influenced by quantum size effects. The modified electronic properties may play an important role in charge carrier transport and separation, and increase the efficiency of energy conversion systems.

Introduction

Titanium dioxide (TiO_2) is an important material for the photoelectrolysis of water [1] and for many other photocatalytic reactions [2]. Its effective conversion of solar light, although limited by the band gap being too large, has been demonstrated in many systems [3]. Atomic layer deposition (ALD) is a chemical method to grow homogeneous thin films in an atomically controlled mode, which allows for the conformal coating of complex structures with precise thickness and a high degree of purity [4]. The growth of TiO_2 by ALD is a well-studied process and has been recently reviewed [5]. Charge carrier transport and separation, which strongly depend on interface and surface properties [6,7], are among the most important aspects of energy conversion processes. Therefore the further implementation of efficient photo-electrochemical (PEC) systems is inherently related to the outstanding quality of ALD films, i.e., high purity and homogeneity, and perfect control of thickness in conformal films. It has been shown that very thin films of TiO_2 may indeed improve PEC performances [8,9].

Recently, TiO_2 nanoparticles (NPs) with an average diameter of 2 nm showed quantum size effects on unoccupied states [10], which involved the hybridization of Ti 3d and Ti 4s orbitals with O 2p orbitals in covalent bonds. The conformal growth of ALD gives the possibility of having homogeneous films below

2 nm thickness and allows for the investigation of similar quantum size effects in TiO_2 thin films. In this case interface effects, as those observed in TiO_2 ALD films grown on SnO_2:F [11], could also become important. We performed the characterization of ALD films by using mostly X-ray absorption spectroscopy (XAS). Synchrotron radiation (SR) based photoemission spectroscopy (PES) was also used to measure Ti 2p, O 1s and Si 2p core level spectra to determine the films thickness. Further, in order to study the TiO_2 thin films in the sub-nanometer range, it was decisive to perform the spectroscopic characterization in an in situ ALD system, where the freshly deposited thin films were transported into the measurement chamber without breaking the vacuum [12,13].

The XAS of 3d transition metal (TM) oxides at the O-K and the TM-$L_{2,3}$ edges is a very important tool to determine their electronic and structural properties. Although the detailed interpretation of XAS measurements is very complex and not yet completely achieved, it was shown that rutile, anatase and amorphous TiO_2 films, as well as quantum-confined TiO_2 nanostructures exhibit distinct features at both the O-K and the TM-$L_{2,3}$ edges [10,14,15]. Here, we compare our XAS results with previous measurements in order to determine how the degree of covalency of the TiO_2 thin films can be evaluated and observe that ALD films of TiO_2 show quantum size effects, which influence their electronic properties.

Results and Discussion

Ti-$L_{2,3}$ edge of TiO_2 thin films

Thermal ALD of TiO_2 with titanium(IV) isopropoxide (TTIP) and H_2O at 200 °C proceeds very slowly [16], with a growth rate of about 0.15 Å/cycle. Indeed, the XAS spectra at the Ti-$L_{2,3}$ edge in Figure 1 show very small changes with increasing number of ALD cycles. Moreover, various spectral features typical of either anatase or rutile TiO_2 are absent in the XAS spectra of the ALD films [17]. These crystalline phases show a split structure for feature A; a strong and sharp peak B, and distinct pre-preak features PP. Features A′ and B′ are sharper and well separated in the crystalline phases, too. Moreover, in the crystalline phases the satellite features S_1 and S_2 are stronger and exhibit a fine structure. Our spectra are, instead, in agreement with those obtained by Kucheyev et al. [14] for amorphous TiO_2, in which feature A is a broad peak, B is very small, and PP are not well developed. Similar spectra were also observed in very thin TiO_2 films that were grown by reactive evaporation in oxygen atmosphere at room temperature on SiO_2 [18], Al_2O_3 [19] and MgO [20]. There, XAS spectra at the Ti-$L_{2,3}$ absorption edge were analyzed within the charge-transfer multiplet (CTM) model. Within the CTM theory, the spectral features observed for very thin TiO_2 films were addressed to a decreased ligand-field at TiO_2/substrate interfaces, which was found to be increasingly important when moving from the MgO substrate to SiO_2 [21]. Instead, Krüger used a first-principles multichannel multiple-scattering approach to show that the absence of a split structure in feature A should be addressed to the loss of long-range order on a length scale of 1 nm [22]. Recently, Preda et al. showed for NiO/SiO_2 that in addition to the lost of long-range order, distortion at the interface induce changes in the XAS spectra [23]. It should be noticed that Ti-$L_{2,3}$ spectra with typical features of anatase and rutile TiO_2 were obtained with our ALD system when TTIP was used in connection with O_2-plasma instead of water [17].

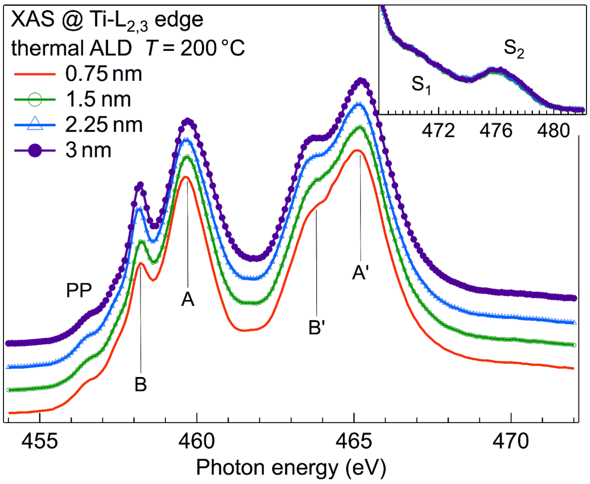

Figure 1: XAS at the Ti-$L_{2,3}$ edge measured for TiO_2 films with thicknesses of 0.75 nm, 1.5 nm, 2.25 nm and 3 nm. Spectra were normalized to the same intensity at 485 eV and vertically offset.

O-K edge of TiO_2 thin films

Differently from the Ti-$L_{2,3}$ spectra, the O-K XAS edge is usually interpreted with the density of unoccupied states of O 2p, as multiplet structures that originate from the overlap of initial and final state wave functions are considered to be negligible [24]. In this case the XAS at O-K edge gives direct information about the hybridization of O 2p with Ti orbitals [24]. The XAS spectra (Figure 2) show mainly two features, namely the double peak C between 530 eV and 535 eV, and the broad feature D extending between 535 eV and 550 eV. The XAS spectra at the O-K edge exhibit evident changes of the shape of the lines with increasing TiO_2 thickness. In fact, the separation between the two peaks that form feature C, the ratio between feature C and feature D, as well as the shape of the broad feature D vary appreciably after each new deposition.

The shape of feature D is influenced by the presence of SiO_2 in the substrate, which contributes to the O-K spectra as shown in Figure 2. To remove the contribution of SiO_2 to the O-K edge of the growing TiO_2 film, we subtracted the former from each

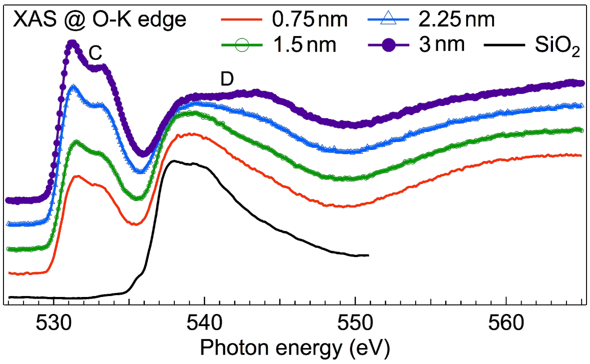

Figure 2: XAS at O-K edge measured for TiO_2 films with thicknesses of 0.75 nm, 1.5 nm, 2.25 nm and 3 nm. The XAS of native SiO_2 is also shown as reference. Spectra were normalized to the same intensity at 580 eV and vertically offset.

XAS spectrum, as shown for the 0.75 nm and 3 nm films in Figure 3. To this aim we estimated the weight of the SiO_2 component in the total spectra considering an exponential attenuation. As mean probing depth (MPD) we used the estimation made by Abbate et al. [25], who found that the O-K edges have a MPD of 1.9 nm. For the spectrum of the 0.75 nm film, we subtracted the SiO_2 substrate spectrum multiplied by 0.68, and for the 3 nm film the same spectrum multiplied by 0.2. Our subtraction procedure is validated by the fact that in a previous experiment [26], in which we deposited HfO_2 on SiO_2 and characterized with XAS cycle by cycle, we could observe that the O-K XAS of SiO_2 does not change during the deposition of HfO_2.

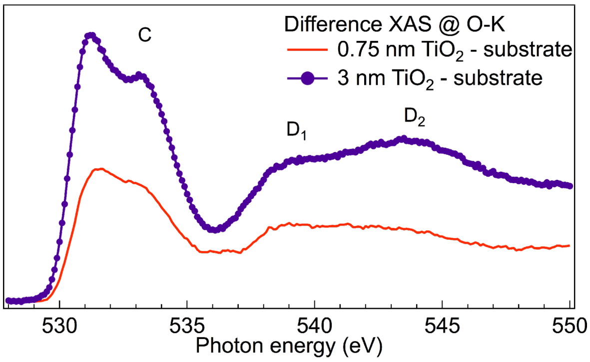

Figure 3: XAS difference spectra. The contribution of SiO_2 to the XAS at the O-K edge was subtracted from the measured spectra. Feature D of Figure 2 is now described by two features: D_1 and D_2.

From the difference spectra the different intensity of peak C and the different shape of feature D, with the latter being formed by two regions, defined as D_1 and D_2, become evident. For the 0.75 nm film, the D_1 contribution is stronger than D_2 and very broad, while in the 3 nm thick film, the ratio is inversed, D_1 becomes sharp and D_2 follows the increase of feature C. Finally, the line shape of the 3 nm film is very similar to that observed in anatase TiO_2 [10]. Vayssieres et al. found that quantum size effects in TiO_2 NPs with an average diameter of 2 nm induce a change in the character of the conduction band orbital with a strengthening of the Ti 4s/O 2p hybridization and a simultaneous weakening of the Ti 3d/O 2p hybridization [10]. This was concluded from the observation that the doublet at 530–535 eV (called feature C here) in TiO_2 NPs was weaker relative to the broad feature in the region 535–550 eV (feature D). The broad region is usually addressed to O 2p states hybridized with Ti 4s and Ti 4p states, and its broadness of about 15 eV is considered to be an indication of strong covalent character of the bonds in TiO_2 polymorphs, while feature C is usually addressed to Ti 3d/O 2p hybridized states [10]. Although we also observe the increase of feature C and the line shape change of feature D, we additionally notice that the two main structures of feature D (D_1 and D_2) in Figure 3 behave differently. This observation establishes an empirical correlation between feature C and the region D_2 that needs an explanation. Theoretical calculations performed by Wu et al. [27] in the framework of the full multiple scattering theory and the tight-binding linear muffin-tin orbital band-structure method showed the presence of the higher energy tail only for large clusters, which is indicative of a long-range order. On the other hand, the calculation of unoccupied density of states performed by Vayssieres et al. [10] indicate the presence of Ti 4s/O 2p states over a large energy range. Our spectrum of the 0.75 nm film agrees with the calculation of Vayssieres especially in the region of peak D_1, while peak D_2 does not have any visible connection to the calculation of small clusters. This could be an indication that peak D_2 originates not only from Ti 4s/O 2p hybridized states.

A detailed view of feature C of the four XAS spectra (Figure 4) shows the change of the fine structure in this region when the TiO_2 film thickness increases from 1.5 nm to 2.25 nm. As mentioned above, the origin of this feature was attributed to hybridized Ti 3d/O 2p states, for which the two peaks appear because the Ti 3d orbital is split into t_{2g} and e_g bands by the ligand-field. The shape of 0.75 nm and 1.5 nm TiO_2 films compares very well with that found by Kronawitter et al. [11] at the interface between TiO_2 and SnO_2:F and were attributed to modified electronic properties of TiO_2. In that case, TiO_2 was grown by ALD using $TiCl_4$ and H_2O at 150 °C. This shows that the interface formation is similar for these two different ALD-precursors and for different substrates. Kronawitter et al. addressed the changes at the O-K edge to a variation of the ligand-field at the interface, due to structural distortion and to a weaker Ti 3d/O 2p hybridization [11]. We further notice that the decrease of Ti 3d/O 2p hybridization in thinner films pairs up with the increase of Ti 4s/O 2p hybridization, and can be explained by the larger spatial extension of Ti 4s wave functions compared to Ti 3d [10]. These considerations attribute the spectral properties of the TiO_2 thin films mostly to changes in covalency.

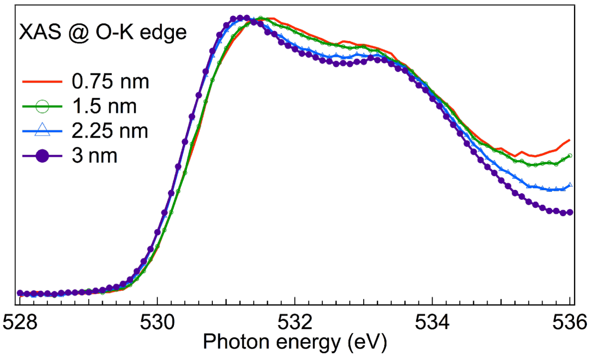

Figure 4: Detailed view of feature C. The spectra were normalized in order to distinguish line-shape changes.

Covalency in TiO_2 thin films

Covalency, i.e., the degree of orbital overlap, in TM oxides is a particularly important property for understanding the efficiency of photo-electrodes, as it influences the charge carrier transport mechanism. Covalent materials are desirable because separation and transport of electrons and holes are supported, while the recombination probability of photo-excited carriers is decreased. A change in the covalent contribution to the chemical bond of one material means modified transport properties, and different PEC efficiency [28]. The stronger Ti 4s/O 2p hybridization observed in TiO_2 thin films causes a larger bandwidth of conduction band states, increases the delocalization of O 2p states, and improves the charge carrier transport. We recently used our TiO_2 films grown by ALD on Fe_2O_3 in order to increase the photoactivated hydrophilic and photocatalytic behavior of Fe oxides. There, it was observed that TiO_2 thin films and their interface with Fe_2O_3 substrates result in an improved charge carrier separation and a decrease of recombination [16] that could be ascribed to the electronic properties of the TiO_2 thin films.

It is important to understand how changes of the line shape (number, position and intensity of peaks and larger features) in XAS can be related to covalency, and whether these features can be used to estimate variations in PEC efficiency. Determination of the covalent character in a TM–O bond through electronic spectroscopy has been discussed for both XPS [29] and XAS [30]. Although, the O-K edge gives information about covalency by considering the width of broad features and by the intensity of feature C, in the case of Ti-$L_{2,3}$ spectra this interpretation is more difficult and often overlooked because covalency in 3d TM-$L_{2,3}$ spectra goes beyond the (atomic) multiplet model used for the analysis. To include covalency in that model, charge transfer (CT) (from oxygen to TM) is usually adopted in order to include the atomic configurations of the TM with an extra charge density that results from hybridization. For example the purely $3d^0$ atomic multiplet of TiO_2 is substituted by a combination of configurations, in which $3d^1\underline{L}$ and $3d^2\underline{LL'}$ CT are partially allowed. However, the atomic nature of the multiplet is still maintained in the calculations [31]. In this way, the influence of covalency in TM-$L_{2,3}$ spectra is mostly related to the presence of peculiar features that are attributed to the charge transfer and not to the relative intensity of the major multiplet features. Instead, these are usually explained with the strength of the ligand-field. The multiplet features are obtained by the transition probabilities to the TM 3d atomic orbital. Due to the strong core–hole effect, the intensity of the various multiplet transitions is weighted by the statistical occupation of the atomic orbital in the initial and final state configurations. Upon changing the ligand-field the energy separation of the d-states (and their statistical occupation) is also changed and the intensity of the main features (obtained from the sum of many multiplets) changes accordingly [31]. In general, a stronger crystal field decreases the intensity of the feature at higher energies and increases the feature at lower energies. Within this model Soriano et al. [21] ascribed the Ti-$L_{2,3}$ XAS of very thin TiO_2 films to the interaction with the substrate and the decreased ligand-field, which eventually modifies the Ti 3d/O 2p hybridization (defined by the pdσ parameter) because of the modified energy distribution of d-orbitals.

Another way to consider covalency in the framework of atomic multiplets is related to the calculation of Slater integrals. This is usually done by considering isolated ions, by using the one-electron Hartree–Fock method and then rescaled to 80% of their value to account for intra-atomic correlation effects. When a covalent bond is formed, the shape and radial distribution of d-orbitals tend to readjust because of the nephelauxetic effect (typical in TM complexes) [32]. The spatial modification of d-orbitals induces a reduction of the Slater integrals in the covalent bond atoms compared to their ionic values. The reduction of Slater integrals produces a similar effect as that of ligand-field increase, i.e., an intensity increase of the lower energy multiplet transitions and a decrease of the higher energy features [33]. However, the reduction of Slater integrals does not need a structural distortion but only a different charge distribution around covalent bond atoms. From this observation it becomes clear that the same line shape can be simulated within the same theory framework (the charge-transfer multiplet) upon varying two different parameters, i.e., Slater integrals or ligand-field, which have a different physical meaning. While Soriano et al. [21] considered only the changes of ligand-field and pdσ at the TiO_2 interface with either MgO, Al_2O_3 or SiO_2, attributing the line shape of the Ti-$L_{2,3}$ spectra to structural modifications of TiO_2, changing the Slater integrals would have induced to attribute the line-shape variations to a changed Ti 3d/O 2p hybridization (and covalency) in very thin films without considering any ligand-field variation, i.e., no structural distortion at the interface. We think that calculations made by varying only the ligand-field parameter could have overestimated its importance, although we agree that at the interface a certain degree of structural distortion should be present. The observed decreased Ti 3d/O 2p (and the increased Ti 4s/O 2p) hybridization at the O-K edge reconciles well with the observed Ti-$L_{2,3}$ spectra in our ALD films when a change of covalency is considered, and calculations with reduced Slater integrals are made maintaining the same or a slightly different ligand-field parameter. This also agrees with the observation that the split of feature A at the Ti-$L_{2,3}$ edge appears in multiple scattering calculations only for large clusters [22], i.e., for systems in which the wavefunction overlap becomes more extended.

Conclusion

We have shown a detailed characterization of TiO_2 ALD films with thickness increasing from 0.75 nm to 3 nm by using XAS at both the Ti-$L_{2,3}$ and O-K edges. The use of ALD films permits to have reproducible films with well-defined thickness, and allows a comparison with energy conversion systems, in which thin TiO_2 films are used to increase efficiency. We deduce that thin TiO_2 films exhibit peculiar electronic properties, which should be ascribed to quantum size effects. These influence the covalency in TiO_2 by favouring a delocalization of conduction band states.

Experimental

Atomic layer deposition (ALD) of TiO_2 was performed in an ultra-high-vacuum (UHV)-compatible reactor attached to the measurement chamber through a plate valve [12]. The Ti precursor (TTIP) pulse was 4 s, followed by two N_2 purging pulses, each of 0.5 s, performed just after the Ti precursor and after 5 s. The H_2O pulse was 0.5 s, followed again by two N_2 purge pulses. Between the cycles we waited 10 s, in order to have a pressure of 10^{-6} mbar in the ALD chamber before starting the next ALD cycle. The sample was heated inductively to 200 °C. On one Si sample, covered with native SiO_2, we deposited a TiO_2 film with increasing thickness, obtained after 50, 100, 150 and 200 ALD cycles. The thickness of the ALD film was 0.75 nm, 1.5 nm, 2.25 nm, and 3 nm, respectively.

Synchrotron radiation was obtained at the U49/2-PGM2 beamline at the BESSY–II synchrotron radiation facility within the Helmholtz-Zentrum Berlin [34]. X-ray photons produced by the U49 undulator were monochromatized by a planar grating monochromator with a resolution of the order of $\Delta E/E \approx 10^{-4}$. X-ray absorption spectroscopy (XAS) was measured simultaneously while using both total electron yield (TEY) and partial electron yield (PEY). The former was measured through the drain current on the sample, while PEY (and PES) was measured using a PHOIBOS-150 electron analyzer from Specs GmbH, equipped with a 1D delay line detector. The base pressure of the measurement chamber was 5×10^{-10} mbar.

Acknowledgements

The authors acknowledge the BESSY-II staff and M. Städter for support during beamtime. Financial support was provided by the Deutsche Forschungsgemeinschaft (DFG) with the project SCHM 745/31-1, and by the German Ministry of Research and Education (BMBF) with the grant 03IN2V4A.

References

1. Fujishima, A.; Honda, K. *Nature* **1972,** *238,* 37–38. doi:10.1038/238037a0
2. Linsebigler, A. L.; Lu, G.; Yates, J. T., Jr. *Chem. Rev.* **1995,** *95,* 735–758. doi:10.1021/cr00035a013
3. Hashimoto, K.; Irie, H.; Fujishima, A. *Jpn. J. Appl. Phys.* **2005,** *44,* 8269–8285. doi:10.1143/JJAP.44.8269
4. Leskelä, M.; Ritala, M. *Thin Solid Films* **2002,** *409,* 138–146. doi:10.1016/S0040-6090(02)00117-7
5. Pore, V. Atomic Layer Deposition and Photocatalytic Properties of Titanium Dioxide Thin Films. Ph.D. Thesis, Helsinki University, Helsinki, Finland, 2010.
6. Liao, P.; Carter, E. A. *Chem. Soc. Rev.* **2013,** *42,* 2401–2422. doi:10.1039/c2cs35267b
7. Li, Z.; Luo, W.; Zhang, M.; Feng, J.; Zou, Z. *Energy Environ. Sci.* **2013,** *6,* 347–370. doi:10.1039/c2ee22618a
8. Paracchino, A.; Laporte, V.; Sivula, K.; Grätzel, M.; Thimsen, E. *Nat. Mater.* **2011,** *10,* 456–461. doi:10.1038/nmat3017
9. Chen, Y. W.; Prange, J. D.; Dühnen, S.; Park, Y.; Gunji, M.; Chidsey, C. E. D.; McIntyre, P. C. *Nat. Mater.* **2011,** *10,* 539–544. doi:10.1038/nmat3047
10. Vayssieres, L.; Persson, C.; Guo, J.-H. *Appl. Phys. Lett.* **2011,** *99,* 183101. doi:10.1063/1.3657147
11. Kronawitter, C. X.; Kapilashrami, M.; Bakke, J. R.; Bent, S. F.; Chuang, C.-H.; Pong, W.-F.; Guo, J.; Vayssieres, L.; Mao, S. S. *Phys. Rev. B* **2012,** *85,* 125109. doi:10.1103/PhysRevB.85.125109
12. Tallarida, M.; Weisheit, M.; Kolanek, K.; Michling, M.; Engelmann, H. J.; Schmeisser, D. *J. Nanopart. Res.* **2011,** *13,* 5975–5983. doi:10.1007/s11051-011-0319-x
13. Tallarida, M.; Schmeisser, D. *Semicond. Sci. Technol.* **2012,** *27,* 074010. doi:10.1088/0268-1242/27/7/074010
14. Kucheyev, S. O.; van Buuren, T.; Baumann, T. F.; Satcher, J. H., Jr.; Willey, T. M.; Meulenberg, R. W.; Felter, T. E.; Poco, J. F.; Gammon, S. A.; Terminello, L. J. *Phys. Rev. B* **2004,** *69,* 245102. doi:10.1103/PhysRevB.69.245102
15. Gago, R.; Redondo-Cubero, A.; Vinnichenko, M.; Vázquez, L. *Chem. Phys. Lett.* **2011,** *511,* 367–371. doi:10.1016/j.cplett.2011.06.061

16. Barreca, D.; Carraro, G.; Gasparotto, A.; Maccato, C.; Rossi, F.; Salviati, G.; Tallarida, M.; Das, C.; Fresno, F.; Korte, D.; Štangar, U. L.; Franko, M.; Schmeisser, D. *ACS Appl. Mater. Interfaces* **2013,** *5,* 7130–7138. doi:10.1021/am401475g
17. Tallarida, M.; Friedrich, D.; Städter, M.; Michling, M.; Schmeisser, D. *J. Nanosci. Nanotechnol.* **2011,** *11,* 8049–8053. doi:10.1166/jnn.2011.5102
18. Soriano, L.; Fuentes, G. G.; Quirós, C.; Trigo, J. F.; Sanz, J. M.; Bressler, P. R.; González-Elipe, A. R. *Langmuir* **2000,** *16,* 7066–7069. doi:10.1021/la000330x
19. Sánchez-Agudo, M.; Soriano, L.; Quirós, C.; Avila, J.; Sanz, J. *Surf. Sci.* **2001,** *482,* 470–475. doi:10.1016/S0039-6028(00)01048-7
20. Sánchez-Agudo, M.; Soriano, L.; Quirós, C.; Roca, L.; Pérez-Dieste, V.; Sanz, J. M. *Surf. Sci.* **2002,** *507–510,* 672–677. doi:10.1016/S0039-6028(02)01334-1
21. Soriano, L.; Sánchez-Agudo, M.; Mossanek, R. J. O.; Abbate, M.; Fuentes, G. G.; Bressler, P. R.; Alvarez, L.; Méndez, J.; Gutiérrez, A.; Sanz, J. M. *Surf. Sci.* **2011,** *605,* 539–544. doi:10.1016/j.susc.2010.12.013
22. Krüger, P. *Phys. Rev. B* **2010,** *81,* 125121. doi:10.1103/PhysRevB.81.125121
23. Preda, I.; Soriano, L.; Díaz-Fernández, D.; Domínguez-Cañizares, G.; Gutiérrez, A.; Castro, G. R.; Chaboy, J. *J. Synchrotron Radiat.* **2013,** *20,* 635–640. doi:10.1107/S0909049513012417
24. de Groot, F. M. F.; Grioni, M.; Fuggle, J. C.; Ghijsen, J.; Sawatzky, G. A.; Petersen, H. *Phys. Rev. B* **1989,** *40,* 5715–5723. doi:10.1103/PhysRevB.40.5715
25. Abbate, M.; Goedkoop, J. B.; de Groot, F. M. F.; Grioni, M.; Fuggle, J. C.; Hofmann, S.; Petersen, H.; Sacchi, M. *Surf. Interface Anal.* **1992,** *18,* 65–69. doi:10.1002/sia.740180111
26. Tallarida, M.; Karavaev, K.; Schmeisser, D. J. *Vac. Sci. Technol., B* **2009,** *27,* 300. doi:10.1116/1.3021023
27. Wu, Z. Y.; Ouvrard, G.; Gressier, P.; Natoli, C. R. *Phys. Rev. B* **1997,** *55,* 10382–10391. doi:10.1103/PhysRevB.55.10382
28. Liao, P.; Toroker, M. C.; Carter, E. A. *Nano Lett.* **2011,** *11,* 1775–1781. doi:10.1021/nl200356n
29. Bagus, P. S.; Ilton, E. S. *Phys. Rev. B* **2006,** *73,* 155110. doi:10.1103/PhysRevB.73.155110
30. Minasian, S. G.; Keith, J. M.; Batista, E. R.; Boland, K. S.; Bradley, J. A.; Daly, S. R.; Kozimor, S. A.; Lukens, W. W.; Martin, R. L.; Nordlund, D.; Seidler, G. T.; Shuh, D. K.; Sokaras, D.; Tyliszczak, T.; Wagner, G. L.; Weng, T.-C.; Yang, P. *J. Am. Chem. Soc.* **2013,** *135,* 1864–1871. doi:10.1021/ja310223b
31. de Groot, F. M. F. *J. Electron Spectrosc. Relat. Phenom.* **1994,** *67,* 529–622. doi:10.1016/0368-2048(93)02041-J
32. Jørgensen, C. K. *Orbitals in Atoms and Molecules;* Academic Press: London, 1962.
33. Crocombette, J. P.; Jollet, F. *J. Phys.: Condens. Matter* **1996,** *8,* 5253. doi:10.1088/0953-8984/8/28/009
34. Schmeisser, D.; Hoffmann, P.; Beuckert, G. Electronic Properties of the Interface Formed by Pr_2O_3 Growth on Si(001), Si(111) and SiC(0001) Surfaces. In *Materials for Information Technology;* Zschech, E.; Whelan, C.; Mikolajick, T., Eds.; Springer: New York, 2005; pp 449–460. doi:10.1007/1-84628-235-7_36

License and Terms

Beilstein Journal
of Nanotechnology

3D-nanoarchitectured Pd/Ni catalysts prepared by atomic layer deposition for the electrooxidation of formic acid

Loïc Assaud[1], Evans Monyoncho[2], Kristina Pitzschel[1], Anis Allagui[2],
Matthieu Petit[1], Margrit Hanbücken[1], Elena A. Baranova*[2]
and Lionel Santinacci*[1]

Full Research Paper

Open Access

Address:
[1]Aix-Marseille Université, CNRS, CINaM UMR 7325, 13288, Marseille, France and [2]Department of Chemical and Biological Engineering, Center for Catalysis Research and Innovation, University of Ottawa, 161 Louis-Pasteur St., Ottawa, ON, K1N 6N5, Canada

Email:
Elena A. Baranova* - elena.baranova@uottawa.ca;
Lionel Santinacci* - lionel.santinacci@univ-amu.fr

* Corresponding author

Keywords:
anodic aluminum oxide; atomic layer deposition (ALD); direct formic acid fuel cells; electrooxidation; nanostructured catalysts; Pd/Ni

Beilstein J. Nanotechnol. **2014,** *5,* 162–172.
doi:10.3762/bjnano.5.16

Received: 30 September 2013
Accepted: 14 January 2014
Published: 12 February 2014

This article is part of the Thematic Series "Energy conversion applications of atomic layer deposition".

Guest Editor: J. Bachmann

Abstract

Three-dimensionally (3D) nanoarchitectured palladium/nickel (Pd/Ni) catalysts, which were prepared by atomic layer deposition (ALD) on high-aspect-ratio nanoporous alumina templates are investigated with regard to the electrooxidation of formic acid in an acidic medium (0.5 M H_2SO_4). Both deposition processes, Ni and Pd, with various mass content ratios have been continuously monitored by using a quartz crystal microbalance. The morphology of the Pd/Ni systems has been studied by electron microscopy and shows a homogeneous deposition of granularly structured Pd onto the Ni substrate. X-ray diffraction analysis performed on Ni and NiO substrates revealed an amorphous structure, while the Pd coating crystallized into a fcc lattice with a preferential orientation along the [220]-direction. Surface chemistry analysis by X-ray photoelectron spectroscopy showed both metallic and oxide contributions for the Ni and Pd deposits. Cyclic voltammetry of the Pd/Ni nanocatalysts revealed that the electrooxidation of HCOOH proceeds through the direct dehydrogenation mechanism with the formation of active intermediates. High catalytic activities are measured for low masses of Pd coatings that were generated by a low number of ALD cycles, probably because of the cluster size effect, electronic interactions between Pd and Ni, or diffusion effects.

Introduction

Over the last decade, the miniaturization of fuel cells for the fast expanding market of portable devices has become a challenging research topic. Direct formic acid fuel cell (DFAFC) systems as electrochemical power sources have many advantages such as the low-toxicity, unlike methanol, the low cost, and the low fuel crossover at a high power density [1-3]. Palladium is a good candidate to catalyze the electrooxidation of formic acid thanks to its good stability at low pH and its high activity [4-8]. The electrooxidation of HCOOH on Pd results in the formation of CO_2 and protons [7], which is a direct dehydrogenation pathway through the formation of active intermediates without the generation of poisonous CO species (Scheme 1).

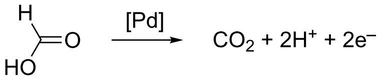

Scheme 1: Pd-catalyzed electrooxidation of HCOOH on Pd surfaces.

Despite the advantages of Pd catalysts for the electrooxidation of formic acid, the activity is still not satisfactory enough for commercial applications and more importantly, Pd tends to dissolve and deactivate quickly by the impurities present in the electrolyte [9]. Additionally, reducing the noble metal loading by alloying Pd with a second cheap transition metal is essential for a viable development of DFAFCs. In recent studies, several metals such as Cu, Ni, Fe or Pt alloyed with Pd have been tested [10-13] for the electrooxidation reaction of HCOOH, and have shown a significant increase of the catalytic activity when compared to pure Pd. Amongst them, the Pd/Ni bimetallic system has shown very promising results due to the favorable electronic effects that Ni brings into the system.

It is also well-known that decreasing the size of the active particles and thus increasing the electro-active surface area of the catalyst are interesting ways to improve the electrooxidation of HCOOH. Nanostructured substrates such as nanowires, nanorods, nanopores or nanotubes have thus been investigated to enhance the catalytic efficiency and to reduce the costs [14]. On the other hand, the physical, chemical and electrochemical properties of the nanostructures are highly correlated with the technique of fabrication. Among the numerous methods that have been recently explored, the use of atomic layer deposition (ALD) to fabricate and/or functionalize nanostructures appears to be very promising. Catalysts grown by ALD often demonstrated similar or enhanced properties as compared to those grown by conventional methods, such as impregnation, ion-exchange, and deposition–precipitation [15,16]. ALD has initially been used to produce oxide layers to support the catalysts [17], but two additional approaches have been recently proposed: ALD is either used to grow metallic clusters or it is applied to protect those metallic clusters with an ultrathin metal oxide layer (see, e.g., the reviews [18-20]). This deposition method is particularly interesting for electrocatalysis because it allows an accurate control of both growth rate and composition of the catalyst, and it provides a high coverage of high aspect ratio nanostructures [21-23]. It is therefore possible to precisely design catalysts onto nanoarchitectured supports that exhibit enhanced abilities for fuel cell applications [24,25].

As previously proposed [26], nanoporous anodic aluminum oxide (AAO) has been used as nanostructured support for the Pd catalysts. The AAO membranes are attractive because they exhibit a high specific surface area and the pore diameter and length can be tailored easily [27,28]. In this study, the usual two-step anodization process shown in Figure 1a–e, has been used to grow well-ordered porous structures. Ni and Pd are then successively deposited into the templates by ALD. The alumina membranes are firstly coated by NiO that is reduced to metallic Ni by annealing under H_2 atmosphere [29,30] (Figure 1f). The Pd clusters are then deposited directly onto the Ni films (Figure 1g). Both NiO and Pd deposition processes have been monitored by quartz crystal microbalance (QCM). The morphology, the chemical composition and the crystalline structures have been investigated by scanning and transmission electron microscopy (SEM and TEM) and atomic force microscopy (AFM), X-ray photoelectron spectroscopy (XPS) and X-ray diffraction (XRD), respectively. The electrocatalytic activity of the Pd/Ni systems, which were deposited on three-dimensional alumina membranes with various mass content ratios, for the electrooxidation of formic acid in acidic solution has been studied by cyclic voltammetry (CV).

Results and Discussion

Nickel deposition

Since ALD processes have been developed mainly for metal oxide and nitride thin films, metal depositions have been hampered mostly by the lack of relevant and stable precursors [31]. Although a new class of precursors that facilitates the direct metal deposition, has recently been proposed [32], several metals are often grown through a two-step process: (i) deposition of the metallic oxide and (ii) subsequent reduction (see, e.g., [29,30]). Metallic Ni is therefore grown by using such an approach [33,34]: the deposition of NiO is carried out from nickelocene ($NiCp_2$) and O_3 precursors and the reduction of this oxide film to metallic Ni is obtained by a reductive annealing process under H_2 atmosphere. The relative mass, *m*, gain and loss have been monitored during the process by QCM and are plotted in Figure 2a. A regular cyclic variation of the mass vs

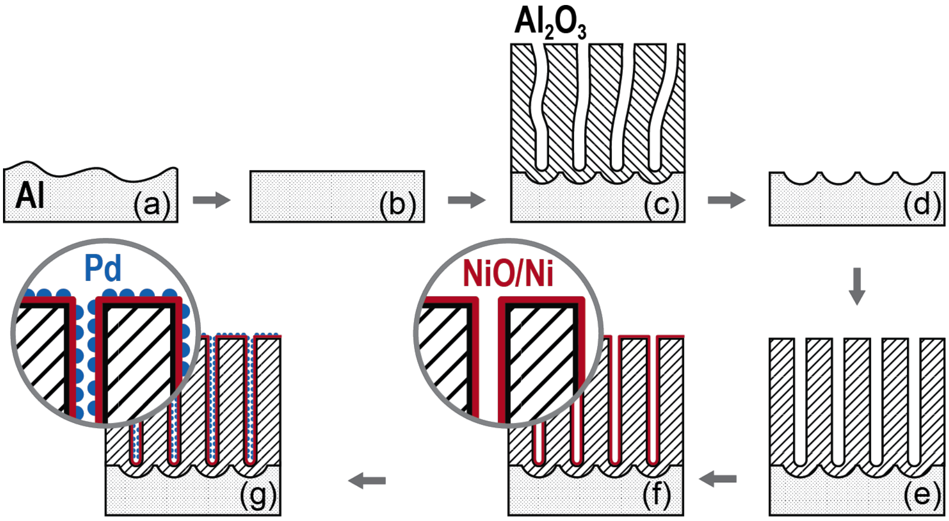

Figure 1: Schematic description of the anodic alumina template fabrication and successive functionalization. (a) Initial Al disc, (b) electropolished Al disc, (c) anodic Al_2O_3 porous layer, (d) pre-ordered Al disc after removal of the AAO sacrificial layer, (e) self-ordered AAO membrane, (f) Ni/NiO film deposited by ALD and reduced by annealing post treatment, (g) Pd cluster layer grown by ALD.

the number of ALD cycles is observed with an overall linear evolution, which is typical for an ALD process with constant growth rate. An enlarged view of one cycle presented in Figure 2b shows in detail the process during the four successive steps of the NiO ALD sequence. The QCM measurements indicate that the exposure and purging duration are optimized for both $NiCp_2$ and O_3 pulses. The mass variations are indeed reaching a plateau at the end of the exposure and purging stages. After the short $NiCp_2$ pulse (green period on the far left of Figure 2b), the mass increases progressively up to a maximum (Δm_1) during the exposure phase (S1). Then a mass loss is measured during the purging phase (S2). A similar trend is observed after the O_3 pulse: a mass increase (Δm_2) is measured during the exposure time (S3) followed by a total mass loss during the purging phase (S4).

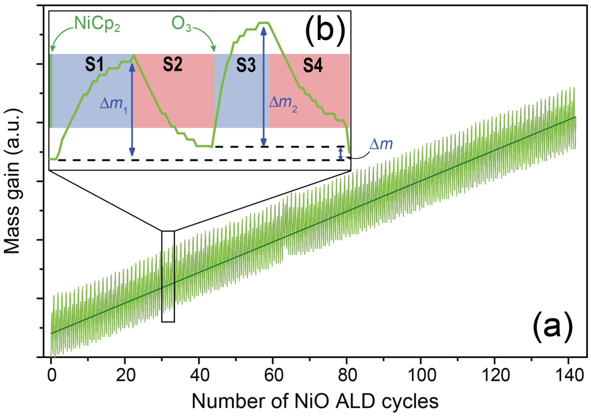

Figure 2: (a) In situ QCM measurement of the NiO mass gain during the ALD process. (b) Enlarged view of the mass gain for one ALD cycle. Δm corresponds to the net mass increase after the ALD cycle.

It is difficult to correlate the mass gain and loss measured by the QCM with a reaction mechanism. Thus few data can be found in literature about such chemical processes. However, Martinson et al. proposed a detailed investigation of the Fe_2O_3 formation from $FeCp_2$ and O_3 precursors by using quadrupole mass spectrometry (QMS) [35]. Since the precursors used for this deposition are close to those employed in the present study, the Martinson mechanism may be adapted to the deposition of NiO using $NiCp_2$ and O_3. Therefore, the S1 period could be ascribed to the adsorption of $NiCp_2$ on the whole surface, which after reaction on the active sites yields a –NiCp group on the surface and one cyclopentadiene molecule is released. Note that Martinson et al. have also detected cyclopentadione as a byproduct in the ferrocene process. During the S2 stage, the desorption of the precursors that have not reacted with active surface sites seems to occur. The net mass gain detected after the nickelocene pulse, exposure and purging could be attributed to the bonding of a –NiCp group with a surface –OH group.

According to the study performed on Fe_2O_3 [35], the S3 and S4 stages could be associated to a combustion of the chemisorbed –NiCp groups. Those cyclopentadienyl groups should therefore be cracked with the production of CO_2 and H_2O. The surface is then activated again with hydroxyl functions onto the Ni atoms. While a mass loss, corresponding to the combustion of Cp, is expected after the O_3 exposure, the QCM measurements (Figure 2b) do not show any net mass decrease during the step.

This unexpected measurement could be attributed to a cooling effect of the vector gas (Ar) on the quartz. The QCM is indeed a very sensitive characterization tool as the sensor oscillation frequency can easily change when low temperature variations occur. Additional experiments have thus been performed by pulsing only ozone. Without $NiCp_2$, the QCM data exhibit a low level background and no regular increase. This indicates that the general trends of m vs t shown in Figure 2a are relevant but no mechanistic information can be deduced from the detailed interpretation of the QCM measurements. QMS investigation would be required to support the proposed chemical mechanism.

In order to characterize their morphology, the resulting NiO/Ni layers have been studied by electron microscopy. The backscattering electron detection mode was used to enhance the chemical contrast of the image shown in Figure 3. The NiO deposit (red color in the figure) is clearly visible within the Al_2O_3 pores. The NiO film is approximately 10 nm thick after 1000 ALD cycles. The TEM picture presented in Figure 4 shows the as-grown NiO layer deposited within the AAO membrane after removal of the alumina template. The average length of the nanotubes is 5 µm, which indicates that the exposure time to $NiCp_2$ is sufficiently long to allow for the deposition to proceed deeply on the entire surface of the pores. On such a TEM image, several NiO nanotubes can be observed. The NiO layer covers the AAO template homogeneously. Note that no gradient of NiO loading is observed in the deep section of the template. The quantity of matter is identical at the top and the at the bottom of the pores. This is attributed to the self-limiting process of the ALD. The tuning of the duration of the surface exposition to the precursors allows for the reaction of the molecules with the activated surface of the three-dimensional substrates, which exhibit a high aspect-ratio geometry.

The TEM image shows that the morphology of the NiO deposit is highly granular. It therefore increases the active surface area of the electrode for a higher interaction with the electrolyte. Note that the NiO layer is an efficient barrier between the solution and the AAO since we have never observed the dissolution of the AAO during the electrochemical characterizations. To get a metallic Ni film, the as-grown NiO deposit has been annealed in H_2 atmosphere at 300 °C. The SEM observations indicate no significant morphological modifications of the Ni after the reductive annealing (Figure 5). The NiO film shown in Figure 3 (before annealing) exhibits a granularity slightly higher than in Figure 5 (after annealing). It is however difficult to get quantitative results from such SEM pictures. Note that inversely, a treatment performed in Ar at higher temperature (T = 700 °C) has shown a strong increase of the granularity after such annealing [34].

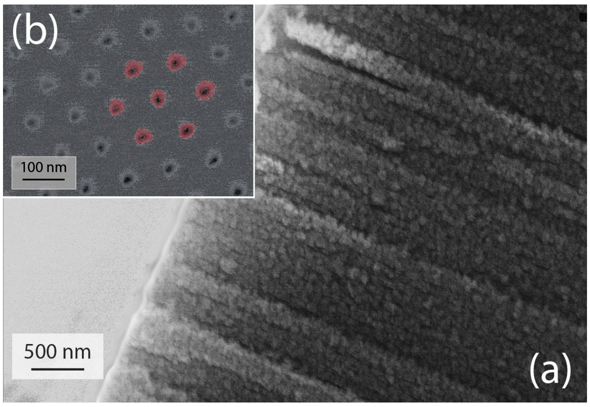

Figure 3: (a) SEM cross section of a NiO layer deposited in AAO membrane. (b) SEM image (obtained in backscattering electron mode) showing NiO grown by ALD within the AAO template. The NiO top layer has been removed by a short Ar sputtering in order to reveal the NiO film coating the vertical pore walls. The NiO deposit is emphasized on the picture using a red overlay.

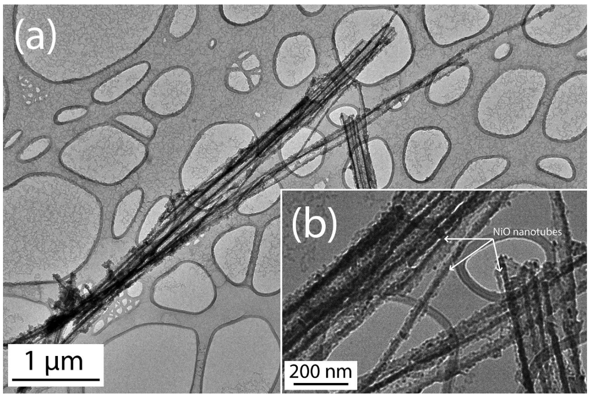

Figure 4: (a) TEM image of NiO nanotubes after alumina template removal. (b) Enlarged view of NiO nanotubes.

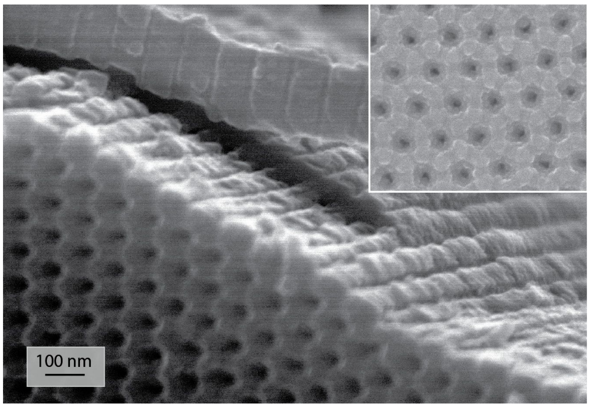

Figure 5: SEM image of Ni layer deposited in an AAO template after 3 h annealing in H_2 at 300 °C of the initially deposited NiO by ALD. The inset shows a detailed top-view of the surface.

The chemical composition as well as the crystal structure of the NiO/Ni layer have been analyzed before and after the reduction stage. The XRD analyses performed on as-grown NiO and after the reduction process indicate that both NiO and Ni layers deposited on AAO are amorphous (XRD patterns are shown in Figure S1, Supporting Information File 1). The surface chemistry of the sample after the reductive annealing of the Ni deposit has been analyzed by XPS. As expected, the spectrum shown in Figure 6 exhibits peaks corresponding to Ni, C and Si but also to O. Although the Ni 2p, Ni 3p and Auger peaks indicate the presence of metallic Ni, the O 1s peak suggests that the Ni deposit remains partially oxidized after the reductive treatment. Since the XPS analysis provides information on the outermost surface, the Ni–O contribution can either originate from an only partial reduction of the initial NiO layer or from the oxidation of the sample while transferring it to the XPS chamber. Note that a contribution coming from SiO_2 in the XPS spectrum in the O 1s binding energies region is possible since an interfacial SiO_2 layer is formed between Si and NiO (Figure S2, Supporting Information File 1). However, the contribution of Si in the survey spectrum is not intense.

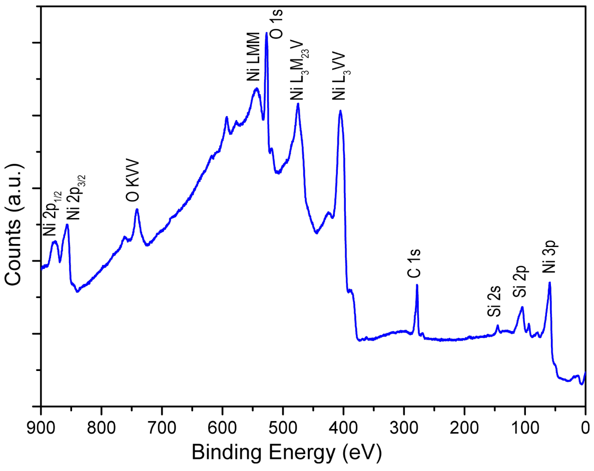

Figure 6: XPS survey spectrum of metallic Ni.

Palladium deposition

A key advantage of ALD is that the growth of materials proceeds according to a two-dimensional mechanism. Nevertheless, for electrocatalytic applications, it is more suitable to have metallic clusters. To obtain such a morphology, it is possible to adjust the deposition parameters and the nature of the precursor. The outcome will depend also on the interaction between the substrate and the deposit. Recently, Elam et al. [25] have reported the synthesis of sub-nanometer Pd particles by an alternating exposure of the substrate to the metallic precursor and to trimethylaluminum. The active hydroxyl sites are thus occupied, which hinders the lateral growth of the particles. As mentioned in the introduction, the growth of Pd clusters by a direct ALD process, which uses palladium hexafluoroacetylacetone ($Pd(hfac)_2$) and formaldehyde, has been previously described [25,36-38]. The mechanism is summarized in Figure 7. Steps 1 and 2 consist of the adsorption of the $Pd(hfac)_2$ precursor onto the surface and its reaction with the hydroxyl sites and a subsequent H-hfac release. After the exposition of the surface to the second precursor (step 3), Pd(hfac) is reduced by formaldehyde. A $–Pd–H_x$ termination is created at the active site and Hhfac, CO and H_2 are released during step 4.

The formation process of the Pd clusters has been monitored by QCM measurements in order to detect the mass gain and loss during the ALD cycles. The general evolution of *m* during the deposition is shown in Figure 8a. Two growth regimes are identified in the curve: before and after 50 cycles. At first, the growth rate of Pd is low and non-linear. It progressively increases and reaches an almost linear growth after 50 ALD cycles. Such behavior has already been observed [36,39]. The initial low growth rate has been attributed to the long nucleation stage of the Pd clusters onto oxidized surfaces and/or

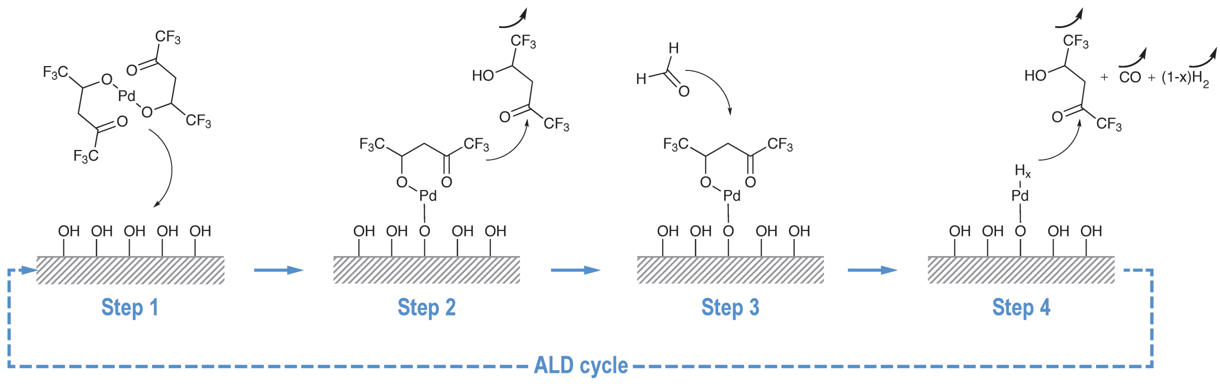

Figure 7: ALD sequence during Pd deposition from $Pd(hfac)_2$ and formaldehyde.

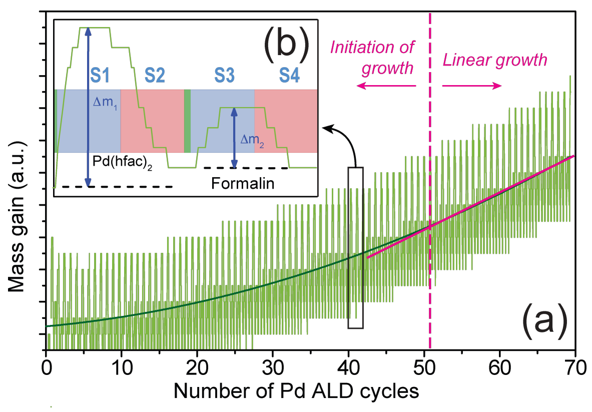

Figure 8: In situ QCM measurements of Pd mass gain during the ALD process for Pd. (a) General evolution and (b) enlarged view of one ALD cycle.

ascribed to the surface poisoning by the precursor ligands by others [38]. An enlarged view on one ALD cycle (Figure 8b) shows the details of the mass gain and loss during the precursor pulses and the pumping of the exposition chamber. Step S1 consists of the adsorption of Pd(hfac)$_2$ precursor molecules onto the surface. At this stage, the mass gain is denoted Δm_1. The end of the exposure time (S1) does not correspond exactly to the maximum of the gain mass Δm_1. The exposure time could thus be decreased to optimize the cycle duration. However, a long exposure duration assures the diffusion of the chemical species toward the pore tips. A similar observation can be done for the pumping time (step S2). Its duration is also not optimized but a longer purge and pumping stage would surely remove all the byproducts and the excess of reactants. George et al. [38] have shown that during the exposure with Pd(hfac)$_2$, the released Hhfac can adsorb onto the hydroxylated Ni surface and block any further Pd reaction at those locations. As mentioned above, this phenomenon can hinder the lateral growth of the Pd film and slows down the deposition rate at the beginning. Steps S3 and S4 describe the surface exposure to the second precursor (formaldehyde) and the purge/pumping of the reactor, respectively. At the end of second part of the ALD cycle, the net mass variation should be negative. After the reaction of HCOH with –Ni–O–Pd(hfac), H-hfac, CO and H_2 are indeed released. However, the QCM measurements show no mass loss. This unexpected measurement could again be attributed to the cooling effect of the vector gas on the quartz oscillation that has been mentioned above for Ni deposition. These data give only an indication on the general deposition process and cannot be used to interpret the growth mechanism. QCM data indicate that Pd deposition takes place onto the surface since the general trend is almost flat if no Pd is pulsed in the chamber.

The morphologies of the Pd films grown onto the NiO layer have been observed by SEM and AFM with and without the reductive annealing treatment in H_2. In order to facilitate such characterizations, the observed NiO and Pd layers have been grown onto flat Si substrates. Note that these depositions onto planar Si and onto AAO membranes have been performed simultaneously. Pd deposits carried out onto as-grown and annealed NiO layers that were grown before onto the Si wafers are presented in Figure 9a and Figure 9b, respectively. Their average diameters are, respectively, about 40 and 10–20 nm. The size of the clusters observed in Figure 9a cannot be attributed to the supporting NiO crystallites since their average size is in the range of 10–15 nm according to TEM cross section shown as supplemental material (Figure S2, Supporting Information File 1). The QCM, XPS and XRD measurements also attest the deposition of Pd onto the NiO layers. Such a spher-

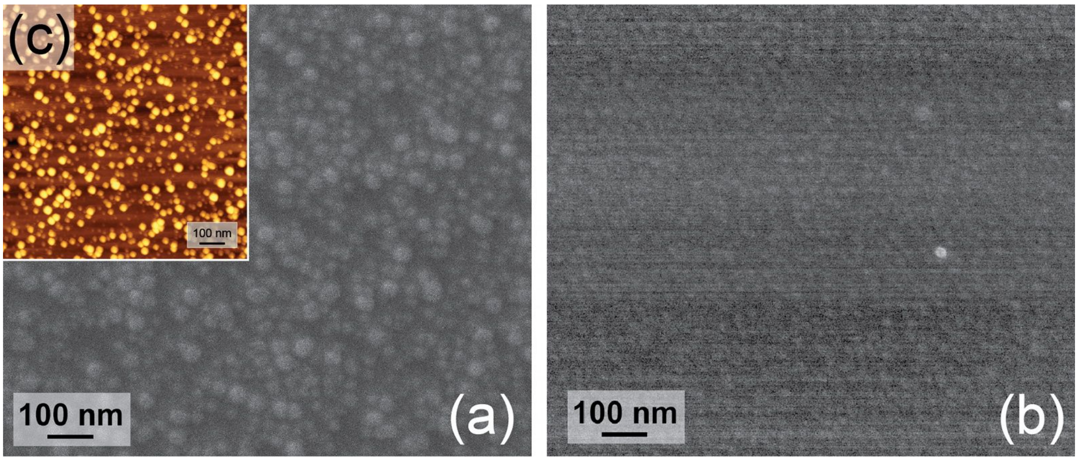

Figure 9: SEM top views of Pd deposits after 100 ALD cycles onto (a) as-grown NiO and (b) reduced NiO films on Si substrate. (c) AFM image of Pd clusters onto as-grown ALD NiO.

ical morphology suggests a Volmer–Weber growth mechanism of Pd. Such a formation of 3D islands is due to the high difference of surface energies between the metallic Pd and the oxidized support [39,40]. The formation of 3D islands can also be supported by the H-hfac ligands that are adsorbed on active –OH sites at the surface after the $Pd(hfac)_2$ pulse [38]. In the case of Figure 9b, it was more difficult to observe the clusters with a high resolution. However the average size is slightly higher than the initial Ni/NiO layer. It indicates therefore that the Pd deposit covers the Ni/NiO film uniformly. This could be due to a lower surface energy between the Pd and the annealed substrate. It is even possible to form a Pd/Ni alloy if the NiO top layer appears only when the sample is exposed to air.

The two different growth mechanisms demonstrate the strong influence of the substrate on the deposition process. Although the XPS data indicate that the reduction of NiO to Ni is not total, the Pd deposition proceeds according to a 2D growth mechanism after the annealing in H_2 atmosphere. In order to optimize the catalyst morphology, it appears that the Pd deposition should be performed onto as-grown NiO because bigger Pd islands are formed then. The AFM image presented in Figure 9c, shows clearly the Pd clusters that cover all of the Ni/NiO layer surface. Since Figure 9a and Figure 9b show planar substrates, they cannot be used to precisely evaluate the size of the Pd particles in the NiO/AAO system. However they give valuable information about the nucleation process of the Pd clusters on the NiO and Ni surfaces. Since atomic layer deposition is a self-limiting layer-by-layer process, it is reasonable to assume that the deposition occurs within the AAO/NiO structures but the particle size should be lower than the one observed on planar substrate. The crystal structure of Pd deposit has been investigated by X-ray diffraction. The XRD patterns shown in Figure 10 depict a polycrystalline structure of the Pd layer with a preferential orientation in the [220] direction (peak at about 70°). The Pd crystallographic structure is face centred cubic (fcc) similar to the structure of bulk Pd metal [11]. The XRD diffractogram suggests therefore the presence of metallic Pd. This result is further confirmed by the XPS analysis (Figure 11) that has revealed the presence of Pd, O and C on the surface. Similarly to Ni, the spectrum indicates the contribution of metallic and oxidized Pd with a slight contribution of O. The presence of Pd–O bonds can also be attributed to the oxidation occurring during the sample transfer to the XPS chamber or to the Pd deposition process itself. As observed for Ni, the Pd layer contains a small amount of C.

Electrooxidation of HCOOH on Pd/Ni layers

According to literature [10-13], Pd/Ni seems to be a more interesting system for the electrooxidation of HCOOH than Pd/NiO. The electrochemical characterizations have thus been performed with the H_2-annealed NiO layers after the deposition of Pd. Figure 12 shows the forward and reverse scans of the third CV cycle on Pd/Ni electrocatalysts deposited onto an AAO membrane in 0.5 M H_2SO_4 before and after adding 1 M HCOOH. From cycle number 1 until cycle number 3, a decrease of the electrocatalytic activity of Pd/Ni system is observed. Indeed, the stability of Ni in H_2SO_4 is not as good as in KOH, however in the potential region of interest no Pd/Ni deactivation due to Ni dissolution has been observed. The third cycle is shown because after three cycles a stable and reproducible behavior of Pd/Ni system was obtained (CVs are identical) in the presence and absence of formic acid. The cyclic voltammogram disclosed in Figure S3 (Supporting Information File 1)

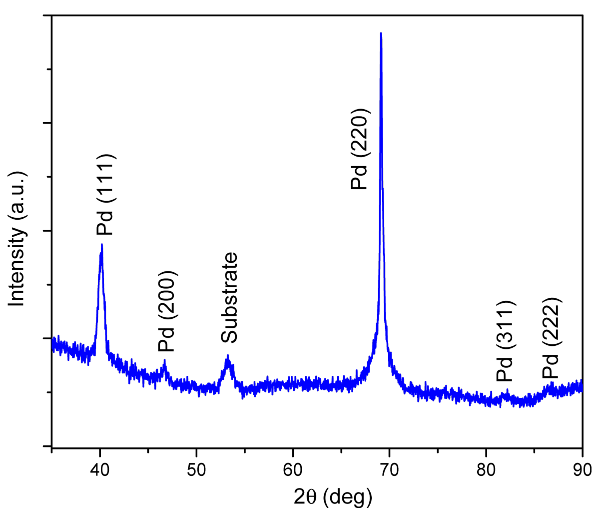

Figure 10: X-ray diffractogram of Pd deposited by ALD exhibiting a polycrystalline structure with a preferential orientation along the fcc [220] direction.

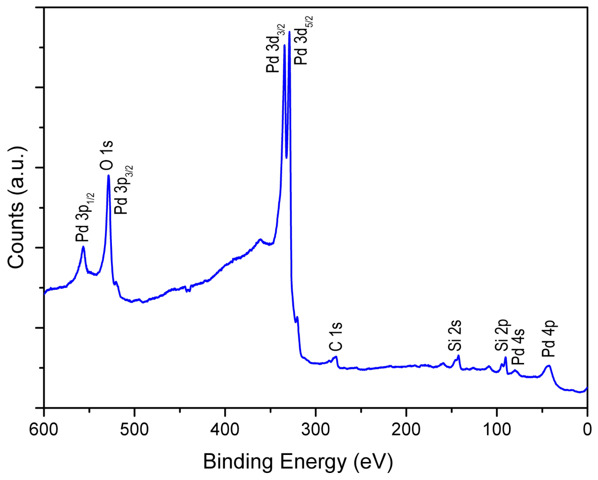

Figure 11: XPS survey spectrum of metallic Pd.

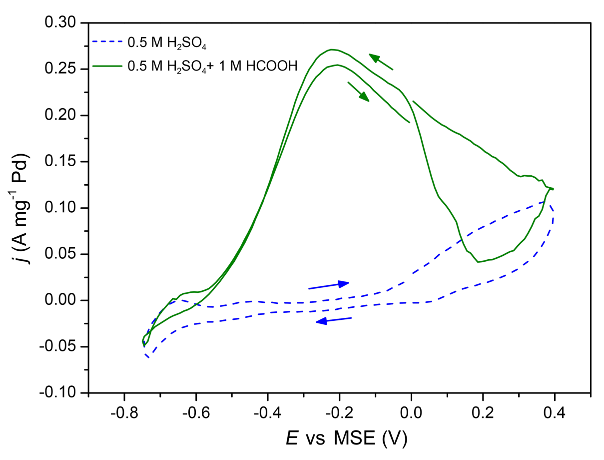

Figure 12: Cyclic voltammograms of Pd(100 ALD cycles)/Ni(1000 ALD cycles) catalysts in 0.5 M H_2SO_4 without (blue dashed line) and with (continuous green line) 1 M HCOOH at 15 mV·s^{-1}. Current densities are given per unit mass of Pd estimated from the QCM measurements.

shows the evolution of the current during the first six cycles. It demonstrates the stability of the Pd/Ni system over time in 0.5 M H_2SO_4.

The Ni and Pd layers were formed after 1000 and 100 ALD cycles, respectively, on alumina membranes. The applied potential varies from −0.75 to 0.4 V vs MSE at 15 mV·s^{-1}. At potentials lower than −0.6 V, the H_2 adsorption/desorption process is observed. Without formic acid in the solution, at potentials between −0.6 and 0 V, the voltammogram exhibits a flat region till approximately 0 V and at higher potentials the formation of Pd oxides starts to take place. In the presence of formic acid, on the other hand, the current begins to increase at a potential of −0.58 V reaching a maximum current density of 0.26 A·mg^{-1} at −0.2 V because of the oxidation of HCOOH. A further increase of the potential leads to a decrease of the current density due to the oxidation of the palladium and the inhibition of the catalytic activity of the metallic system by reaction intermediates [9,41]. On the reverse scan, the current remains low until 0.19 V, at which the reduction of PdO_x begins to take place, and then increases because of the electrooxidation of formic acid on the reduced Pd. Note that the anodic wave that is centered at −0.19 V in the reverse scan is slightly higher than the one during the forward scan. This hysteresis indicates that the Pd surface still remains active and the previously formed oxides are completely reduced when the potential is reversed toward the negative direction. The electrooxidation of HCOOH follows the direct dehydrogenation pathway, which is in agreement with previous works [42]. The effect of the number of Pd ALD cycles (40, 80, 100 and 145) and, consequently, the Pd to Ni ratio on the current peak at −0.19 V, which corresponds to the oxidation of HCOOH is shown in Figure 13. Additionally, the electrochemical characterizations have shown the typical Pd response in H_2SO_4. The obtained results (overpotential for the oxidation of formic acid) are in a good agreement with the literature data reported for Pd/transition metal systems prepared by other techniques [10,13].

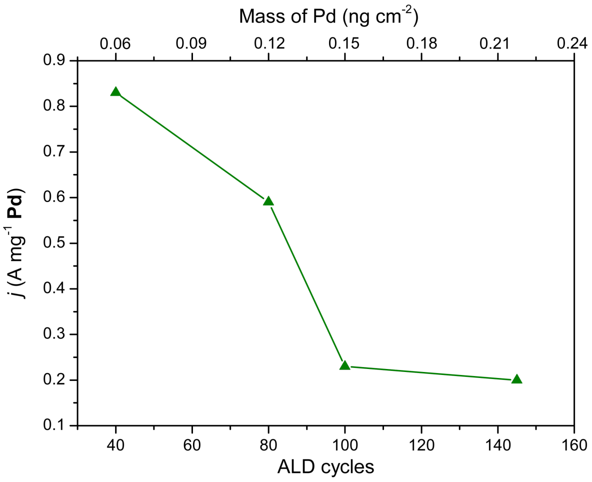

Figure 13: Peak current densities of the electrooxidation of 1 M HCOOH in 0.5 M H_2SO_4 with various Pd contents in the Pd/Ni nanocatalysts, which were obtained with 40 to 145 Pd ALD cycles. The mass of Pd was estimated from the QCM measurements.

The mass activity of the Pd systems decreases to about one fourth from 40 to 145 ALD cycles. The increase of mass of Pd may result in the formation of larger clusters, and subsequently in both a smaller overall active surface area of the catalyst per unit mass, and weaker interactions with the Ni support. These two reasons can explain the negative trend of peak current densities for the oxidation of formic acid on Pd/Ni electrocatalysts with the increase of Pd mass. Note that it can also be because of the mass transport effect [43] since diffusion into such narrow channels can differ strongly from standard 2D models.

Conclusion

In this study, well-defined Pd/Ni nanocatalysts grown by ALD have been investigated for the electrooxidation of formic acid in 0.5 M H_2SO_4. The deposition of nickel oxide from $NiCp_2$ and O_3 precursors on high aspect ratio nanoporous Al_2O_3 has been demonstrated. Although the chemical composition analysis of the NiO layers has not shown that the reductive treatment in H_2 leads to fully metallic films, in which no strong morphological modifications were observed. Furthermore, it was concluded that the oxidized Ni is a better substrate to obtain a three-dimensional growth of Pd islands, which are more suitable for electrocatalytic applications. The Pd deposit is polycrystalline and exhibits a preferential orientation along the [220] direction. For both Ni and Pd depositions, the QCM results were not conclusive with regard to proper information about the deposition mechanisms by ALD. The Pd/Ni bimetallic systems demonstrates a high activity toward the electrooxidation reaction of formic acid and reaches 0.83 A·mg^{-1} for Pd(40 ALD cycles)/Ni(1000 ALD cycles). The electrochemical properties are very similar to those reported in the literature [10-13]. The interaction between Pd and Ni is stronger when the mass of the deposited Pd is decreased because of the lower thickness and size of Pd particles, but also because of the electronic effects between the alloyed Pd/Ni metals or because of the mass transport effect in 3D nanostructures. This explains the trend of higher peak current densities for the electrooxidation of formic acid at a lower Pd content in the Pd/Ni nanocatalysts.

Experimental

The porous alumina structures have been grown on 4 cm wide aluminum discs (Goodfellow, 99.999%) by using the method that is schematically depicted in Figure 1a–e. The aluminum was first electropolished in an alcoholic solution of perchloric acid and successively anodized at a constant voltage, *U*, of 40 V in oxalic acid. A chemical dissolution was performed between the two anodizations to remove the disordered sacrificial Al_2O_3 layer. The resulting alumina membrane is ordered on a large scale area (ca. 10 cm^2); the pore diameter is 40 nm and the length of the pores is about 5 µm. A typical AAO template is shown in Figure 14.

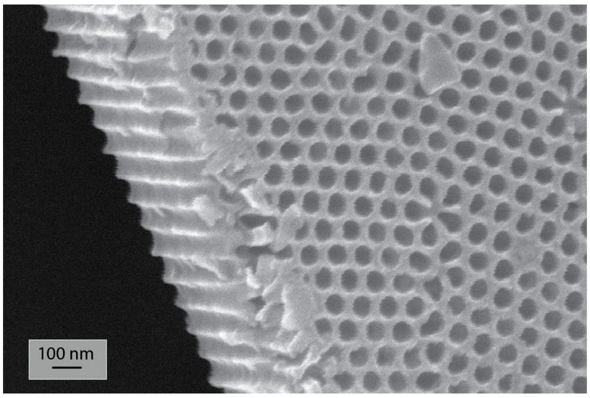

Figure 14: SEM micrograph of an anodic alumina oxide template. After the electropolishing, a sacrificial film was firstly grown by applying 40 V in 0.3 M $H_2C_2O_4$ for 24 h at T = 8 °C and then dissolved in H_2CrO_4 and H_3PO_4 at 50 °C for 12 h. The second anodization step is then carried out during 2.5 h at the same anodic conditions.

The Pd/Ni catalysts have been prepared by ALD in a Fiji 200 reactor from Ultratech/Cambridge Nanotech. The catalysts (Ni and Pd) were deposited both on AAO membranes and on flat Si(100) wafers that were cleaned beforehand by sonication in acetone, isopropanol and ethanol and deoxidized by dipping in 1% HF for 5 s. The alumina template was coated by a thin NiO layer grown from nickelocene ($NiCp_2$, 99% from STREM chemicals), and ozone as chemical precursors. The temperature of the ALD chamber during the deposition was set to 250 °C. The ALD cycle consisted of successive exposures of the sample to $NiCp_2$ and O_3. The pulse durations and exposure time were, respectively, 1 and 30 s for $NiCp_2$ and 0.2 and 20 s for O_3. In both cases, the purging of the chamber was carried out for 30 s. The resulting NiO film was annealed and reduced under a H_2 flow at 300 °C for 3 h to obtain a metallic Ni layer. The last step of the preparation of the catalysts consisted of depositing Pd nanoclusters that have been grown from palladium(II) hexafluoroacetylacetonate ($Pd(hfac)_2$, 98% from STREM chemicals), and formalin (37% formaldehyde in water with 10–15% of methanol from Sigma-Aldrich) at 200 °C. The ALD sequence consisted of successive exposures of the Ni-covered sample to $Pd(hfac)_2$ and formaldehyde. The pulse durations were, respectively, 1 and 3 s. In both cases, the exposure and purge durations were 30 s. Due to the low vapor pressure of the Pd precursor, an argon flow has been injected in the canister for 0.25 s through an additional valve before each precursor pulse in order to enhance the transport of chemical species toward the deposition chamber. Experiments with various number of ALD cycles of the different precursors have been performed to adjust the mass and the composition of the films. A chemical etching performed in chromic acid solution allows to chemically dissolve the alumina template to allow for the nanostructured catalysts to be collected by centrifugation for further TEM observations of the catalysts out of the alumina template. The Pd/Ni catalysts have been deposited both on 3D alumina templates and flat Si(100) wafers in order to facilitate the chemical and structural characterizations. In situ monitoring of the relative mass gain and loss was performed by using a quartz crystal microbalance (QCM from Inficon). The QCM is connected to the ALD chamber and driven by a SQM-160 controller for data acquisition. The morphology of Al_2O_3 templates and Pd/Ni electrocatalysts has been observed by SEM and TEM using, respectively, JEOL 6320-F and JEOL 3010 equipment. Some additional morphological investigations have been carried out by non-contact AFM using a XE 100 microscope from Park systems. The crystalline structure of NiO, Ni and Pd has been characterized by X-ray diffraction using an INEL diffractometer equipped with a quartz monochromator and a horizontally disposed 1D curved position detector (CPS-120) that covers a 2θ angle of 120°. The measurements were obtained in reflection mode with an incident angle of 10° and Cu Kα1 (1.54056 Å) radiation. X-ray photoelectron spectroscopy by using a Mg electrode Kα (1253.6 eV) source (HA150 from VSW) was used for surface chemistry composition analysis. The Electrooxidation of HCOOH on alumina-supported Pd/Ni catalysts after reductive annealing treatment of the NiO ALD layer has been studied in 0.5 M H_2SO_4 solution in a three-electrode teflon cell. A large surface area Pt mesh and a mercury sulfate electrode (MSE) served respectively as counter and reference electrodes. The geometric area of the working electrode was 0.196 cm^2. The electrical contact to the working electrode was established by a gold wire on the Pd/Ni layer. Cyclic voltammetry was carried out by using a BioLogic VSP potentiostat together with the EC-Lab software at room temperature. The CVs were performed in the potential region from −0.75 to 0.4 V vs MSE at a scanning rate of 15 $mV \cdot s^{-1}$. The current densities have been reported per unit mass of Pd (details on the Pd mass calculations can be found in Supporting Information File 1).

Supporting Information

Supporting Information File 1

Additional experimental details
[http://www.beilstein-journals.org/bjnano/content/supplementary/2190-4286-5-16-S1.pdf]

Acknowledgements

The authors acknowledge Damien Chaudanson and Serge Nitsche for their precious help with the electron microscopy, Jean-Yves Hoarau for XPS analysis and Vasile Heresanu for XRD measurements and interpretation. This work was supported by the France Canada Research Fund. The European Regional Development Fund (ERDF), the PACA Regional Council, the French Ministry of Higher Education and Research and the CNRS are also acknowledged for funding.

References

1. Yu, X.; Pickup, P. G. *J. Power Sources* **2008,** *182,* 124–132. doi:10.1016/j.jpowsour.2008.03.075
2. Rice, C.; Ha, S.; Masel, R. I.; Wieckowski, A. *J. Power Sources* **2003,** *115,* 229–235. doi:10.1016/S0378-7753(03)00026-0
3. Rice, C.; Ha, S.; Masel, R. I.; Waszczuk, P.; Wieckowski, A.; Barnard, T. *J. Power Sources* **2002,** *111,* 83–89. doi:10.1016/S0378-7753(02)00271-9
4. Liu, Z.; Hong, L.; Tham, M. P.; Lim, T. H.; Jiang, H. *J. Power Sources* **2006,** *161,* 831–835. doi:10.1016/j.jpowsour.2006.05.052
5. Choi, J. H.; Noh, S. Y.; Han, S. D.; Yoon, S. K.; Lee, C.-S.; Hwang, T.-S.; Rhee, Y. W. *Korean J. Chem. Eng.* **2008,** *25,* 1026–1030. doi:10.1007/s11814-008-0167-2
6. Antolini, E. *Energy Environ. Sci.* **2009,** *2,* 915–931. doi:10.1039/B820837A
7. Baik, S. M.; Han, J.; Kim, J.; Kwon, Y. *Int. J. Hydrogen Energy* **2011,** *36,* 14719–14724. doi:10.1016/j.ijhydene.2011.04.181
8. Yang, L.; Su, H.; Shu, T.; Liao, S. *Sci. China: Chem.* **2012,** *55,* 391–397. doi:10.1007/s11426-011-4485-6
9. Du, C.; Chen, M.; Wang, W.; Yin, G. *ACS Appl. Mater. Interfaces* **2011,** *3,* 105–109. doi:10.1021/am100803d
10. Xu, C.; Liu, Y.; Wang, J.; Geng, H.; Qiu, H. *J. Power Sources* **2012,** *199,* 124–131. doi:10.1016/j.jpowsour.2011.10.075
11. Shen, S. Y.; Zhao, T. S.; Xu, J. B.; Li, Y. S. *J. Power Sources* **2010,** *195,* 1001–1006. doi:10.1016/j.jpowsour.2009.08.079
12. Baranova, E. A.; Miles, N.; Mercier, P. H. J.; Page, Y. L.; Patarachao, B. *Electrochim. Acta* **2010,** *55,* 8182–8188. doi:10.1016/j.electacta.2009.12.090
13. Hu, S.; Ha, S.; Scudiero, L. *Electrochim. Acta* **2013,** *105,* 362–370. doi:10.1016/j.electacta.2013.05.012
14. Zhong, C.-J.; Luo, J.; Fang, B.; Wanjala, B. N.; Njoki, P. N.; Loukrakpam, R.; Yin, J. *Nanotechnology* **2010,** *21,* 062001. doi:10.1088/0957-4484/21/6/062001
15. Feng, H.; Elam, J. W.; Libera, J. A.; Setthapun, W.; Stair, P. C. *Chem. Mater.* **2010,** *22,* 3133–3142. doi:10.1021/cm100061n
16. Lu, J.; Liu, B.; Greeley, J. P.; Feng, Z.; Libera, J. A.; Lei, Y.; Bedzyk, M. J.; Stair, P. C.; Elam, J. W. *Chem. Mater.* **2012,** *24,* 2047–2055. doi:10.1021/cm300203s
17. Haukka, S.; Lakomaa, E. L.; Suntola, T. Adsorption controlled preparation of heterogeneous catalysts. In *Adsorption and its Applications in Industry and Environmental Protection;* Dabrowski, A., Ed.; Studies in Surface Science and Catalysis, Vol. 120A; Elsevier: Amsterdam, 1999; pp 715–750.
18. Detavernier, C.; Dendooven, J.; Sree, S. P.; Ludwig, K. F.; Martens, J. A. *Chem. Soc. Rev.* **2011,** *40,* 5242–5253. doi:10.1039/c1cs15091j
19. Elam, J. W.; Dasgupta, N. P.; Prinz, F. B. *MRS Bull.* **2011,** *36,* 899–906. doi:10.1557/mrs.2011.265
20. Lu, J.; Elam, J. W.; Stair, P. C. *Acc. Chem. Res.* **2013,** *46,* 1806–1815. doi:10.1021/ar300229c
21. Goldstein, D. N.; George, S. M. *Appl. Phys. Lett.* **2009,** *95,* 143106. doi:10.1063/1.3238558
22. Binder, A.; Seipenbusch, M. *Appl. Catal., A* **2011,** *396,* 1–7. doi:10.1016/j.apcata.2010.12.030
23. Liang, X.; Lyon, L. B.; Jiang, Y.-B.; Weimer, A. W. *J. Nanopart. Res.* **2012,** *14,* No. 943. doi:10.1007/s11051-012-0943-0
24. Rikkinen, E.; Santasalo-Aarnio, A.; Airaksinen, S.; Borghei, M.; Viitanen, V.; Sainio, J.; Kauppinen, E. I.; Kallio, T.; Krause, A. O. I. *J. Phys. Chem. C* **2011,** *115,* 23067–23073. doi:10.1021/jp2083659
25. Feng, H.; Libera, J. A.; Stair, P. C.; Miller, J. T.; Elam, J. W. *ACS Catal.* **2011,** *1,* 665–673. doi:10.1021/cs2000957
26. Chen, Y.-X.; Lavacchi, A.; Chen, S.-P.; di Benedetto, F.; Bevilacqua, M.; Bianchini, C.; Fornasiero, P.; Innocenti, M.; Marelli, M.; Oberhauser, W.; Sun, S.-G.; Vizza, F. *Angew. Chem., Int. Ed.* **2012,** *51,* 8500–8504. doi:10.1002/anie.201203589
27. Moyen, E.; Santinacci, L.; Masson, L.; Sahaf, H.; Macé, M.; Assaud, L.; Hanbücken, M. *Int. J. Nanotechnol.* **2012,** *9,* 246–259. doi:10.1504/IJNT.2012.045330
28. Moyen, E.; Santinacci, L.; Masson, L.; Wulfhekel, W.; Hanbücken, M. *Adv. Mater.* **2012,** *24,* 5094–5098. doi:10.1002/adma.201200648
29. Rüffer, D.; Huber, R.; Berberich, P.; Albert, S.; Russo-Averchi, E.; Heiss, M.; Arbiol, J.; Fontcuberta i Morral, A.; Grundler, D. *Nanoscale* **2012,** *4,* 4989–4995. doi:10.1039/c2nr31086d
30. Peck, M. A.; Langell, M. A. *Chem. Mater.* **2012,** *24,* 4483–4490. doi:10.1021/cm300739y
31. Miikkulainen, V.; Leskelä, M.; Ritala, M.; Puurunen, R. L. *J. Appl. Phys.* **2013,** *113,* 021301. doi:10.1063/1.4757907
32. Lim, B. S.; Rahtu, A.; Gordon, R. G. *Nat. Mater.* **2003,** *2,* 749–754. doi:10.1038/nmat1000
33. Chae, J.; Park, H.-S.; Kang, S.-w. *Electrochem. Solid-State Lett.* **2002,** *5,* C64–C66. doi:10.1149/1.1475199

34. Bachmann, J.; Zolotaryov, A.; Albrecht, O.; Goetze, S.; Berger, A.; Hesse, D.; Novikov, D.; Nielsch, K. *Chem. Vap. Deposition* **2011,** *17,* 177–180. doi:10.1002/cvde.201004300
35. Martinson, A. B. F.; DeVries, M. J.; Libera, J. A.; Christensen, S. T.; Hupp, J. T.; Pellin, M. J.; Elam, J. W. *J. Phys. Chem. C* **2011,** *115,* 4333–4339. doi:10.1021/jp110203x
36. Elam, J. W.; Zinovev, A.; Han, C. Y.; Wang, H. H.; Welp, U.; Hryn, J. N.; Pellin, M. J. *Thin Solid Films* **2006,** *515,* 1664–1673. doi:10.1016/j.tsf.2006.05.049
37. Stair, P. C. *J. Chem. Phys.* **2008,** *128,* 182507. doi:10.1063/1.2824939
38. Goldstein, D. N.; George, S. M. *Thin Solid Films* **2011,** *519,* 5339–5347. doi:10.1016/j.tsf.2011.02.037
39. Weber, M. J.; Mackus, A. J. M.; Verheijen, M. A.; van der Marel, C.; Kessels, W. M. M. *Chem. Mater.* **2012,** *24,* 2973–2977. doi:10.1021/cm301206e
40. Campbell, C. T. *Surf. Sci. Rep.* **1997,** *27,* 1–111. doi:10.1016/S0167-5729(96)00011-8
41. Capon, A.; Parsons, R. *J. Electroanal. Chem.* **1975,** *65,* 285–305. doi:10.1016/0368-1874(75)85124-0
42. Li, R.; Wei, Z.; Huang, T.; Yu, A. *Electrochim. Acta* **2011,** *56,* 6860–6865. doi:10.1016/j.electacta.2011.05.097
43. Lindström, R. W.; Seidel, Y. E.; Jusys, Z.; Gustavsson, M.; Wickman, B.; Kasemo, B.; Behm, R. J. *J. Electroanal. Chem.* **2010,** *644,* 90–102. doi:10.1016/j.jelechem.2009.04.034

License and Terms

The definitive version of this article is the electronic one which can be found at:
doi:10.3762/bjnano.5.16

Beilstein Journal
of Nanotechnology

Photovoltaic properties of ZnO nanorods/p-type Si heterojunction structures

Rafal Pietruszka*[1], Bartlomiej S. Witkowski[1], Grzegorz Luka[1],
Lukasz Wachnicki[1], Sylwia Gieraltowska[1], Krzysztof Kopalko[1],
Eunika Zielony[2], Piotr Bieganski[2], Ewa Placzek-Popko[2]
and Marek Godlewski[1,3]

Full Research Paper

Open Access

Address:
[1]Institute of Physics, Polish Academy of Sciences, Warsaw, Poland,
[2]Institute of Physics, WroclawUniversity of Technology, Wroclaw,
Poland and [3]Department of Mathematics and Natural Sciences
College of Science, Cardinal Stefan Wyszynski University, Warsaw,
Poland

Email:
Rafal Pietruszka* - pietruszka@ifpan.edu.pl

* Corresponding author

Keywords:
atomic layer deposition; hydrothermal method; solar cells; zinc oxide;
zinc oxide nanorods

Beilstein J. Nanotechnol. **2014,** *5,* 173–179.
doi:10.3762/bjnano.5.17

Received: 27 September 2013
Accepted: 16 January 2014
Published: 14 February 2014

This article is part of the Thematic Series "Energy conversion applications of atomic layer deposition".

Guest Editor: J. Bachmann

Abstract

Selected properties of photovoltaic (PV) structures based on n-type zinc oxide nanorods grown by a low temperature hydrothermal method on p-type silicon substrates (100) are investigated. PV structures were covered with thin films of Al doped ZnO grown by atomic layer deposition acting as transparent electrodes. The investigated PV structures differ in terms of the shapes and densities of their nanorods. The best response is observed for the structure containing closely-spaced nanorods, which show light conversion efficiency of 3.6%.

Introduction

Solar cells are intensively studied as an alternative energy source and may replace conventional energy sources based on fossil fuels in the future. Since the first photovoltaic (PV) structures were shown by the Bell Laboratories in the 1950s [1], concentrated efforts led to the development of a range of possible PV systems. Nowadays multi-junction photovoltaic structures have an efficiency beyond 40% under laboratory conditions [2,3]. Typical PV structures achieve an efficiency of about 20% for crystalline silicon [4] and about 16% for cadmium telluride [5]. Unfortunately, the high costs of the generated electricity prevents that PV systems are more widely spread. The interest in photovoltaic (PV) structures stems from the fact that solar cells are environmentally friendly, rather than from the low costs of energy production. To reduce these costs, efforts to improve efficiency and a concentrated search for cheaper materials and structures are undertaken.

Wide band gap semiconductors have been studied since the 1930s [6], and several applications have been found in the past decades. For example, they are used in PV systems based on thin films, so-called PV structures of the second generation [7-9]. At the moment, zinc oxide is the most studied wide band gap material [10-14]. ZnO has a 3.37 eV direct band gap at room temperature [15] and a high excitation binding energy of 60 meV. It is intensively studied for light emitters in the near-UV region of the spectrum [16,17], or for spintronic applications [18-20], since ferromagnetic thin films of ZnO can be used to store data for a long period of time [21]. In PV structures, ZnO can replace the commonly used indium tin oxide (ITO) as a transparent electrode. Thin films of ZnO doped with aluminum (ZnO:Al, AZO) or gallium (ZnO:Ga, GZO) obtained by various deposition methods, show a resistivity of the order of 10^{-4} Ω·cm and a high transparency [22,23]. Due to these properties and the low costs of ZnO and deposition methods, ZnO:Al films may be used in PV structures as a replacement for expensive ITO layers [24-26].

One-dimensional (1D) nanostructures such as nanorods attracted a lot of attention due to their ability of being used as building blocks for future electronic, photonic, electromechanical and PV devices [27-32]. Many research groups have been working on various 1D semiconductor systems for the past few years [33-35].

In this work, we study PV structures based on zinc oxide nanorods grown by a hydrothermal method on top of p-type Si, covered on top with ZnO:Al films grown by atomic layer deposition (ALD) and acting as a transparent electrode. These simple and low costs solar cells show a power conversion efficiency, which we consider satisfactory.

Experimental

In this work, we investigate n-type ZnO/p-type Si heterostructures. P-type (100) silicon wafer with a resistance of 2.32 Ω cm was cut into pieces of the size of 0.5 cm^2. Cut silicon pieces were cleaned in 2-propanol, acetone and deionized water for 5 minutes by using an ultrasonic cleaner. Then, in the ALD process with 15 cycles, ZnO nanoseeds were deposited on a Si substrate (Figure 1a). The deposited ZnO nano-islands nucleate growth of ZnO nanorods in a hydrothermal process, performed in a Ertec01-03 Magnum reactor [36-39]. The growth of the ZnO nanorods was performed at atmospheric pressure and a temperature of about 60 °C.

The reaction mixture was prepared by dissolving zinc acetate in deionized water. Due to the precipitation of sodium hydroxide we obtained a solution with pH values of 7, 7.5 and 8. The pH values in this range control the size and density of nanorods. For example, given a solution with a pH value of 7 the ZnO nanorods have a length of approximately 800 nm and a width of approximately 300 nm. For higher pH values, the length of the nanorods increases their width decreases, and their density increases. For pH 8, the nanorods have a width of approximately 200 nm, a length of approximately 800 nm, and are close to each other. Average sizes of ZnO NRs and ZnO NRs covered ZnO:Al layers are summarized in Table 1. We obtained three distinct types of ZnO nanorods by changing the pH values denoted as sample A, sample B and sample C.

ZnO with aluminum atoms (AZO) were grown on ZnO nanorods (ZnO_{NR})/Si structures by using the ALD process in the Savannah-100 reactor Cambridge NanoTech (Figure 1b) [40,41]. We used diethylzinc (DEZ) and deionized water as zinc and oxygen precursors, respectively. For doping zinc oxide

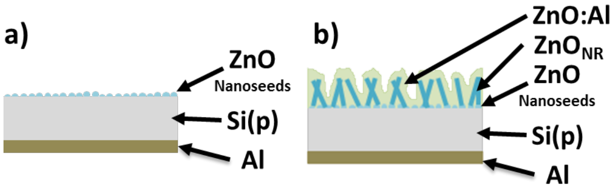

Figure 1: Schematic drawings of the investigated solar cells structure based on zinc oxide nanorods (not to scale).

Table 1: Average sizes of ZnO NRs and ZnO NRs covered ZnO:Al grown at different pH values.

pH	Average height of ZnO NRs [nm]	Average width of ZnO NRs [nm]	Average height of ZnO:Al/ZnO NRs [nm]	Average width of ZnO:Al/ZnO NRs [nm]
7	800	300	1100	800
7.5	1050	400	1400	800
8	800	200	1150	650

layers trimethylaluminum (TMA) was used as an aluminum precursor. The growth temperature was 160 °C and the N_2 was used as a purging gas. To obtain a high conductivity of the ZnO film, we mixed ALD cycles. We applied 1 cycle TMA + H_2O and 24 cycles of DEZ + H_2O to obtain a uniform distribution of Al in the layer. The lowest resistivity was achieved for ZnO:Al films with 3% of Al. Further details of the ALD growth process are given in our recent publication [42]. Although the growth temperature was relatively low (160 °C), we achieved a metallic-like conductivity. Concentrations, mobilities and resistivities of ZnO:Al films and Si substrates are listed in Table 2. Please note that the low growth temperature – which still facilitates a high conductivity – is important, since we plan to deposit future test devices on transparent foils.

Aluminum ohmic contacts to p-type Si were deposited by e-beam evaporation (PVD 75, Kurt Lesker). The obtained solar cell structures were characterized by a Scanning Electron Microscope Hitachi SU-70 with an accelerating voltage of 15 kV. PV response was measured by using current–voltage (*I–V*) curve tracer for fast *I–V* measurements with a sun simulator cl. AAA, at an illumination irradiance of 100 mW/cm^2. Quantum efficiency was measured by using the PV Quantum efficiency system (EQE and IQE) (300–1100 nm) (Bentham U.K.) and a bias-light.

Results

Figure 2 shows scanning electron microscope (SEM) images of three types of the studied ZnO:Al/ZnO$_{NR}$/Si/Al PV structures denoted as A, B and C. Figure 1 (up) shows the cross section and the top view of the nanorods. Figure 2 (down) shows zinc oxide nanorods covered with AZO films. The samples A and B exhibited a similar density of nanorods. For samples A (pH 7) the calculated average length was 800 nm and the width 300 nm. We noticed an increased length and width with an increasing pH value from 7 to 7.5. For samples B (pH 7.5) the length increased from 800 nm to 1050 nm and the width increased from 300 nm to 400 nm. The average density did not change. However, pH values higher than 7.5 lead to decreased lengths and widths. Zinc oxide NRs grown at pH 8 show an average length of 800 nm and a width of 200 nm. For samples C we obtained the highest density of nanorods. The average thickness of ZnO:Al layers was 350 nm. The width changed significantly for samples A and B. The average width for samples A and B is 800 nm and for sample C 650 nm. Different sizes of nanorods enable us to study the influence of ZnO$_{NR}$ on the electrical and optical properties of the ZnO$_{NR}$/Si PV structures.

Dark *I–V* characteristics of the structures are shown in Figure 3a. From the dark *I–V* measurements we see that the size and density of the nanorods affect the diode parameters. Sample A and sample B with similar widths and densities of the nanorods display similar *I–V* curves. Rectification ratios calculated at 1 V are about 10^2 for the samples A and B and 4.7×10^3 for the sample C. For nanorods with a low density (structures A and B) the deposited ZnO:Al films cover not only nanorods but also fill in the gaps between them (Figure 4). Samples A and B show a core-shell structure with the zinc oxide nanorod being the core and the AZO layer being the shell. For closely packed nanorods (sample C) the AZO film is grown only on the top of the nanorods. However, we also observed growths of AZO films between single nanorods. Thus, the sample C is the only one to have a “clean” junction between ZnO$_{NR}$ and the silicon as well as an AZO film acting as a transparent top electrode. The fact that the structure C shows the best junction properties indicates that the quality of ZnO nanorods affects the results.

The most important parameter for a comparison of solar cells is the efficiency (η) of light conversion. The efficiency is defined as the ratio of the energy output from the cells ($P_{\max}$) to the input energy from the sun (P_{in}). In this work, the efficiency of the solar cells was calculated by using the equation:

$$\eta = \frac{P_{\max}}{P_{\text{in}}} = \frac{V_{\text{oc}} J_{\text{sc}} FF}{P_{\text{in}}} \tag{1}$$

where V_{oc} is the open-circuit voltage, J_{sc} is the short-circuit current, and *FF* is the fill factor.

The fill factor (*FF*) determines the maximum power from the PV cells. The fill factor is the ratio of the real output from the solar cell ($V_m \times J_m$) to the product of $V_{\text{oc}} \times J_{\text{sc}}$. The fill factor can be expressed by the following equation:

Table 2: Electrical parameters of investigated PV structures grown on p Si substrates.

	Thickness	Mobility [cm^2/Vs]	Concentration [cm^{-3}]	Conductivity [Ω^{-1}cm^{-1}]	Resistivity [Ω·cm]	Carrier type
ZnO:Al	350 nm	11.1	3.33×10^{20}	629	1.89×10^{-3}	electrons
Si	270 μm	297	9.08×10^{15}	0.43	2.32	holes

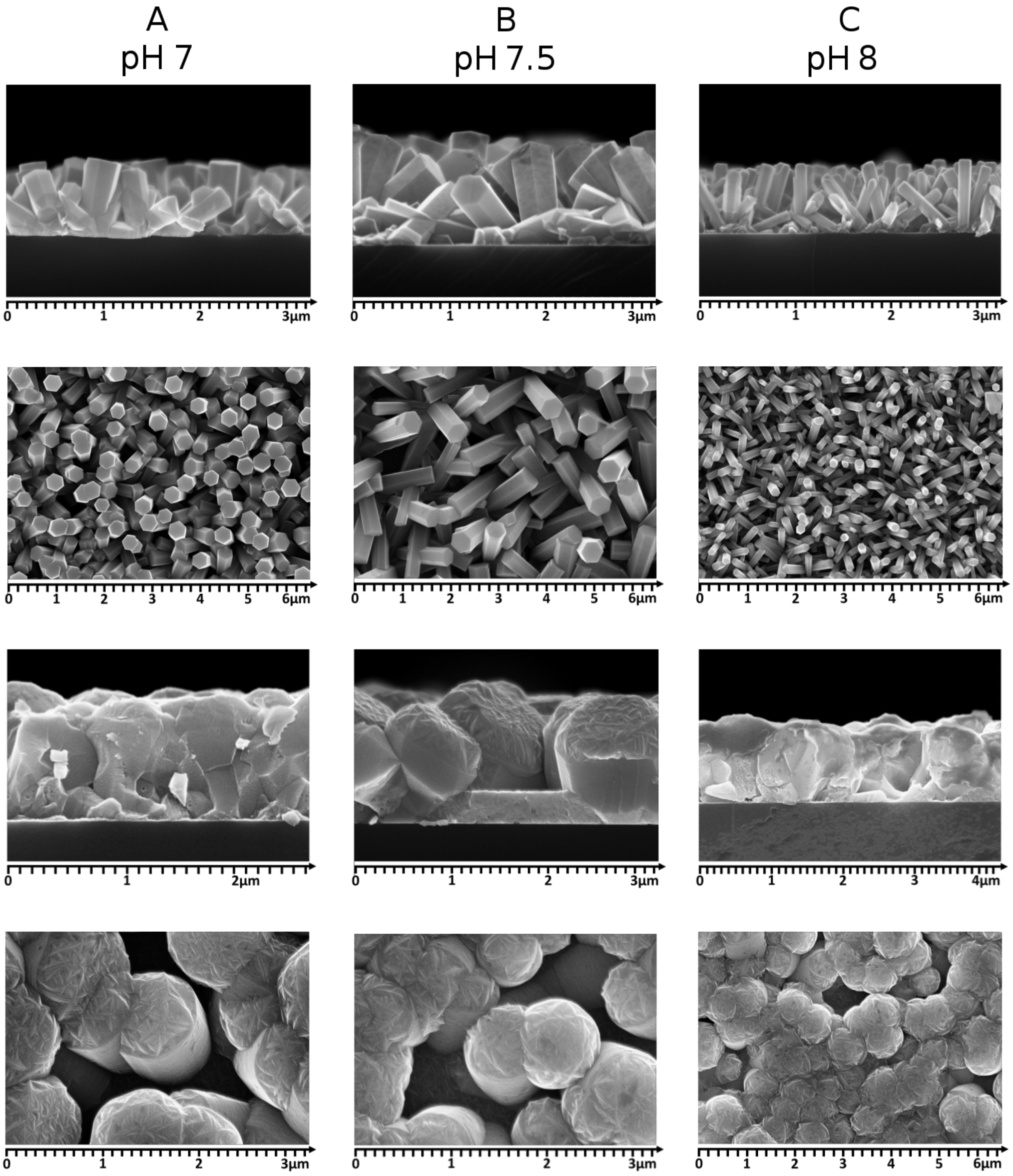

Figure 2: Cross-section and top view (up) SEM images illustrating zinc oxide nanorods grown at different pH values of 7, 7.5 and 8. Images at the bottom show cross-section and top view of ZnONR covered with ZnO:Al layers.

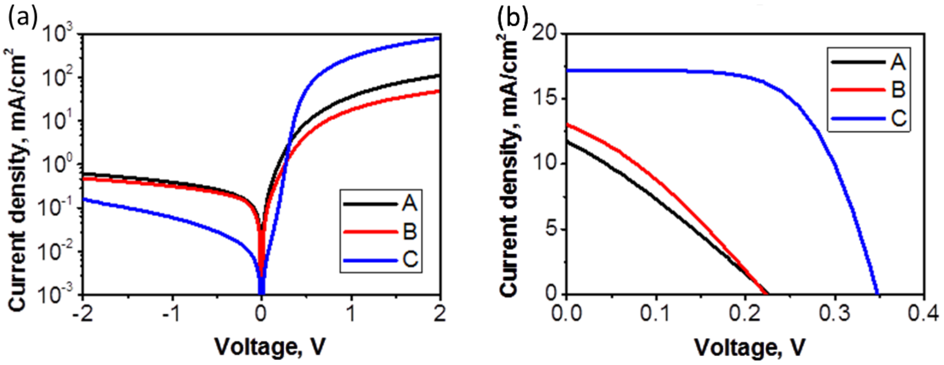

Figure 3: Current–voltage characteristics for the ZnO:Al/ZnO$_{NR}$/Si/Al heterostructures measured under dark (top) and under light conditions (down).

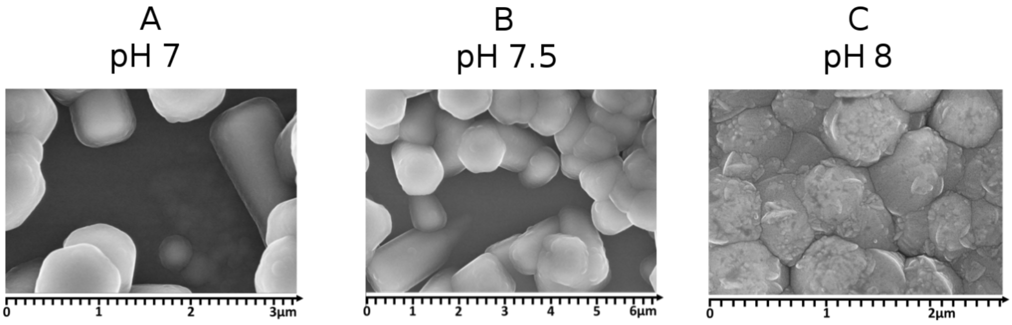

Figure 4: SEM images of the three investigated types of structures with different surface morphologies.

$$FF = \frac{V_m J_m}{V_{oc} J_{sc}} \tag{2}$$

where V_m is the value of the voltage for the maximum power from a solar cell, and J_m is the value of the current for the maximum power from a solar cell.

Figure 3b shows *I*–*V* characteristics for the samples A, B and C measured under an illumination of 100 mW/cm^2. The photovoltaic parameters obtained from the fit are summarized in Table 3. The given data allows the determination of the relationship between R_{sh} (shunt resistance), R_s (series resistance) and the PV response. For the samples A and B the shunt resistance is very low. The low value of the shunt resistance indicates the presence of a low connection of recombination paths for photo-generated electron-hole pairs. The large value of R_{sh} reduces the current flowing through the junction and reduces the value of V_{oc}. The current value is influenced by the structure morphology. Samples A and B show a non-uniform ZnO:Al layer morphology. Probably, this increases the scattering of photo-generated carriers. Sample C with uniform AZO film morphology exhibits the highest value of photo-generated current. The calculated value of R_s is relatively high for samples A and B. The main impact of R_s is the reduction of *FF* in the investigated structures. In case of sample C, the best value of R_s equals 5.1 Ω. We noticed that *FF* decreases from 38% to 28% when R_s increases from 5.1 Ω to 20.8 Ω. We observe an increase of the short circuit current, open circuit voltage and the filling factor for sample C. Consequently, the best PV response is observed for sample C with a value of 3.6%.

Figure 5 shows the external quantum efficiency measured with an illumination in the range of 350–1200 nm. The investigated PV structures react to the light from 380 nm to 1150 nm. For all samples the highest value of generated photocurrent flows through the junction with an illumination in the range of 900 nm to 1000 nm, i.e., when carriers are generated in a Si substrate. Samples with a similar value of the shunt resistance (A, B) have a similar photoresponse curves. Quantum efficiency values calculated at 950 nm for the samples A, B and C are 2.51×10^{-2}%, 3.39×10^{-2}% and 3.17×10^{-2}%, respectively. The quantum efficiency of structure C, the one with the highest efficiency, is twice as large as for the samples A and B when illuminated with light in the range of 350 nm to 700 nm. This may be explained by the increased absorption of ZnO NRs

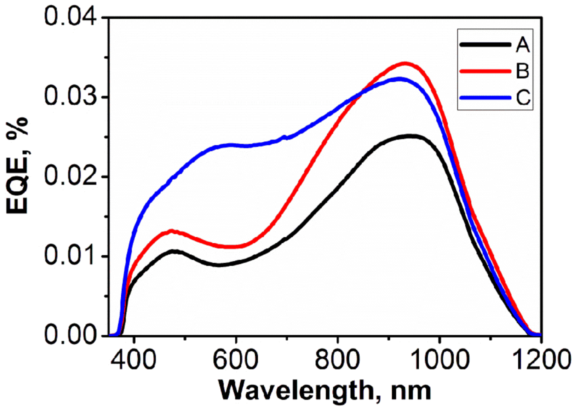

Figure 5: External quantum efficiency of the PV structures of samples A, B and C based on zinc oxide nanorods.

Table 3: Photovoltaic parameters for the investigated heterostructures.

No.	R_{sh} [Ω]	R_s [Ω]	J_{sc} [mA/cm^2]	V_{oc} [V]	J_m [mA/cm^2]	V_m [V]	*FF* [%]	Efficiency [%]
A	69.8	20.8	12	0.23	6	0.12	28	0.9
B	86.7	11.8	13	0.23	8	0.12	30	1
C	2038	5.1	17	0.35	16	0.22	38	3.6

due to the presence of defect states with energies below the ZnO conduction band gap edge. A similar phenomenon was observed by us in case of a ZnO–organic heterojunction, where an increased absorption in the blue-violet spectra range contributed to a higher PV efficiency of the obtained hybrid PV cells [43]. However, a detailed explanation of the effect observed in this work will require a further study.

Conclusion

We investigated PV structures based on zinc oxide nanorods. Their 3D morphology leads to an increased light trapping. ZnO_{NR} with different sizes and density were grown on silicon surfaces by the hydrothermal method. AZO films were grown at a low deposition temperature in the ALD process. This method has the potential of scaling up substrate sizes to more than 1 m^2. A wide spectral range of the absorption (from 350 nm to 1200 nm) was observed. The wide working spectrum and the good junction quality led to 3.6% quantum efficiency, which can be further improved by, e.g., the plasmonic effect, a refinement of the electrical parameters of the AZO films (higher growth temperature), and an optimization of the contacts (the results given here were collected by using a point contact to AZO films). The investigated PV structures are cheap and easily constructed. We used cheap Si substrates, a very efficient and low-cost technology to produce both nanorods and AZO films, and inexpensive precursors of reactions.

Acknowledgements

This work was partially supported by the European Union within the European Regional Development Fund, by the Innovative Economy grant (POIG.01.01.02-00-108/09), by the National Centre for Research and Development with the grant (PBS1/A5/27/2012), and by the National Laboratory of Quantum Technologies (POIG. 02.02.00-00-003/08-00).

References

1. Chapin, D. M.; Fuller, C. S.; Pearson, G. L. *J. Appl. Phys.* **1954,** *25,* 676–677. doi:10.1063/1.1721711
2. King, R. R.; Law, D. C.; Edmondson, K. M.; Fetzer, C. M.; Kinsey, G. S.; Yoon, H.; Sherif, R. A.; Karam, N. H. *Appl. Phys. Lett.* **2007,** *90,* 183516. doi:10.1063/1.2734507
3. Green, M. A.; Emery, K.; Hishikawa, Y.; Warta, W.; Dunlop, E. D. *Prog. Photovoltaics* **2012,** *20,* 606–614. doi:10.1002/pip.2267
4. Descoeudres, A.; Holman, Z. C.; Barraud, L.; Morel, S.; de Wolf, S.; Ballif, C. *IEEE J. Photovoltaics* **2013,** *3,* 83–89. doi:10.1109/JPHOTOV.2012.2209407
5. Gupta, A.; Compaan, A. D. *Appl. Phys. Lett.* **2004,** *85,* 684–686. doi:10.1063/1.1775289
6. Bunn, C. W. *Proc. Phys. Soc., London* **1935,** *47,* 835–842. doi:10.1088/0959-5309/47/5/307
7. Feng, Y.; Wu, F.; Jiang, J.; Zhu, J.; Fodjouong, G. J.; Meng, G.; Xing, Y.; Wang, W.; Huang, X. *J. Alloys Compd.* **2013,** *581,* 610–615. doi:10.1016/j.jallcom.2013.07.171
8. Tan, W. K.; Lockman, Z.; Raza, K. A.; Kawamura, G.; Muto, H.; Matsuda, A. *Int. J. Energy Res.* **2013,** *37,* 1992–2000. doi:10.1002/er.3026
9. Pietruszka, R.; Luka, G.; Witkowski, B. S.; Kopalko, K.; Zielony, E.; Bieganski, P.; Placzek-Popko, E.; Godlewski, M. *Thin Solid Films* **2013,** in press. doi:10.1016/j.tsf.2013.10.110
10. Liu, C. P.; Hung, Y. T. *Thin Solid Films* **2005,** *492,* 269–274. doi:10.1016/j.tsf.2005.06.030
11. Ahmad, M.; Hong, Z. L.; Ahmed, E.; Khalid, N. R.; Elhissi, A.; Ahmad, W. *Ceram. Int.* **2013,** *39,* 3007–3015. doi:10.1016/j.ceramint.2012.09.079
12. Navarro, S.; Fenoll, J.; Vela, N.; Ruiz, E.; Navarro, G. *J. Hazard. Mater.* **2009,** *172,* 1303–1310. doi:10.1016/j.jhazmat.2009.07.137
13. Pietruszka, R.; Luka, G.; Kopalko, K.; Zielony, E.; Bieganski, P.; Placzek-Popko, E.; Godlewski, M. *Mater. Sci. Semicond. Process.* **2013,** in press. doi:10.1016/j.mssp.2013.11.026
14. Yin, X.; Que, W.; Fei, D.; Shen, F.; Guo, Q. *J. Alloys Compd.* **2012,** *524,* 13–21. doi:10.1016/j.jallcom.2012.02.052
15. Chen, Y.; Bagnall, D. M.; Koh, H.-j.; Park, K.-t.; Hiraga, K.; Zhu, Z.; Yao, T. *J. Appl. Phys.* **1998,** *84,* 3912–3918. doi:10.1063/1.368595
16. Guo, X.-l.; Choi, J.-H.; Tabata, H.; Kawai, T. *Jpn. J. Appl. Phys., Part 1* **2001,** *40,* 177–180. doi:10.1143/JJAP.40.L177
17. Ryu, Y. R.; Lee, T. S.; Leem, J. H.; White, H. W. *Appl. Phys. Lett.* **2003,** *83,* 4032–4034. doi:10.1063/1.1625787
18. Pan, F.; Song, C.; Liu, X. J.; Yang, Y. C.; Zeng, F. *Mater. Sci. Eng., R* **2008,** *62,* 1–35. doi:10.1016/j.mser.2008.04.002
19. Mandal, S. K.; Das, A. K.; Nath, T. K.; Karmakar, D. *Appl. Phys. Lett.* **2006,** *89,* 144105. doi:10.1063/1.2360176
20. Dietl, T.; Ohno, H. *MRS Bull.* **2003,** *28,* 714–719. doi:10.1557/mrs2003.211
21. Parkin, S.; Jiang, X.; Kaiser, C.; Panchula, A.; Roche, K.; Samant, M. *Proc. IEEE* **2003,** *91,* 661. doi:10.1109/JPROC.2003.811807
22. Lee, W.; Shin, S.; Jung, D.-R.; Kim, J.; Nahm, C.; Moon, T.; Park, B. *Curr. Appl. Phys.* **2012,** *12,* 628–631. doi:10.1016/j.cap.2011.09.008
23. Bowen, A.; Li, J.; Lewis, J.; Sivaramakrishnan, K.; Alford, T. L.; Iyer, S. *Thin Solid Films* **2011,** *519,* 1809–1816. doi:10.1016/j.tsf.2010.10.019
24. Gordillo, G.; Grizalez, M.; Moreno, L. C.; Landazábal, F. *Phys. Status Solidi B* **2000,** *220,* 215–219. doi:10.1002/1521-3951(200007)220:1<215::AID-PSSB215>3.0.CO;2-8
25. Cho, H. J.; Lee, S. U.; Hong, B.; Shin, Y. D.; Ju, J. Y.; Kim, H. D.; Park, M.; Choi, W. S. *Thin Solid Films* **2010,** *518,* 2941–2944. doi:10.1016/j.tsf.2009.10.130
26. Dagamseh, A. M. K.; Vet, B.; Tichelaar, F. D.; Sutta, P.; Zeman, M. *Thin Solid Films* **2008,** *516,* 7844–7850. doi:10.1016/j.tsf.2008.05.009
27. Appell, D. *Nature* **2002,** *419,* 553–555. doi:10.1038/419553a
28. Samuelson, L. *Mater. Today* **2003,** *6,* 22–31. doi:10.1016/S1369-7021(03)01026-5
29. Duan, X.; Huang, Y.; Cui, Y.; Wang, J.; Lieber, C. M. *Nature* **2001,** *409,* 66–69. doi:10.1038/35051047
30. Djurišić, A. B.; Ng, A. M. C.; Chen, X. Y. *Prog. Quantum Electron.* **2010,** *34,* 191–259. doi:10.1016/j.pquantelec.2010.04.001
31. Wang, Z. L. *Adv. Mater.* **2000,** *12,* 1295–1298. doi:10.1002/1521-4095(200009)12:17<1295::AID-ADMA1295>3.0.CO;2-B
32. Hu, J.; Odom, T. W.; Lieber, C. M. *Acc. Chem. Res.* **1999,** *32,* 435–445. doi:10.1021/ar9700365
33. Yang, P.; Lieber, C. M. *Science* **1996,** *273,* 1836–1840. doi:10.1126/science.273.5283.1836
34. Morales, A. M.; Lieber, C. M. *Science* **1998,** *279,* 208–211. doi:10.1126/science.279.5348.208

35. Peng, X.; Wickham, J.; Alivisatos, A. P. *J. Am. Chem. Soc.* **1998,** *120,* 5343–5344. doi:10.1021/ja9805425
36. Witkowski, B. S.; Wachnicki, L.; Gieraltowska, S.; Dłuzewski, P.; Szczepanska, A.; Kaszewski, J.; Godlewski, M. *Int. J. Nanotechnol.* **2014,** in press.
37. Baruah, S.; Dutta, J. *Sci. Technol. Adv. Mater.* **2009,** *10,* 013001. doi:10.1088/1468-6996/10/1/013001
38. Baruah, S.; Dutta, J. *J. Cryst. Growth* **2009,** *311,* 2549–2554. doi:10.1016/j.jcrysgro.2009.01.135
39. Degen, A.; Kosec, M. *J. Eur. Ceram. Soc.* **2000,** *20,* 667–673. doi:10.1016/S0955-2219(99)00203-4
40. Luka, G.; Krajewski, T.; Wachnicki, L.; Witkowski, B.; Lusakowska, E.; Paszkowicz, W.; Guziewicz, E.; Godlewski, M. *Phys. Status Solidi A* **2010,** *207,* 1568–1571. doi:10.1002/pssa.200983709
41. Godlewski, M.; Guziewicz, E.; Kopalko, K.; Łuka, G.; Łukasiewicz, M. I.; Krajewski, T.; Witkowski, B. S.; Gierałtowska, S. *Low Temp. Phys.* **2011,** *37,* 235–241. doi:10.1063/1.3570930
42. Luka, G.; Krajewski, T. A.; Witkowski, B. S.; Wisz, G.; Virt, I. S.; Guziewicz, E.; Godlewski, M. *J. Mater. Sci.: Mater. Electron.* **2011,** *22,* 1810–1815. doi:10.1007/s10854-011-0367-0
43. Stakhira, P. I.; Pakhomov, G. L.; Cherpak, V. V.; Volynyuk, D.; Luka, G.; Godlewski, M.; Guziewicz, E.; Hotra, Z. Yu. *Cent. Eur. J. Phys.* **2010,** *8,* 798–803. doi:10.2478/s11534-009-0159-9

License and Terms

The definitive version of this article is the electronic one which can be found at:
doi:10.3762/bjnano.5.17

Beilstein Journal
of Nanotechnology

Modeling and optimization of atomic layer deposition processes on vertically aligned carbon nanotubes

Nuri Yazdani[1,2], Vipin Chawla[3], Eve Edwards[3], Vanessa Wood[2],
Hyung Gyu Park*[1] and Ivo Utke*[3]

Full Research Paper

Open Access

Address:
[1]Nanoscience for Energy Technology and Sustainability, Department of Mechanical and Process Engineering, ETH Zürich, Zürich CH-8092, Switzerland, [2]Laboratory for Nanoelectronics, Department of Information Technology and Electrical Engineering, ETH Zürich, Zürich CH-8092, Switzerland and [3]Laboratory for Mechanics of Materials and Nanostructures, EMPA, Thun CH-3602, Switzerland

Email:
Hyung Gyu Park* - parkh@ethz.ch; Ivo Utke* - ivo.utke@empa.ch

* Corresponding author

Keywords:
atomic layer deposition; vertically aligned carbon nanotubes; continuum diffusion model; conformal coating guidelines; titania, TiO2

Beilstein J. Nanotechnol. **2014,** *5,* 234–244.
doi:10.3762/bjnano.5.25

Received: 29 September 2013
Accepted: 12 February 2014
Published: 05 March 2014

This article is part of the Thematic Series "Energy conversion applications of atomic layer deposition".

Guest Editor: J. Bachmann

Abstract

Many energy conversion and storage devices exploit structured ceramics with large interfacial surface areas. Vertically aligned carbon nanotube (VACNT) arrays have emerged as possible scaffolds to support large surface area ceramic layers. However, obtaining conformal and uniform coatings of ceramics on structures with high aspect ratio morphologies is non-trivial, even with atomic layer deposition (ALD). Here we implement a diffusion model to investigate the effect of the ALD parameters on coating kinetics and use it to develop a guideline for achieving conformal and uniform thickness coatings throughout the depth of ultra-high aspect ratio structures. We validate the model predictions with experimental data from ALD coatings of VACNT arrays. However, the approach can be applied to predict film conformality as a function of depth for any porous topology, including nanopores and nanowire arrays.

Introduction

Recent advances in the synthesis and processing of carbon nanotubes (CNTs) have enabled the prospect of their integration into existing technologies that exploit the high surface area of mesoporous ceramic films [1]. Over the last 10 years, ceramic coated CNTs have been applied in battery [2-5] and supercapacitor electrodes [6-12], fuel cells [13], and sensors

[14-17]. For many of the proposed applications of these CNT/ceramic hybrids, the performances of the devices depend crucially on the thickness and conformality of the ceramic coating of the CNTs. Atomic layer deposition (ALD) is a highly attractive option for coating CNTs because it enables a wide range of ceramics and metals to be deposited conformally on arbitrary surface topologies with precise control of layer thickness [1,18].

However, vertically aligned CNT (VACNT) arrays present a complex surface and topology for ALD that requires new processing strategies. First, the graphitic surface of a pristine CNT is chemically inert, and provides no bonding sites for the nucleation of ceramics, which prevents the conformal coating of the CNT without prior functionalization [19-24]. In practice, however, chemical vapor deposition (CVD) grown CNTs are prone to a sufficient density of surface defect sites to allow for the nucleation of the ceramic at discrete points along the surface of the CNT. The ceramic then grows from these nucleation sites until it overlaps with ceramic from a neighboring site. In this way, a conformal coating forms on the surface of the nanotube [16,25-27]. While the number of cycles required to arrive at a state of complete coverage depends on the density of defect sites, 50–100 cycles are typically sufficient for a conformal coating of CVD-grown CNTs.

Second, the vertically aligned nature of the CNT arrays presents a challenge for conformal coatings of uniform thickness. The penetration of the deposited oxide into the VACNTs is often limited as illustrated in Figure 1. Under the pressure and temperature conditions of typical ALD processes, gas phase collisions among the precursor molecules in the pores of VACNT structure are far less frequent than collisions between a precursor molecule and a CNT surface. This corresponds to the free molecular regime of gas transport (i.e., Knudsen diffusion) [28,29]. Furthermore, even VACNTs of moderate lengths have very large surface areas that require a large number of precursor molecules for a monolayer coating, such that either large precursor concentrations or very long exposure times are needed to conformally coat all the way down to the bottom of the array [30]. An optimization of the ALD process can ensure the desired depositions while minimizing the use of precursor material and the deposition time [16,27]. Here we develop and validate a model to perform such optimization.

Previous modeling [31-36] of the penetration of metal oxides into nanometer-sized pores has demonstrated that the factor limiting the penetration depth of the oxide is the depth, to which the precursor molecules can diffuse in the pores and adsorb on the pore surface during the precursor exposure/adsorption step of the ALD process. The penetration depth of the oxide into the pores, x_p, was shown to be proportional to the pore radius, $x_\mathrm{p} \propto r$ the square root of the precursor exposure time, $x_\mathrm{p} \propto \sqrt{t}$ and the square root of the precursor concentration in the chamber, $x_\mathrm{p} \propto \sqrt{n_\mathrm{chamber}}$ [31-33]. For porous media, the radius of the pores will decrease from cycle to cycle, which further hinders a diffusion of the precursor molecules. In addition, in the case of VACNTs, not only will diffusion be increasingly hindered because of the cycle-to-cycle increase of the CNT radii, but the total surface area will also increase, which means that more and more precursor molecules are required to completely cover the CNTs with adsorbed precursors, as illustrated in Figure 1. Understanding how the penetration depth of the precursor varies with the ALD process parameters and radii of the CNTs could thus enable deposition recipes to be optimized to obtain a ceramic with uniform thickness to a desired penetration depth.

To this end, we develop a model that treats both the diffusion of precursor molecules and their adsorption on VACNTs during the precursor pulse. Assuming rapid adsorption of the precursor molecules, this full diffusive model can be approximated by a

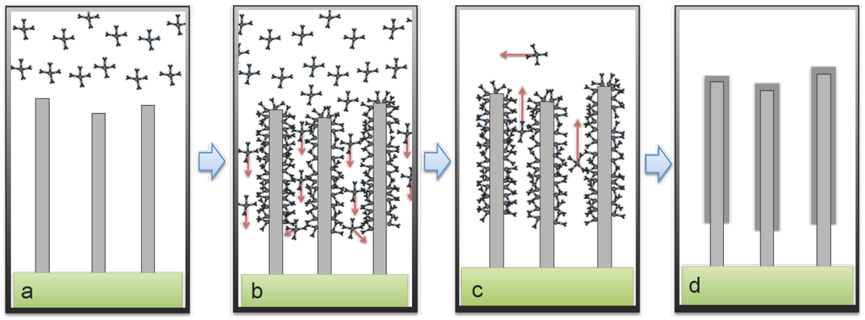

Figure 1: Illustration of one ALD cycle on a VACNT array. Upon exposure to the precursor gas (a: bulk gas diffusion), precursor molecules diffuse into the CNT array and adsorb onto available sites (b: confined diffusion and adsorption). After the defined precursor exposure time, purging of the ALD chamber removes unreacted precursor molecules from the chamber (c). After the oxidization pulse, a thin layer of oxide is formed on the surface (d).

close form expression, equivalent to the well-established Gordon model [32]. We use the full diffusion model to investigate the effects of the various ALD process settings and physical parameters of the CNTs on the oxide growth kinetics during a single ALD cycle. Multi-cycle ALD processes are simulated, and reveal that non-uniform coating thickness as a function of depth results from the decrease in the penetration depth from cycle to cycle. The model predicts that if the precursor exposure times are scaled as a function of cycle number, uniform depositions can be achieved. Finally, we experimentally confirm our model predictions.

Results and Discussion

Modeling of precursor exposure/adsorption

When performing ALD on structures with a high aspect ratio, one process that limits the uniform coating could be the relatively slow diffusion of the precursor molecules within the structures. At the same time, the large surface area of the high-aspect-ratio structure requires a large number of precursor molecules such that the location and rate of adsorption is also critical to the coating kinetics. Therefore to understand how ALD process parameters influence the coatings of high aspect ratio structures, we develop a model based on a continuum diffusion approach that also takes into account adsorption of precursor molecules.

In this model, we exclude the discrete nucleation phase of the ALD process on the CNTs. That is, we assume that a layer of ceramic is already deposited on the nanotubes, which may typically require 50–100 ALD cycles to achieve. The model may thus underestimate the penetration depth of the ceramic for a low number of ALD cycles, but it should be qualitatively accurate for high cycle numbers.

Diffusion model of the precursor adsorption kinetics

In ALD, the precursor is pulsed into the chamber diluted in a carrier gas, such as N_2 or Ar. An overall chamber pressure of the order of several millibar are typical for ALD processes, with precursor number densities ranging from 10^{13}–10^{15} cm^{-3}. As the mass of the precursor molecules, m_p, and their molecular diameter are in general much larger than those of the carrier gases, the diffusion of the precursor molecules within the VACNT array is far slower than that of the carrier gas. Here, we assume a mechanical equilibrium between the porous region of the CNT arrays and the rest of the ALD chamber such that total pressures within and outside the CNT arrays are quickly equilibrated as a result of fast distribution of the carrier gas. We can thus model the transport kinetics as a diffusive process of the precursor species in a porous medium initially filled with the carrier species.

Assuming a negligible variation of the precursor partial pressure in the transverse directions of the CNT arrays, we can represent the precursor number density per unit volume, $n(x,t)$, as a function of time, t, and the distance into the CNT array, x. The function $n(x,t)$ obeys the following transport equation:

$$\frac{\partial n(x,t)}{\partial t} = \frac{\partial}{\partial x}\left(D(x)\frac{\partial n(x,t)}{\partial x} \right) - \alpha(x,t), \qquad (1)$$

where $D(x)$ is the diffusion coefficient of the precursor molecules inside the CNT array, and $\alpha(x,t)$ is a loss term that corresponds to the adsorption of precursor molecules onto available bonding sites and their subsequent chemical bond formation (chemisorption).

The adsorption rate per unit volume, α, is modeled to be proportional to the number of precursor molecules striking the CNT surface per unit area, i.e., the impingement rate, $I(x,t)$, to the fraction of the CNT surface area available for the precursor adsorption, $f(x,t)$, and to the probability, at which an impinging precursor molecule adsorbs and reacts on an adsorption site, i.e., the reactive sticking coefficient, Γ:

$$\alpha(x,t) = I(x,t)\Delta A_\text{s}(x) f(x,t)\Gamma , \qquad (2)$$

where ΔA_s (cm^{-1}) is the surface area per unit volume of the CNT array. We take the impingement rate from gas kinetics theory, in which for an ideal gas,

$$I(x,t) = n(x,t)\sqrt{\frac{k_\text{B}T}{2\pi m_\text{p}}} . \qquad (3)$$

The fraction of the surface area that is available for adsorption is given by

$$f(x,t) = \frac{\Delta A_\text{s} - n_\text{ads}(x,t)/\sigma_\text{p}}{\Delta A_\text{s}} , \qquad (4)$$

where σ_p is the maximum number of adsorbed precursor molecules per unit area, and

$$n_\text{ads}(x,t) = \int_{t=0}^{t} \alpha(x,t)dt \qquad (5)$$

is the total number of precursor molecules per unit volume already adsorbed at time t.

Substituting Equation 2 into Equation 1, we simulate Equation 1 by using a finite difference method. Both time and space are discretized into points separated by Δt and Δx respectively,

$$\begin{aligned} &x \to x_i\,, \qquad x_{N_x} = L\,, \qquad L/N_x = \Delta x\,, \\ &t \to t_j\,, \qquad t_{N_t} = t_{\text{total}}\,, \quad t_{\text{total}}/N_t = \Delta t\,, \\ &n(x,t) \to n_i^j \end{aligned} \tag{6}$$

Since the adsorption kinetics typically proceed at a much faster rate than the diffusion of precursor molecules, we also decouple Equation 1 in the simulation into two parts. To update the simulation parameters at time t_{j+1}, the diffusion process is advanced first in the simulation, generating a concentration profile given by $n_i^{j'}$. The adsorption kinetics are then solved explicitly over the period $t_j \to t_{j+1}$ and n_i^{j+1} and $N_{\text{ads},i}^{j+1}$ are then computed accordingly, as described in more detail below. A flow chart of the simulation of one ALD cycle is shown in Figure 2.

For the precursor pulse portion of the ALD cycle, we use the initial condition that the CNT array is devoid of any precursor molecules, $n_i^0 = 0$. The system has a closed boundary at $x = L$ (the bottom of the VACNT array), which is implemented by a first order Neumann boundary condition, $dn/dx = 0$. At $x = 0$ (the top of the VACNT array) we apply $n_0^t = n_{\text{chamber}}$, where n_{chamber} is the concentration of the precursor molecules in the ALD chamber. For the purge portion of the ALD cycle, we take as the initial condition the final state of the system at the end of the precursor pulse portion. The boundary condition at the top of the CNT array ($x = 0$) is also changed to reflect that there are no precursor molecules in the chamber ($n_0^t = 0$).

Precursor adsorption kinetics

At each time step t_j, the amount of precursor molecules that adsorb onto vacant adsorption sites during the time $t_j \to t_{j+1}$ is calculated for each discrete void volume element ΔV_i, where $\Delta V_i \equiv \Delta V \cdot \Delta x$, at position x_i. We let $N_i(t)$ represent the number of precursor molecules per projected area in ΔV_i, continuously in time from $t_j \to t_{j+1}$, where $N_i(t_j) = n_i^{j'} \Delta V_i$. According to Equation 2, $N_i(t)$ should satisfy:

$$\begin{aligned} \frac{\partial N_i(t)}{\partial t} &= -\frac{\Gamma}{\sigma_p \Delta V_i} \sqrt{\frac{k_B T}{2\pi m_p}} \\ &\quad \times N_i(t)\left(\sigma_p \Delta A_i - N_{\text{ads},i}^j - \left(n_i^{j'} \Delta V_i - N_i(t)\right)\right), \end{aligned} \tag{7}$$

where $\Delta A_i \equiv \Delta A_s \cdot \Delta x$. Solving Equation 7 and applying the initial condition $l = \left(\sqrt{2}\pi d^2 n\right)^{-1}$ gives

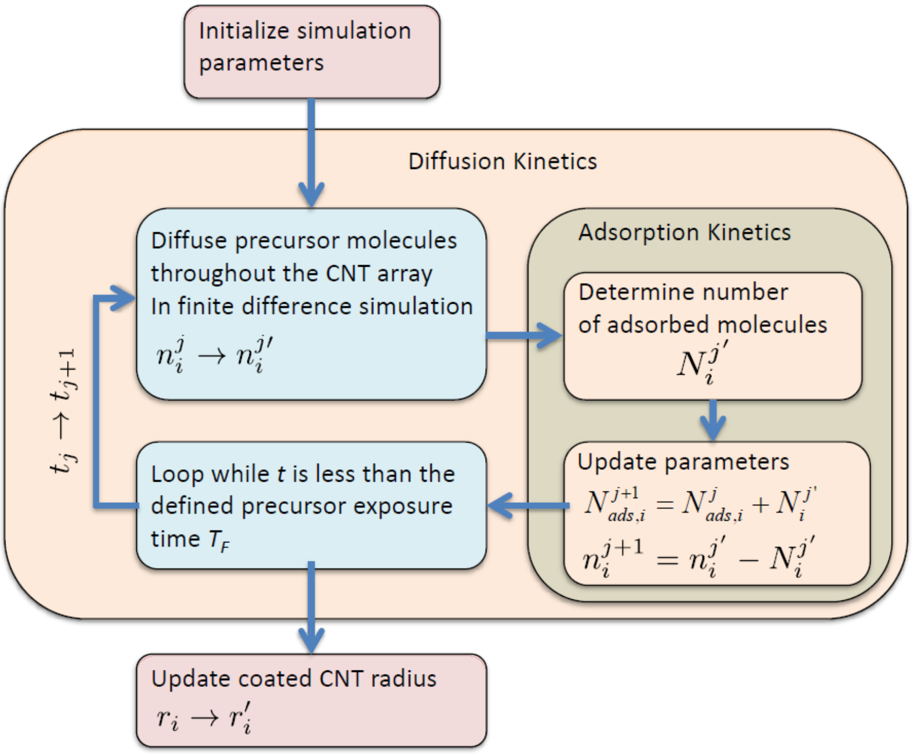

Figure 2: Flow chart of the precursor exposure/adsorption simulation for one ALD cycle.

$$N_i(t) = \frac{n_i^{j\prime}\Delta V\left(\sigma_{\mathrm{p}}\Delta A_i - N_{\mathrm{ads},i}^{j} - n_i^{j\prime}\Delta V\right)\exp\left[-\frac{\Gamma}{\sigma_{\mathrm{p}}\Delta V_i}\sqrt{\frac{k_{\mathrm{B}}T}{2\pi m_{\mathrm{p}}}}N_i(t)\left(\sigma_{\mathrm{p}}\Delta A_i - N_{\mathrm{ads},i}^{j} - n_i^{j\prime}\Delta V\right)\left(t-t_j\right)\right]}{\sigma_{\mathrm{p}}\Delta A_i - N_{\mathrm{ads},i}^{j} - n_i^{j\prime}\Delta V\exp\left[-\frac{\Gamma}{\sigma_{\mathrm{p}}\Delta V_i}\sqrt{\frac{k_{\mathrm{B}}T}{2\pi m_{\mathrm{p}}}}N_i(t)\left(\sigma_{\mathrm{p}}\Delta A_i - N_{\mathrm{ads},i}^{j} - n_i^{j\prime}\Delta V\right)\left(t-t_j\right)\right]}. \quad (8)$$

Equation 8 is then used to calculate the total amount of precursor molecules that are adsorbed in the volume ΔV_i, giving

$$n_i^{j+1} = \frac{N_i\left(t_{j+1}\right)}{\Delta V_i},\ N_{\mathrm{ads},i}^{j+1} = N_{\mathrm{ads},i}^{j} + n_i^{j\prime}\Delta V_i - N_i\left(t_{j+1}\right). \quad (9)$$

Diffusion coefficient

From the kinetic theory of an ideal gas, the mean free path is given by $l = \left(\sqrt{2}\pi d^2 n\right)^{-1}$, where d is the molecular diameter, and n is the gas number density. Most precursor molecules have diameters in the range of 10^{-8}–10^{-7} cm, while precursor concentrations can range anywhere from 10^{13} cm^{-3} to 10^{15} cm^{-3} with chamber pressures typically of the order of a few millibar. Even assuming partial pressures of the precursor molecule of up to 10 mbar, the mean free path calculated from kinetic theory (1.5×10^{-4} cm) is more than an order of magnitude greater than the average distance between the CNTs of the vertical array, which is typically smaller than 10^{-5} cm. The gas transport of this system is thus in the regime of free molecular flow, in which the effective diffusion coefficient for this porous medium is described by Knudsen diffusivity,

$$D_{\mathrm{k}} = d_{\mathrm{pore}}\sqrt{\frac{8k_{\mathrm{B}}T}{9\pi m_{\mathrm{p}}}}, \quad (10)$$

where d_{pore} is the average pore size of the porous medium. As a first order approximation, we use Equation 10 and replace d_{pore} with the average spacing between the CNTs in the array. If the CNTs have an areal density of σ_{CNT} (cm^{-2}) and the radius r, the effective diffusion coefficient will be given by

$$D_{\mathrm{k}} = \left(\frac{1}{\sqrt{\sigma_{\mathrm{CNT}}}} - 2r\right)\sqrt{\frac{8k_{\mathrm{B}}T}{9\pi m_{\mathrm{p}}}}. \quad (11)$$

Simulation results

Table 1 summarizes our estimates for the physical parameters of the CNTs and precursor molecules as well as the ALD run parameters that were used in the simulations. Values for the precursor parameters are estimated from titanium isopropoxide. The precursor surface adsorption density, σ_{p}, is estimated to be $1/V_{\mathrm{AB2}}^{2/3}$, where V_{AB2} is the volume of a deposited oxide unit, here determined by the dimensions of the titanium dioxide unit cell.

Table 1: Default parameters for the simulation.

simulation parameter	value
height of the VACNTs	10^{-2} cm
initial average CNT diameter	10^{-6} cm
areal density of the CNTs (σ_{CNT})	10^{10} cm^{-2}
diameter of precursor molecule	10^{-7} cm
mass of precursor molecule (m_{p})	4.7×10^{-22} g
precursor surface adsorption density (σ_{p})	10^{14} cm^{-2}
volume per oxide unit (AB_2)	1.4×10^{-22} cm^3
concentration of precursor vapor (n_{chamber})	5×10^{15} cm^{-3}
reactive sticking coefficient	0.01
ALD deposition temperature	500 K
precursor exposure time	50 ms
purge time	50 ms

By using the parameters defined in Table 1, the concentration of the precursor as a function of the depth within the VACNT array is plotted at various times during the exposure to the precursor of 50 ms in Figure 3a. Immediately after its introduction into the ALD chamber, the precursor can easily penetrate the CNT arrays down to 10 µm. The penetration becomes limited, however, to 30–40 µm even after the full 50 ms of exposure, which is attributed to decreasing flux of the penetrating precursor as a function of depth into the array, $\partial n/\partial x$.

In Figure 3b, the thickness of oxide coated per cycle is plotted as a function of depth for various reactive sticking coefficients ranging from 10^{-4} to 1. For relatively large coefficients (from about 10^{-2} to 1), the penetration depth is not greatly affected by the reactive sticking coefficient, which indicates that the impingement rate of the precursor molecules on the CNT surface is large compared to the rate, at which they diffuse into the CNT array. In Figure 3c the thickness of oxide coated per cycle is plotted with respect to depth for various precursor exposure times. The thickness of the coating deep inside the CNT array increases with the exposure time, as the precursor molecules have more time to diffuse down to available adsorption sites.

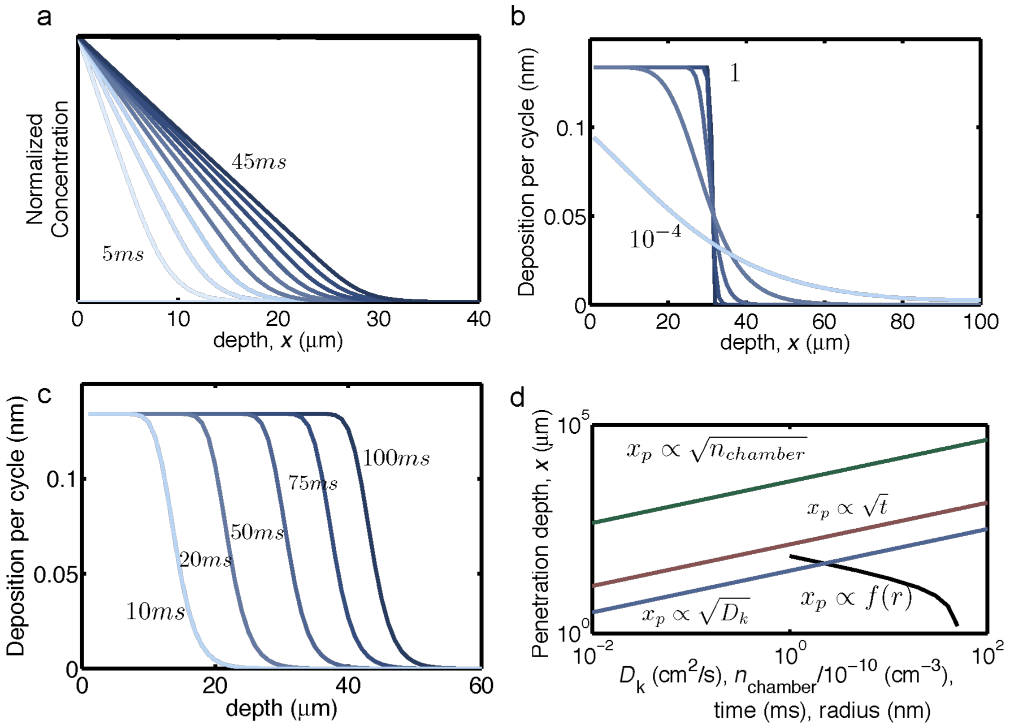

Figure 3: Results of the precursor adsorption kinetics simulation while using the parameters defined in Table 1. The concentration of precursor molecules as a function of depth at several time steps (0 to 50 ms, with 5 ms intervals) within the CNT array is plotted in (a). The effect of the reactive sticking coefficient is demonstrated in (b), where the deposited oxide thickness per cycle is plotted versus the depth in the array, after 50 ms exposure. In (c) the effect of the precursor exposure time is plotted. In (d), the penetration depth of the oxide is plotted as a function of the precursor concentration, exposure time, Knudsen diffusion coefficient, and radius of the CNTs with a reactive sticking coefficient of 10^{-2}. The penetration depth clearly depends on the square root of the precursor concentration, exposure time, and diffusion coefficient, but has a nontrivial dependence on the radius of the CNTs.

The maximum growth per cycle of about 0.13 nm is rather large compared to typical ALD deposition rates for titanium dioxide. In principle, one can modify the precursor surface adsorption density to achieve more reasonable deposition rates. The two extreme limits for the maximum growth per cycle would be the limits, at which the density is either determined by the oxide volume, $\sigma_p = 1/V_{AB2}^{2/3}$ as used for the data above, or by the diameter of the precursor molecules, $\sigma_p = 1/\pi r_p^2$ where r_p is the radius of the precursor molecule.

The penetration depth of the oxide, x_p (defined as the depth, at which the thickness of the coating is equal to half of its maximum value), is characterized while varying the exposure time, precursor concentration, diffusion coefficient, and the radius of the CNTs (Figure 3d). The penetration depth is found to be proportional to the square root of the exposure time, the precursor concentration, and the diffusion coefficient, which is consistent with previous studies [32,33]. Interestingly, the penetration depth shows a non-trivial dependence on the radius of the CNTs. The radius of the CNTs has an impact on two parameters in the diffusion/absorption process. As the radius of the CNTs is increased, the gap distance between the CNTs decreases, which reduces the diffusion coefficient given in Equation 11. In addition, as the radius of the CNTs increase, the overall surface area per unit volume, ΔA_s, also increases, such that more precursor molecules are adsorbed per unit length. The combination of slower diffusion and increased demand of precursor supply to fully coat the surface has a strong impact on the extent, to which the oxide can penetrate into the CNT array.

Approximation to the model assuming rapid adsorption

Under the condition that the adsorption rate of precursor molecules is much faster than the diffusive transport through the CNT array and with a reactive sticking coefficient close to one, it can be assumed that all the precursor molecules adsorb at the first encounter with an unoccupied adsorption site [32]. In this scenario, the adsorption sites are filled up linearly in the x direction, and the precursor concentration is zero at x_p, since all of the precursor molecules arriving at x_p are immediately adsorbed. Furthermore, the precursor diffusion flux throughout the array up to x_p must be constant, since precursor molecules are adsorbing at a fixed rate at x_p. Thus, given that the concentration at $x = 0$ is fixed at $n_{chamber}$, Fick's law gives the precursor diffusion flux as

$$J\left(x,t\right) = D_{\mathrm{k}} \frac{n_{\mathrm{chamber}}}{x_{\mathrm{p}}}, \tag{12}$$

or in terms of the number of precursor molecules per unit projected area, *N*,

$$\frac{dN}{dt} = D_{\mathrm{k}} \frac{n_{\mathrm{chamber}} \Delta V}{x_{\mathrm{p}}}. \tag{13}$$

As precursor molecules continuously flow into the CNT array, the change in x_p can be expressed as

$$\frac{dx_{\mathrm{p}}}{dt} = \frac{dN/dt}{\sigma_{\mathrm{p}} \Delta A_{\mathrm{s}}}. \tag{14}$$

Substituting Equation 13 into Equation 14 and a subsequent integration gives

$$x_{\mathrm{p}} = \sqrt{\frac{2tD_{\mathrm{k}} n_{\mathrm{chamber}} \Delta V}{\sigma_{\mathrm{p}} \Delta A_{\mathrm{s}}}}. \tag{15}$$

This result is equivalent to the expression given by Gordon et al. [32] for tubular pores taking Equation 10 for D_{k} and considering that

$$\Delta A_{\mathrm{s}} = \sigma_{\mathrm{pore}} 2\pi r,\ \Delta V = \sigma_{\mathrm{pore}} \pi r^2, \tag{16}$$

under the condition that the pore radius, *r*, is much smaller than the depth of the pores. Equation 15 thus gives an analytical approximation for the oxide penetration depth valid for any porous topology with high aspect ratio provided that the reactive sticking is close to one ($\Gamma \approx 1$). It only requires the determination of (1) an effective diffusion coefficient related to the porosity, constrictivity, and tortuosity of the porous medium and of (2) the surface area and void volume per unit volume.

For an array of CNTs the surface area and void volume per unit volume are given by

$$\Delta A_{\mathrm{s}} = \sigma_{\mathrm{CNT}} 2\pi r,\ \Delta V = 1 - \sigma_{\mathrm{CNT}} \pi r^2. \tag{17}$$

Substituting Equation 16 and Equation 11 into Equation 15 then gives the final expression for the penetration depth of one ALD cycle,

$$x_{\mathrm{p}} = \left(\frac{8k_{\mathrm{B}}T}{9\pi m_{\mathrm{p}}}\right)^{1/4} \sqrt{\frac{t \cdot n_{\mathrm{chamber}}}{\sigma_{\mathrm{p}}} \left(\frac{1}{\sqrt{\sigma_{\mathrm{CNT}}}} - 2r\right) \frac{\left(1 - \sigma_{\mathrm{CNT}} \pi r^2\right)}{\pi r \sigma_{\mathrm{CNT}}}}. \tag{18}$$

This simplified expression is in agreement with the simulations of the full diffusion model above. In Figure 4, the penetration depth of the oxide is plotted by using both the simulation and the simplified expression while using the parameters in Table 1 with varying precursor adsorption site densities. The results when using Equation 18 are in agreement with the simulation output.

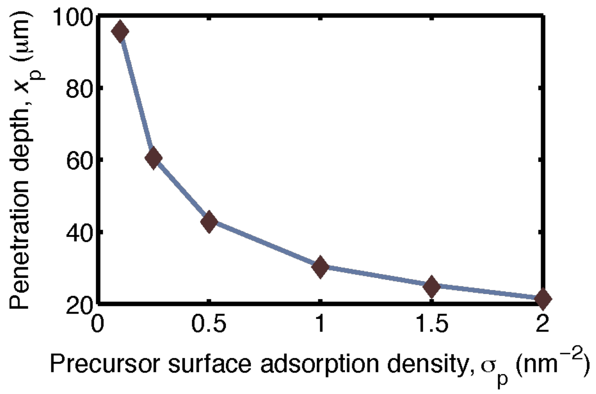

Figure 4: Comparison of the simplified model (Equation 18) and the simulation of the full diffusion model (solid line) while using a reactive sticking coefficient Γ = 1, as function of the varying precursor surface adsorption density. The penetration depths given by both methods are in agreement.

Multiple cycle growth kinetics

The dependence of the penetration depth for the precursor adsorption on the radius of the CNTs (Equation 18) implies that the depth of the ALD deposition will decrease from cycle to cycle. Depositions on VACNT arrays that utilize an ALD process with fixed deposition parameters typically display a decreasing coating thickness as a function of the depth within the array. From the results of our modeling, it is clear that this depth profile of the coating predominantly occurs not through an uneven deposition profile from each individual cycle but rather from a cycle-to-cycle variation in the penetration depth of the oxide coating. In Figure 5a, the oxide thickness with respect to depth is plotted according to results of the multi-cycle ALD simulation. These findings suggest that, in order to achieve truly uniform coatings on a high-aspect-ratio structure, one must scale the ALD parameters from cycle to cycle. Although changing the precursor concentration and temperature is generally impractical, the precursor exposure time can be changed rather easily. If cycle zero has an exposure time, t_0, with CNTs of radius, r_0, the subsequent exposure times required to always reach the same penetration depth are given as:

$$t_k = \frac{\left(r_0 + k\Delta r\right)\left(\frac{1}{\sqrt{\sigma_{\mathrm{CNT}}}} - 2r_0\right)\left(1 - \sigma_{\mathrm{CNT}}\pi r_0^2\right)}{r_0\left(\frac{1}{\sqrt{\sigma_{\mathrm{CNT}}}} - 2\left(r_0 + k\Delta r\right)\right)\left(1 - \sigma_{\mathrm{CNT}}\pi\left(r_0 + k\Delta r\right)^2\right)} t_0, \quad (19)$$

where Δr is the thickness of oxide deposited per cycle, and k is the cycle number. This scaling is simulated, and shows (Figure 5b) a more uniform coating thickness as a function of depth compared to the coating obtained with a constant precursor exposure time (Figure 5a). This result suggests a clear ALD process protocol to achieve a uniform coating of high aspect ratio structures.

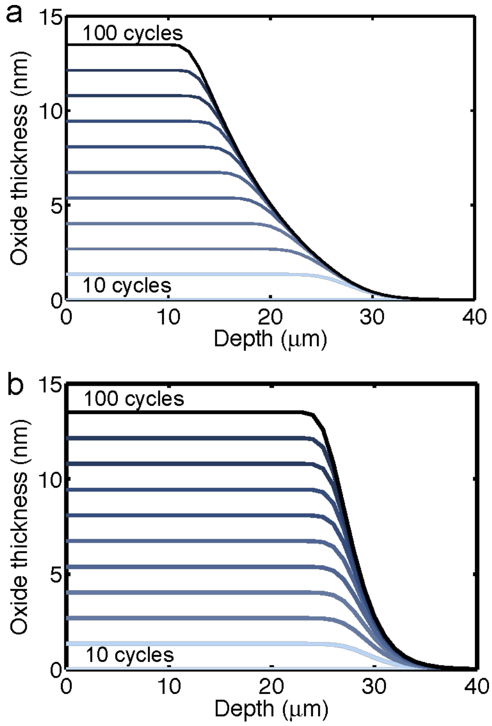

Figure 5: Plot of deposited oxide thickness with respect to the VACNT depth for a multi-cycle ALD process, determined by the model with the parameters in Table 1. (a) Fixed precursor exposure time (50 ms). (b) Scaled exposure time according to Equation 19.

Experimental

To qualitatively compare the results of the modeling to actual depositions, VACNT samples are prepared and coated with titanium dioxide and aluminum oxide. To synthesize our VACNTs, a 3-nm-thick catalyst layer of iron on top of a 20-nm-thick layer of aluminum is deposited through electron beam evaporation onto a silicon wafer. The VACNTs are then grown by chemical vapor deposition in a cold-wall CVD system. The catalyst-covered substrate is annealed for 10 min at 725 °C in a flowing environment of Ar (400 sccm) and H_2 (600 sccm) in order to reduce the iron oxide to metallic iron. After this reduction annealing, C_2H_4 (250 sccm) as a carbon precursor is supplied for 5 min, which results in the growth of vertically aligned multiwalled CNTs, 50–90 μm in height. By using scanning electron microscopy (SEM), the distribution of CNT diameters is measured, and the bare CNT radii are found to be 6.3 ± 0.2 nm. Titanium dioxide is deposited on the CNTs by using a custom-built ALD system. The depositions are performed at 225 °C with a precursor mixture of titanium isopropoxide ($\mathrm{Ti\{OCH(CH_3)_2\}_4}$, TTIP) heated to 90 °C and water vapor at 40 °C. One ALD cycle consists of a 5 s long pulse and 40 s long hold of TTIP, followed by a 0.5 s long pulse and 40 s long hold of water vapor, with 60 s long Ar purges in between the two pulses. Aluminum oxide is deposited on the CNTs by using a Picosun ALD system. The depositions are performed at 200 °C. Trimethylaluminum ($\mathrm{Al_2(CH_3)_6}$, TMA), held at room temperature, is used as the precursor. One ALD cycle comprises of a 0.2 s long pulse of TMA, which is followed by a 5 s long N_2 purge and two sequential 0.2 s long water vapor pulses. For the scaled deposition, the TMA pulse duration is modified while the remainder of the ALD procedure remains unchanged.

Figure 6 shows SEM images of a sample processed with 400 ALD cycles. Near the top of the VACNT array, the CNTs are clearly coated conformally with a thick layer of TiO_2. Further down the array, the TiO_2 coating becomes thinner, until only a few nucleation points of the oxide are visible on the CNTs. The rough surface of the oxide indicates the initial stages of nucleation. On the bare CNTs, the precursor adsorbs only onto discrete defect sites on the CNTs, and these nucleation centers expand with subsequent cycles, until they merge with one another.

The thickness of the deposited oxide as a function of the depth within the array is determined by measuring the diameter distributions of the coated nanotubes at various depths. This is carried out for two samples, one processed with 200 ALD cycles and the other processed with 400 cycles. The 200-cycle sample has a roughly constant oxide thickness of about 10 nm from the top of the array down to 28 μm, whereas the 400-cycle sample has an average oxide thickness of about 25 nm from the top of the array down to ca. 12 μm. At depths greater than approx. 30 μm, both samples have roughly the same oxide coating thickness. This confirms the model prediction that non-uniform oxide thickness does not arise as a result of a non-uniform deposition profile per cycle but rather from the decrease of the penetration depth of the oxide coating from cycle to cycle. A comparison of experimental and simulation results shows that the model scales correctly with the ALD cycle number. From the experimental data in Figure 6b, we find that for 400 cycles we have $x_\mathrm{p} \approx 12$ μm and $r_{400} \approx 28$ nm, while for the 200 cycle sample $x_p \approx 28$ µm and $r_{200} \approx 13$ nm. By using Equation 18 we can calculate $x_p(r_{200})/x_p(r_{400}) \approx 2.1$, which is very close to the measured value of (28 µm)/(12 µm) ≈ 2.3. One can utilize similar measurements to develop ALD recipes that can provide a uniform coating of the oxide up to a desired penetration depth. The parameter, Δr, required in Equation 19 can be extracted from the measurements of the oxide thicknesses for the coatings that result from two different numbers of cycles. The overall penetration depth can then be tuned, since it scales with the square root of the precursor exposure/adsorption time (see Equation 18).

To experimentally validate the pulse time scaling procedure developed from the model, we perform depositions of aluminum oxide on VACNT samples, during which we attempt to keep the penetration depth of each ALD cycle constant over one hundred cycles. In Figure 6c, the oxide thickness as a function of the depth within the array is plotted for samples coated with 100 and 200 cycles of aluminum oxide by using a fixed exposure time, and for one sample with 200 cycles, for which the exposure time from the 100th to the 200th cycle was scaled according to Equation 19. As expected, a uniform thickness up to $x_p \approx 12$ µm is obtained for the 100-cycle sample, while a uniform thickness down to $x_p \approx 7$ µm is obtained for the 200-cycle sample. From the plots, we determine $\Delta r \approx 0.12$ nm and we approximate $\sigma_{CNT} \approx 10^9$ cm^{-2}. For the number of cycles investigated here, Equation 19 can be approximated by $t_k = t_0 + t_0 k \Delta r / r_0$. By scaling of the pulse times between the 100th and 200th ALD cycles, the coating thickness remains roughly uniform down to $x_p \approx 12$ µm, as desired. The decrease in thickness at depths smaller than about 12 µm, as well as the thicker than expected coatings at depths greater than ca. 12 µm, are attributed to the fact that in the ALD system used, the pulse times are rounded to the nearest tenth of a second, which causes some ALD cycles during the scaling steps to be longer or shorter than desired. This result indicates that the scaling the pulse times is a viable method to obtain uniform coatings down to specific depths on high aspect ratio structures.

Conclusion

Our model and experiments indicate that limited penetration depth and non-uniformity of the ALD coatings of VACNTs result from the combination of slower diffusion and increased demand for precursor supply, effects that become increasingly important with each ALD cycle. This finding allows us to propose and subsequently validate that uniform ALD coatings to a desired depth within a high-aspect-ratio structure can be achieved by cycle-to-cycle variation of the precursor exposure time.

For the sake of convenience, a summary of important variables that were used in the modeling is given in Table 2.

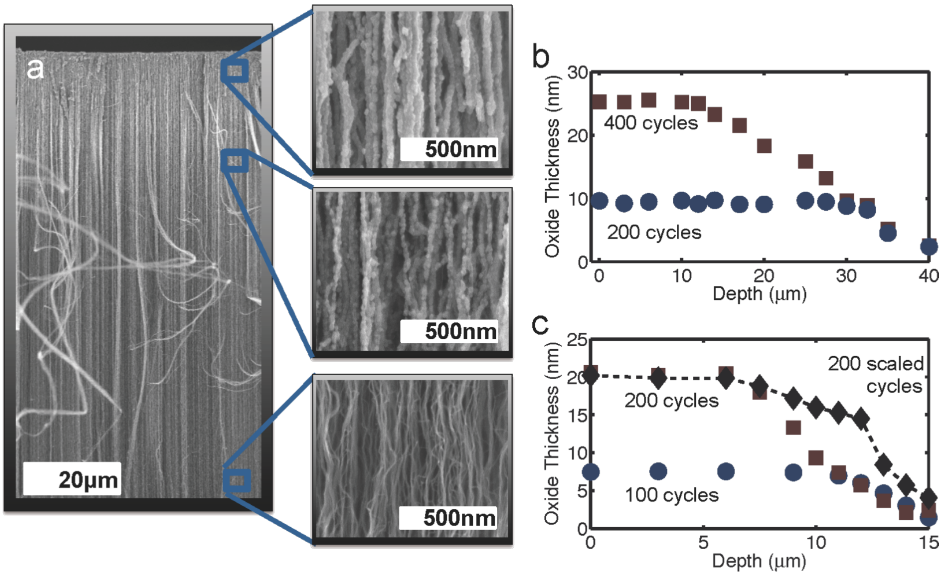

Figure 6: Experimental results for TiO_2 coated VACNTs. (a) An SEM image of a VACNT array coated with 400 cycles of TiO_2 is shown with close-up SEM images at depths of ca. 5, 25, and 80 µm. At 5 µm, a thick and conformal coating of TiO_2 is evident. At 25 µm the oxide coating is visibly thinner, and exposed CNTs are visible, at which the oxide beads have not merged, yet. Down at approx. 80 µm, only small nucleations of the oxide are noticeable. The TiO_2 thickness on the CNTs (determined by the measurement of the coated-CNT diameter distribution) as a function of depth is plotted in (b) for samples coated with 200 (circles) and 400 (squares) cycles. Error bars are indicated by the size of the points. Plot (c) shows the thickness of aluminum dioxide as a function of depth for the samples prepared with 100 cycles (blue circles) and 200 cycles (red squares), for which the precursor exposure time was fixed at 0.2 s, along with a plot for a sample prepared where the precursor exposure time was scaled as a function of ALD cycles between the 100th and 200th cycles (black diamonds).

Table 2: Summary of important variables used in the modeling.

variable	description	unit
n	density of precursor molecules	cm^{-3}
n_{ads}	density of adsorbed precursor molecules	cm^{-3}
N	precursor molecules per unit sample area	cm^{-2}
x	distance into the CNT array	cm
A	absorption rate per unit volume	$cm^{-3}s^{-1}$
I	impingement rate of precursor molecules	$cm^{-2}s^{-1}$
D_k	diffusion coefficient of precursor molecules within the CNT array	cm^2s^{-1}
f	fraction of the CNT surface area available for the precursor adsorption	—
Γ	reactive sticking coefficient	—
ΔA_s	surface area per unit volume	cm^{-1}
ΔV	void volume per unit volume	—
σ_{CNT}	CNT density	cm^{-2}
σ_p	adsorption site density	cm^{-2}
Δx	spacing of discretized points in simulation	cm
ΔA_i	surface area contained in Δx per unit area	—
ΔV_i	void volume contained in Δx per unit area	cm
n_i^j	density of precursor molecules	cm^{-3}
$N^j_{ads,i}$	number of adsorbed precursor molecules	cm^{-2}

References

1. Marichy, C.; Bechelany, M.; Pinna, N. *Adv. Mater.* **2012,** *24,* 1017. doi:10.1002/adma.201104129
2. Lahiri, I.; Oh, S.-M.; Hwang, J. Y.; Kang, C.; Choi, M.; Jeon, H.; Banerjee, R.; Sun, Y.-K.; Choi, W. *J. Mater. Chem.* **2011,** *21,* 13621. doi:10.1039/c1jm11474c
3. Meng, X.; Zhong, Y.; Sun, Y.; Banis, M. N.; Li, R.; Sun, X. *Carbon* **2011,** *49,* 1133. doi:10.1016/j.carbon.2010.11.028
4. Min, Y.-S.; Bae, E. J.; Jeong, K. S.; Cho, Y. J.; Lee, J.-H.; Choi, W. B.; Park, G.-S. *Adv. Mater.* **2003,** *15,* 1019. doi:10.1002/adma.200304452
5. Wen, Z.; Wang, Q.; Zhang, Q.; Li, J. *Adv. Funct. Mater.* **2007,** *17,* 2772. doi:10.1002/adfm.200600739
6. Chen, Y.; Zhang, Y.; Geng, D.; Li, R.; Hong, H.; Chen, J.; Sun, X. *Carbon* **2011,** *49,* 4434. doi:10.1016/j.carbon.2011.06.046
7. Cui, X.; Hu, F.; Wei, W.; Chen, W. *Carbon* **2011,** *49,* 1225. doi:10.1016/j.carbon.2010.11.039
8. Ma, S.-B.; Ahn, K.-Y.; Lee, E.-S.; Oh, K.-H.; Kim, K.-B. *Carbon* **2007,** *45,* 375. doi:10.1016/j.carbon.2006.09.006
9. Ma, S.-B.; Nam, K.-W.; Yoon, W.-S.; Yang, X.-Q.; Ahn, K.-Y.; Oh, K.-H.; Kim, K.-B. *J. Power Sources* **2008,** *178,* 483. doi:10.1016/j.jpowsour.2007.12.027
10. Nam, K.-W.; Lee, C.-W.; Yang, X.-Q.; Cho, B. W.; Yoon, W.-S.; Kim, K.-B. *J. Power Sources* **2009,** *188,* 323. doi:10.1016/j.jpowsour.2008.11.133
11. Raymundo-Piñero, E.; Khomenko, V.; Frackowiak, E.; Béguin, F. *J. Electrochem. Soc.* **2005,** *152,* A229. doi:10.1149/1.1834913
12. Boukhalfa, S.; Evanoff, K.; Yushin, G. *Energy Environ. Sci.* **2012,** *5,* 6872. doi:10.1039/C2EE21110F
13. Liu, C.; Wang, C.-C.; Kei, C.-C.; Hsueh, Y.-C.; Perng, T.-P. *Small* **2009,** *5,* 1535. doi:10.1002/smll.200900278
14. Marichy, C.; Donato, N.; Willinger, M.-G.; Latino, M.; Karpinsky, D.; Yu, S.-H.; Neri, G.; Pinna, N. *Adv. Funct. Mater.* **2011,** *21,* 658. doi:10.1002/adfm.201001572
15. Willinger, M.-G.; Neri, G.; Bonavita, A.; Micali, G.; Rauwel, E.; Herntrich, T.; Pinna, N. *Phys. Chem. Chem. Phys.* **2009,** *11,* 3615. doi:10.1039/b821555c
16. Willinger, M.-G.; Neri, G.; Rauwel, E.; Bonavita, A.; Micali, G.; Pinna, N. *Nano Lett.* **2008,** *8,* 4201. doi:10.1021/nl801785b
17. Altun, A. O.; Youn, S. K.; Yazdani, N.; Bond, T.; Park, H. G. *Adv. Mater.* **2013,** *25,* 4377. doi:10.1002/adma.201370199
18. Knez, M.; Nielsch, K.; Niinistö, K. *Adv. Mater.* **2007,** *19,* 3425. doi:10.1002/adma.200700079
19. Aarik, J.; Aidla, A.; Mändar, H.; Uustare, T. *Appl. Surf. Sci.* **2001,** *172,* 148. doi:10.1016/S0169-4332(00)00842-4
20. Aarik, J.; Aidla, A.; Uustare, T.; Ritala, M.; Leskelä, M. *Appl. Surf. Sci.* **2000,** *161,* 385. doi:10.1016/S0169-4332(00)00274-9
21. Herrmann, C. F.; Fabreguette, F. H.; Finch, D. S.; Geiss, R.; George, S. M. *Appl. Phys. Lett.* **2005,** *87,* 123110. doi:10.1063/1.2053358
22. Lu, Y.; Bangsaruntip, S.; Wang, X.; Zhang, L.; Nishi, Y.; Dai, H. *J. Am. Chem. Soc.* **2006,** *128,* 3518. doi:10.1021/ja058836v
23. Wang, X.; Tabakman, S. M.; Dai, H. *J. Am. Chem. Soc.* **2008,** *130,* 8152. doi:10.1021/ja8023059
24. Xuan, Y.; Wu, Y. Q.; Shen, T.; Qi, M.; Capano, M. A.; Cooper, J. A.; Ye, P. D. *Appl. Phys. Lett.* **2008,** *92,* 013101. doi:10.1063/1.2828338
25. Cavanagh, A. S.; Wilson, C. A.; Weimer, A. W.; George, S. M. *Nanotechnology* **2009,** *20,* 255602. doi:10.1088/0957-4484/20/25/255602
26. Lim, J.-W.; Park, H.-S.; Kang, S.-W. *J. Electrochem. Soc.* **2001,** *148,* C403. doi:10.1149/1.1368102
27. Yazdani, N.; Bozyigit, D.; Utke, I.; Buchheim, J.; Youn, S. K.; Patscheider, J.; Wood, V.; Park, H. G. *ACS Appl. Mater. Interfaces* **2014,** *6,* 1389. doi:10.1021/am405987t
28. Xiang, R.; Yang, Z.; Zhang, Q.; Luo, G.; Qian, W.; Wei, F.; Kadowaki, M.; Einarsson, E.; Maruyama, S. *J. Phys. Chem. C* **2008,** *112,* 4892. doi:10.1021/jp710730x

29. Zhong, G.; Iwasaki, T.; Robertson, J.; Kawarada, H. *J. Phys. Chem. B* **2007,** *111,* 1907. doi:10.1021/jp067776s
30. George, S. M. *Chem. Rev.* **2009,** *110,* 111. doi:10.1021/cr900056b
31. Dendooven, J.; Deduytsche, D.; Musschoot, J.; Vanmeirhaeghe, R.; Detavernier, C. *J. Electrochem. Soc.* **2009,** *156,* P63. doi:10.1149/1.3072694
32. Gordon, R. G.; Hausmann, D.; Kim, E.; Shepard, J. *Chem. Vap. Deposition* **2003,** *9,* 73. doi:10.1002/cvde.200390005
33. Elam, J. W.; Routkevitch, D.; Mardilovich, P. P.; George, S. M. *Chem. Mater.* **2003,** *15,* 3507. doi:10.1021/cm0303080
34. Adomaitis, R. A. *Chem. Vap. Deposition* **2011,** *17,* 353. doi:10.1002/cvde.201106922
35. Knoops, H. C. M.; Langereis, E.; van de Sanden, M. C. M.; Kessels, W. M. M. *J. Electrochem. Soc.* **2010,** *157,* G241. doi:10.1149/1.3491381
36. Rose, M.; Bartha, J. W. *Appl. Surf. Sci.* **2009,** *255,* 6620. doi:10.1016/j.apsusc.2009.02.055

License and Terms

The definitive version of this article is the electronic one which can be found at:
doi:10.3762/bjnano.5.25